ANALYSIS OF DEVELOPMENTAL REGULATION AND DISEASE MODELING OF CARGO TRAFFICKING IN ZEBRAFISH

By

Daniel Scott Levic

Dissertation

Submitted to the Faculty

of the Graduate School of Vanderbilt University

in partial fulfillment of the requirements

for the degree of

DOCTOR OF PHILOSOPHY

in

Cell and Developmental Biology

December 2015

Nashville, Tennessee

Approved:

David Miller, Ph.D.

Todd Graham, Ph.D.

Irina Kaverina, Ph.D.

Wendell Yarbrough, M.D.

This work is dedicated to Julie Gragg Levic,

whose countless sacrifices have allowed me to pursue my ambitions.

ACKNOWLEDGEMENTS

This work was made possible by the support of many. Foremost, I want to thank Ela Knapik. Ela has influenced me as a scientist in countless ways, but perhaps the greatest lesson she taught me is the art of mentorship. Very early in my training, Ela identified my strengths and weaknesses and thereby created an environment that fostered not only my analytical and scientific skills, but also my independence and resilience.

I also want to thank my committee members, David Miller, Irina Kaverina, Todd Graham, and Wendell Yarbrough. I'm grateful for their sharing of time and expertise, particularly for teaching me how to identify and focus on important questions. Undoubtedly, I will always remember David's litmus test for significance: what does your mutant tell you about how the system normally works?

I'm very thankful for Chris Wright, David Bader, Trish Labosky and the Program in Developmental Biology members. Chris, David, and Trish afforded me the opportunity of a slot in the program's training grant, not only providing financial support but also encouraging participation in the program's many training outlets. I'm grateful that David Bader allowed me to help with the program's "Bootcamp" course. An important lesson I learned from David is that a thorough understanding of anatomy and morphogenesis is an invaluable asset for a developmental biologist.

I want to thank collaborators, including Antonis Hatzopolous, Nancy Cox, Brian Eames, Hassane Mchaourab, and Mike Freeman for the opportunity of participating in their exciting projects. I also have had the pleasure of working closely with many brilliant colleagues, including Sataree Khuansuwan, Li-En Jao, Sanjay Mishra, Lehanna Sanders, and

Amudhan Venkateswaran. Finally, I would like to thank fellow my lab members, Gokhan Unlu, David Melville, Kirill Zavalin, Amy Rushing, Witek Rybski, Corey Guthrie, Blaine Stannard, Swapnalee Sarmah, and Wen-Der Wang, for helping to make a stimulating, productive, and exciting work environment.

TABLE OF CONTENTS

PAGE

LIST OF FIGURES

Figure Page

CHAPTER I

INTRODUCTION

Overview

A core feature of eukaryotic life is the ability to transport proteins to specific areas of the cell. This process, known as cargo trafficking, accounts for many fundamental cellular processes, including intercellular communication and cell polarity. One of the major trafficking routes is the biosynthetic-secretory pathway, which is responsible for secretion from the cell and which distributes membrane-embedded and soluble proteins throughout secretory organelles, including the endoplasmic reticulum (ER), Golgi apparatus, and lysosomes. Along this route, cargo is transported in vesicular carriers (small spherical or tubular vesicles) that emerge from a donor organelle and then fuse with a target membrane. Transport along the secretory pathway is highly regulated by cargo trafficking components at multiple steps, including cargo loading, vesicle budding, transport, docking and fusion.

Due to their involvement in diverse cellular functions, many cargo trafficking components, collectively referred to as trafficking machinery, are essential for viability in unicellular eukaryotes such as yeast (Schekman and Novick, 2004). Among multicellular eukaryotes, however, gene duplication events and subsequent coevolution have led to the paralogous expansion of many trafficking components, giving rise to proteins that have similar yet specialized functions in cargo traffic (Dacks and Field, 2007; Schlacht and

Dacks, 2015). Many trafficking components, even paralogs of the same gene family, have acquired specialized functions within different cell-types during development, homeostasis, and injury. In fact, regulation of protein trafficking underlies a variety of developmental programs in vertebrates, such as morphogenetic cell movements (Ogata et al., 2007; Ulrich et al., 2005), tissue and organ morphogenesis (Lang et al., 2006; Sarmah et al., 2010; Melville et al., 2011; Ellis et al., 2013), cell migration (Strachan and Condic, 2004), and cellular differentiation (Rodríguez-Fraticelli et al., 2015). Similarly, mutations in trafficking genes lead to many distinct types of human diseases (Corbeel and Freson, 2008; Howell et al., 2006; Jiang et al., 2014). For instance, mutations in human SEC23A and SEC23B, which share >95% amino acid sequence similarity and which both regulate ER-to-Golgi trafficking, result in skeletal malformations and anemia, respectively (Boyadjiev et al., 2006; Bianchi et al., 2009). Minor structural variations and differential regulation of expression levels are thought to contribute to the cell-type specific requirements of trafficking paralogs (Melville and Knapik, 2011; Unlu et al., 2014), yet a precise mechanistic basis for their functional differences remains unclear in many instances. Studies of cell-type-specific functions of trafficking components are therefore likely to lead to better understanding of human development and identify potential therapeutic targets for many diseases.

The goal of this dissertation is to identify novel functions of specific cargo trafficking components in development and disease. The introduction describes how animal models help to inform human disease studies and discusses examples of tissue-specific functions of trafficking components. Chapter II is a study examining the contribution of directed post-Golgi trafficking in cell shape regulation during

chondrocyte differentiation and cartilage growth. Chapter III describes a novel animal model to study the pathogenesis of a human lipid malabsorption disease caused by impaired pre-Golgi trafficking. Chapter IV is a study of the regulation of COPII-dependent cargo transport in skeletal morphogenesis. Chapter V concludes with a discussion of the significance and relevance of this dissertation research to cell and developmental biology as well has human health and disease, and outlines future lines of investigation. Portions of this introductory chapter are adapted from a review article to which I contributed:

Unlu G, **Levic DS**, Melville DB, Knapik EW (2014) Trafficking mechanisms of extracellular matrix macromolecules: insights from vertebrate development and human diseases. Int J Biochem Cell Biol. 47:57-67.

Significance of animal model studies of protein trafficking: crosstalk between human genetics and developmental biology

Although yeast and cell culture studies have been instrumental to the current understanding of protein trafficking, animal models are uniquely suited for discovering developmental and physiological functions of trafficking machinery. Additionally, animal model studies are critical for understanding the cellular and molecular mechanisms of human diseases. These studies are especially pertinent when diseases are associated with rare genetic variants, which are being discovered at increasing rates due to advances in next generation sequencing (Davis et al., 2014). For example, a given mutation may be identified in very small numbers of patients, or variants may be associated with

syndromes characterized by variable expressivity or reduced penetrance. Consequently there may not sufficient evidence or statistical power to demonstrate clear causation between a gene and disease (Smedley et al., 2014). In such instances, knowledge of the spectrum of animal model phenotypes associated with loss-of-function or mutations in a particular gene can aid the identification of a causative mutation among those in several candidate genes (MacArthur et al., 2014). For example, a recent study using whole exome sequencing of patients with a rare form Osteogenesis Imperfecta identified rare variants in five genes (Garbes et al., 2015). One of the candidates, *SEC24D*, which regulates ER-to-Golgi trafficking, had been extensively analyzed in multiple animal model systems and was selected for prioritization. Functional analysis confirmed that patient samples had cellular phenotypes consistent with those that were first discovered in *sec24d* mutant zebrafish (Sarmah et al., 2010; Garbes et al., 2015). Notably, patient symptoms were more consistent with phenotypes in zebrafish and medaka than with mice (Sarmah et al., 2010; Ohisa et al., 2010; Baines et al., 2013), demonstrating the importance of studying gene function in multiple systems.

In addition to testing the causal relationship between a gene and disease, animal model studies are also instrumental for uncovering mechanisms of pathogenesis. As an example consider complex diseases, which are influenced by multiple genetic factors. Genetic associations to complex diseases, including polygenic effects and contributions from rare variants in diverse genes, often have modest effect sizes and are statistically insignificant. Although variants may have small effect sizes when analyzed individually, the collective analysis of multiple genetic associations can reveal contributions of entire biological pathways, rather than individual genes, to complex diseases. This approach,

known as gene set or pathway analysis, is used to link collections of genetic associations for a given disease to an individual biological pathways using gene function annotation databases such as Gene Ontology (Mooney et al., 2014; Ashburner et al., 2000). A recent study using this approach identified novel genetic associations, including *SEC24D*, with perioperative myocardial infarction. While none of the individual variants they found met standard criteria for significance, pathway analysis revealed significant association with extracellular matrix (ECM) trafficking and remodeling (Kertai et al., 2015). Although association studies, next generation sequencing, and pathway analysis are important for uncovering genetic causes of disease, mechanistic animal model studies can lead to better understanding of the underlying pathologies. A recent study exploited knowledge from human genetics and developmental biology to identify GREM2, a secreted protein that modulates BMP (bone morphogenetic protein) signaling, as a novel candidate disease gene in atrial fibrillation (AF). By resequencing a cohort of idiopathic AF patients, the researchers identified a rare variant of *GREM2* (Q76E). They then used in vivo experiments in zebrafish to determine that the Q76E variant disrupts a genetic pathway regulating cardiac rhythm, giving insight into the biological pathway underlying AF (Müller et al., 2013).

Mechanisms of paralog-specific functions during COPII-dependent cargo transport

The trafficking and rapid secretion of large cargos such as collagens requires unique regulatory mechanisms to assure availability of specialized transport machinery (Saito et al., 2009b; Melville et al., 2011). Much of the current understanding of trafficking

regulation in the secretory pathway has come from studies using model cargo such as procollagen (Bonfanti et al., 1998; Arnold and Fertala, 2013). Procollagen is synthesized and initially post-translationally modified in the ER, and is then transported in a COPII (coat protein II complex)-dependent manner to the ER-to-Golgi intermediate compartment (ERGIC) en route to the Golgi complex, where further post-translational processing occurs (Canty and Kadler, 2005). Procollagen is then transported in tubular carriers to be secreted to the extracellular space, where it is cleaved and assembled into higher-order structures (Arnold and Fertala, 2013; Ishikawa and Bächinger, 2013).

A critical step of this journey is cargo export from the ER, which is mediated by the COPII complex. Pioneering work using yeast genetics first identified 23 genes, *SEC1-SEC23*, whose products are required for secretory activity (Novick et al., 1980; Schekman and Novick, 2004). Among them were components of the COPII complex (Barlowe et al., 1994). COPII formation is initiated when the cytoplasmic GTPase Sar1 undergoes a conformational change upon GTP binding and associates with the ER membrane (Nakano and Muramatsu, 1989; Barlowe et al., 1993; Kuge et al., 1994). Sar1 then recruits Sec23/Sec24 heterodimers to form the COPII inner coat complex (Matsuoka et al., 1998; Bi et al., 2002). Two additional ER associated proteins, Sec12 that acts as a GEF (guanine nucleotide exchange factor) for Sar1 and Sec16 that is a large scaffold protein, associate with ER Exit Sites and contribute to initiation of vesicle formation. Sec23 functions as a GAP (GTPase activating protein) for Sar1, resulting in coat dissociation from the vesicle membrane (Yoshihisa et al., 1993), and Sec24 acts as a cargo adaptor by selecting distinct proteins for ER exit (Miller et al., 2002). Assembly of the COPII inner coat is followed by recruitment of the Sec13-Sec31 heterotetramer of the outer coat complex, which stabilizes

the coat (Tang et al., 2000; Stagg et al., 2006; Bi et al., 2007; Bhattacharya et al., 2012; Copic et al., 2012).

Unlike the baker's yeast genome (*Saccharomyces cerevisiae*) that harbors single copies of these essential genes, vertebrate genomes have an expanded repertoire of COPII genes, including Sar1a and Sar1b (Jones et al., 2003), Sec23a and Sec23b (Paccaud et al., 1996), Sec24A, Sec24B, Sec24C and Sec24D (Tang et al., 1999), Sec13 (Swaroop et al., 1994), Sec31a and Sec31b (Tang et al., 2000). Gene multiplication of the coat components are thought to have been evolutionarily driven by genome expansion to accommodate novel extracellular matrix proteins and more complex body plans (Schlacht and Dacks, 2015).

Tandem genome duplication expanded the ancestral Sec24 gene to two syntenic groups, one being Sec24A and Sec24B and the second group being Sec24C and Sec24D (Tang et al., 1999). The four genes are highly divergent in sequence between the two groups (20% similarity) and approximately 50% similar between each pair, but each paralog is highly conserved within vertebrates (up to 90% sequence similarity between fish and human) (Sarmah et al., 2010). The high levels of divergence among the Sec24 paralogs may relate to their function in cargo selection for COPII vesicles (Miller et al., 2002). For example, differential expression of Sec24 paralogs may convey selectivity and redundancy for different cargos, a notion that is supported by cell culture studies of cargo selection during COPII transport (Wendeler et al., 2007).

Recent *in vivo* evidence obtained from phenotype-driven genetic screens in zebrafish, medaka, and mouse have begun to uncover the complexity of Sec24-based cargo selection. To date, only Sec24D has been directly implicated in ECM secretion. Mutant

bulldog/sec24d zebrafish embryos fail to secrete type II collagen and matrilin from chondrocytes, fibroblasts, and notochord sheath cells. These defects lead to severe craniofacial dysmorphology, shortened body length and kinked pectoral fins (Sarmah et al., 2010). The zebrafish *sec24d* mutant phenotypes are largely recapitulated by the *vbi/sec24d* medaka mutant, which carries a nonsense mutation that truncates a C-terminal portion of the Sec24D protein (Ohisa et al., 2010). In both zebrafish and medaka, Sec24D-deficient chondrocytes accumulate type II collagen in distended ER. However, other ECM and transmembrane proteins appear to be trafficked normally to the extracellular space and plasma membrane, including fibronectin, cadherin, and β1-integrin. In mice, however, gene-trap-mediated *Sec24D* knockout leads to pre-implantation lethality with no discernible phenotype in a haploinsufficient condition (Baines et al., 2013). The mouse data confirm that cargos that are required as early as the 8-cell stage are transported in a Sec24D-dependent manner. The inability to study Sec24D-dependent ECM transport during organogenesis in global mouse knockouts is complemented by studies in teleost fish such as zebrafish and medaka, which receive maternal Sec24D mRNA that allow for normal gastrulation. Notably, mutations in human *SEC24D* were recently identified in Osteogenesis Imperfecta, and patient symptoms were more similar to zebrafish *sec24d* mutants than to mouse *Sec24d* knockouts (Sarmah et al., 2010; Baines et al., 2013; Garbes et al., 2015).

Although Sec24D and Sec24C cargo adaptors recognize similar cargo binding motifs during in vitro assays (Wendeler et al., 2007), they appear to transport unique cargos in cell culture and in vivo studies. For example, Sec24C has been shown to be essential for secretion of neurotransmitter transporters (Sucic et al., 2011) and the fusion of

prechylomicron transport vesicles with Golgi membranes (Siddiqi et al., 2010). Furthermore, although Sec24D depletion in zebrafish results in craniofacial skeleton deficits as well as impaired notochord extension, Sec24C depletion only affects notochord extension and not the head skeleton. Combined depletion of Sec24C and Sec24D results in a significantly more severe phenotype, suggesting that Sec24C and Sec24D are exclusively required for secretion of select notochord basement membrane matrix proteins, whereas other matrix proteins are secreted in a redundant fashion by the two paralogs (Sarmah et al., 2010; Melville and Knapik, 2011). So far, only a few ECM cargos have been matched with specific adaptors. Future in depth studies will be needed to establish a combinatorial network of cargos and their respective adaptors and to understand how they are regulated to meet the secretory demand of different tissues during embryonic development.

SEC24B mutations were recently identified in patients carrying severe neural tube defects (Yang et al., 2013). Prior work in mouse mutants helped to explain how Sec24B is required for neural tube closure. Phenotype-driven chemical screens in mice have shown that Sec24B is essential for the secretion of Vangl2, a protein known to act in planar cell polarity (PCP) and the gastrulation movements of convergence and extension during early embryonic development. Defects in these processes result in craniorachischisis and neural tube closure defects in Sec24B mouse mutants (Merte et al., 2010; Wansleeben et al., 2010). Although not a matrix protein, Vangl2 function has been shown to regulate MMP-14 (membrane type-1 matrix metalloproteinase) that is involved in fibronectin remodeling during gastrulation (Latimer and Jessen, 2010; Williams et al., 2012b; a).

The discovery of tissue-specific phenotypes in carriers of Sec23A mutations challenged the prevailing view that Sec24 adaptors are solely responsible for the cargo

specificity of COPII carriers. Vertebrate genomes harbor two paralogs of the ancestral Sec23 gene, Sec23A and Sec23B (Paccaud et al., 1996), and phenotype-driven genetic screens in animal models along with disease genotyping in human patients provided the first evidence that Sec23A and Sec23B not only act in a tissue-specific manner, but also have cargo-specific trafficking functions.

A zebrafish *sec23a* mutant known as *crusher* (Driever et al., 1996; Neuhauss et al., 1996) was shown to carry a nonsense mutation at amino acid 402, resulting in a predicted stop codon and truncation of almost half of the Sec23a protein (Lang et al., 2006). Craniofacial dysmorphology and shortened body length are the predominant phenotypes of *sec23a* mutants, indicating deficits in skeletal development. At the subcellular level, *crusher* chondrocytes exhibit distended ER that accumulate type II collagen deposits. This intracellular backlog consequently leads to reduced Collagen and Matrilin content in cartilage ECM (Lang et al., 2006).

In parallel with discoveries of *sec23a* function in zebrafish, mutations in the human *SEC23A* gene were reported to cause cranio-lenticulo-sutural-dysplasia (CLSD), an autosomal recessive disorder characterized by facial dysmorphism and axial skeleton defects (Boyadjiev et al., 2006). Electron microscopy studies in fibroblasts isolated from CLSD patients revealed dilated ER structures and accumulation of procollagen in ER cisternae. To date, two missense mutations located near the Sec31 binding site of the SEC23A folded protein were identified in patients. The F382L mutation was shown to hinder SEC23A ability to recruit the SEC13-SEC31 outer coat and to ultimately prevent vesicle budding, whereas the M702V allele promotes premature dissociation of the COPII coat from ER membranes (Fromme et al., 2007; Boyadjiev et al., 2011; Kim et al., 2012).

Although other cargo molecules are packaged into COPII vesicles normally, procollagen accumulates in the ER of M702V mutant fibroblasts. These results suggest that COPII vesicles with a longer occupancy on ER membrane may be required to form sufficiently large carriers to transport procollagen (Kim et al., 2012). The zebrafish *crusher* and two CLSD mutations affect approximately the same region of the Sec23A protein and result in remarkably similar phenotypes, demonstrating the high degree of conservation of COPII-mediated collagen transport among vertebrates.

SEC23B mutations in humans, in contrast to those of *SEC23A*, are linked to Congenital Dyserythropoietic Anemia Type II (CDAII), an autosomal recessive disease characterized by ineffective erythropoiesis, hemolysis, and presence of multinucleated erythroblasts in bone marrow. The precise molecular mechanisms leading to these phenotypes are not understood, but electron micrographs of erythrocytes in peripheral blood showed double plasma membranes, and SDS-PAGE experiments revealed hypoglycosylation of membrane proteins (Bianchi et al., 2009), suggesting a requirement of SEC23B in the secretion of components of glycosylation pathways. Over 50 variants in *SEC23B* have been identified throughout the length of the coding region, and most of the patients are homozygous for missense mutations or compound heterozygotes presenting primarily with an anemia phenotype (Schwarz et al., 2009; Iolascon et al., 2010; Khoriaty et al., 2012). No homozygotes for nonsense mutations have been identified in approximately 370 reported cases (Iolascon et al., 2012). Interestingly, three independent *Sec23b* gene-trap insertion lines in mouse, each of which results in predicted null alleles, do not present an anemia phenotype and die at birth with profound developmental and exocrine organ secretion deficits (Tao et al., 2012). In contrast, zebrafish larvae depleted

in *sec23b* present an anemia phenotype and hemolysis similar to CDAII patients, and in addition they lack the entire neural crest-derived craniofacial skeleton (Lang et al., 2006; Schwarz et al., 2009). At present it is not clear whether the range of phenotypes represents species-specific functional differences or variations between hypomorph and null alleles. One potential explanation for the tissue-specific phenotypes observed with Sec23a and Sec23b mutations is that the two paralogs are required to transport distinct cargos. This notion, however, contrasts with the prevailing view that Sec24, but not Sec23, participates in COPII cargo selection. Whether Sec23b is required directly or indirectly to transport unique cargos from those of Sec23a remains unknown, and future studies will be needed to address these questions to better explain tissue- and species-specific phenotypes that have been observed.

Although not known to confer cargo-selection, Sec23a and Sec23b could indirectly influence cargo specificity of the COPII coat by selective interaction with Sec24 proteins, which are known to directly interact with cargos (Miller et al., 2002; Miller and Barlowe, 2010). In this scenario, Sec23a may be viewed as a critical partner for a collagen-specific Sec24 paralog. Alternatively, Sec23 could participate in direct cargo/receptor/adapter binding through undiscovered mechanisms. The complexity of paralog-specific functions in cargo transport in vivo is just being uncovered, and it has become clear that this is a complex problem that will require extensive investigation.

Sar1b function in COPII-dependent ER-to-Golgi transport

Sar1 is a small GTP-binding protein that initiates COPII coat assembly on ER membranes (Aridor et al., 2001; Bielli et al., 2005; Kuge et al., 1994). Similar to other COPII components, vertebrate genomes harbor two Sar1 genes, Sar1A and Sar1B (He et al., 2002; Jones et al., 2003; Levic et al., 2015). The two paralogs are highly conserved and the human genes vary by only 20 residues, whereas the fish and mammalian homologs share over 90% identity. Despite this remarkable similarity in sequence the two paralogs function in a distinct manner.

The distinct functions may potentially be explained by differential interactions of Sar1A and Sar1B with the outer COPII coat. Under Sec31-stimulated conditions, Sar1B hydrolyzes GTP more slowly than Sar1A possibly due to higher binding affinity of Sec13-Sec31 to Sar1A than to Sar1B containing coats (Fromme et al., 2007). Conceivably, this high-affinity binding of Sar1A to the outer coat could lead to tightly packaged small vesicles, whereas loosely packed Sar1B -outer coat complex may allow for larger COPII carriers (Fromme et al., 2008). Although this could potentially help to explain how enlarged COPII carriers are formed, it remains unknown whether the different binding affinities of Sar1A and Sar1B for the COPII outer coat observed in vitro translate into functional differences in a physiological context. Alternatively, for example, Sar1b may accommodate the formation of larger sized carriers primarily due to its slower rate of GTP hydrolysis, which slow the kinetics of vesicle budding to allow larger vesicles to form.

Consistent with the carrier size hypothesis, chylomicrons (250 nm in size) are significantly larger than typical 90 nm COPII vesicles, and have been observed to be secreted in a Sar1B-dependent rather than Sar1A-dependent manner (Shoulders et al., 2004). Mutations in human SAR1B were shown to cause chylomicron retention disease (CMRD), a lipid absorption disorder characterized by deficits in intestinal lipid uptake and hypocholesterolemia (Jones et al., 2003). Besides lipid malabsorption, some CMRD patients are diagnosed with other symptoms, including exocrine pancreatic insufficiency, decreased bone mineral density, and cerebellar ataxia. The pathophysiology of the disease is not understood; however, sar1b loss-of-function experiments in zebrafish embryos showed not only intestinal lipid absorption deficits but also craniofacial dysmorphology due to failure of type II collagen secretion to extracellular cartilage matrix (Levic et al., 2015). These findings suggest that Sar1b is needed not only for secretion of lipids in large chylomicrons, but also large extracellular matrix proteins such as collagen.

Interestingly, no mutations in the SAR1A coding region have been identified in patients (Charcosset et al., 2008; Kumkhaek et al., 2008) and depletion of Sar1a in zebrafish did not result in a gross dysmorphology (Levic et al., 2015). Recent experiments in mammalian cell culture setting examined essential roles of Sar1a and Sar1b and revealed that cells depleted in both paralogs were still capable of secreting small globular proteins (VSV-G) in a COPII-independent manner using a previously uncharacterized, atypical COPI-dependent secretory mechanism. Procollagen type I, however, was retained in the ER and did not sort to ER exit sites (Cutrona et al., 2013). These findings open a new, intriguing possibility for ECM transport mechanisms,

particularly because COPI genetic mutations in zebrafish have deficits in secretion of notochord basement membrane proteins (Coutinho et al., 2004). For example, copa depletion results in a highly similar phenotype in the craniofacial skeleton compared to Sec23a mutants alone; however, combined copa/sec23a mutants had a significantly shorter axial skeleton than either condition alone (Lang et al., 2006). These results suggest that distinct trafficking pathways are required for morphogenesis of the two tissues, which are composed of distinct ECM components. Further investigations are needed to better understand the function of the COPII inner coat in ECM secretion, as well as the regulatory mechanisms that provide the proper combinations and stoichiometry of different inner coat paralogs to meet the secretory demand of various tissues and organs.

CHAPTER II

POST-GOLGI TRAFFIC ACTS AS A GATEKEEPER OF CELL GROWTH BY SPATIALLY RESTRICTING CARGO DELIVERY

Daniel S. Levic[1,2], David B. Melville[1,2,3], Gokhan Unlu[1,2], and Ela W. Knapik[1,2],

[1]Department of Medicine, Division of Genetic Medicine; [2]Department of Cell and Developmental Biology, Vanderbilt University Medical Center, Nashville, TN 37232, USA

Present Address: [3]Department of Molecular and Cell Biology, University of California at Berkeley, CA 94720-3370, USA

This chapter is being prepared for submission.

Abstract

Cell shape regulation is critical for morphogenesis and tissue repair, but despite broad significance, little is known about how cells modulate shape and length in their native microenvironment in vivo. Here, we employ a mesenchymal cell-type to ask how shape is regulated cell autonomously in the absence of direct cell-cell contacts. Using forward genetics, we identified Erc1 as a central regulator of cell shape changes occurring during

chondrocyte differentiation. We show that Erc1 functions cell-autonomously at the cell cortex to regulate microtubule organization and cargo traffic required for cell growth. Time-lapse imaging reveals that Erc1-deficient chondrocytes elongate but then contract in width, leading to cell death and limiting cartilage growth. Destabilizing polarized microtubules or blocking Rab11function rescues cell shape changes in Erc1-deficient cells. We propose that regulation of cargo traffic via endo- and exocytic recycling drives cell shape changes during chondrocyte differentiation. Understanding mechanisms of Erc1-directed cell shape changes could facilitate future use of mesenchymal stem cells in wound healing, tissue engineering and regeneration.

Introduction

A striking feature of mature differentiated cells is their characteristic and evolutionarily-conserved shape. For example, neurons, intestinal epithelial cells, and chondrocytes each have unique but stereotypic shapes that influence their function within respective organs. The fact that morphology differs vastly among distinct cell-types suggests that similar variation exists in the mechanisms governing cell shape. However, much of the current understanding of cell shape regulation has come from studies of epithelial sheets, in which cell shape is influenced by both intrinsic and extrinsic factors. For example, forces imposed on an epithelial cell from neighbors can be counter-balanced by changes in cortical tension to maintain cell shape (Mao and Baum, 2015). Alternatively, non-cell-autonomous mechanisms regulate cell shape changes by tissue-level forces during epithelial morphogenesis (Monier et al., 2015; Porazinski et al., 2015). Cytoskeletal

reorganization is the predominant intrinsic factor controlling cell shape, with actomyosin-based contraction being an important regulator (Paluch and Heisenberg, 2009; Mao and Baum, 2015). However, the mechanisms by which cell shape changes are managed in the absence of direct cell-cell contact are largely unknown.

Shape regulation of isolated cells has primarily been studied in unicellular organisms (He et al., 2007) and cultured cells in vitro (Picone et al., 2010). In cultured fibroblasts and myoblasts, for example, cell length is influenced by microtubule (MT) dynamics (Straube and Merdes, 2007; Picone et al., 2010). Although MT polymerization contributes to cell elongation, it is not considered to generate sufficient force to grow the cell by pushing out on the cell cortex (Morris and Homann, 2001), suggesting that MT-dependent cell shape changes may depend on additional factors. Furthermore, how mesenchymal cells in vivo in a complex, three-dimensional microenvironment regulate cell shape in the absence of direct cell-cell contact remains an open question.

To address this question of how shape is regulated cell-autonomously in vivo, we used chondrocyte cell elongation that occurs during stacking as a model. Stacking is a process where clusters of small, round cells lose cell-cell contacts and rearrange into organized, stereotypical rows of elongated chondrocytes that are immersed in extracellular matrix (ECM), promoting skeletal growth and function (Kimmel et al., 1998). We previously observed that inhibiting ER-to-Golgi secretory traffic arrests chondrocyte stacking and cell elongation (Sarmah et al., 2010), leading us to ask by what mechanisms cargo traffic regulates cell shape (Fig. 2.1). Here, using a forward

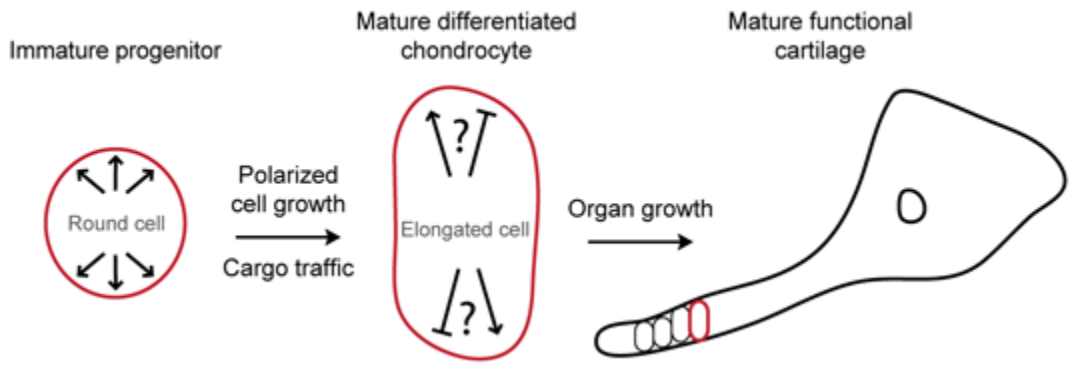

Figure 2.1. Hypothetical model of cell shape regulation during chondrocyte differentiation and cartilage growth.
Schematic of cell shape changes during chondrocyte differentiation. Small, round cells elongate (arrows) to form stacks of mature chondrocytes, a process dependent on cargo traffic (Sarmah et al., 2010). We hypothesize that additional unknown trafficking components regulate cell shape, and subsequently impact organ size and function.

genetics approach, we have identified Erc1 as a central regulator of cell shape changes during chondrocyte differentiation and cartilage growth. Erc1 localizes to the chondrocyte cell cortex, where it regulates microtubule organization and cargo traffic to balance polarized cell growth. In the absence of Erc1, chondrocytes increase in length but contract in width, leading to elongated but narrow cells that subsequently undergo apoptosis. Erc1-deficient cell shape changes are suppressed by destabilizing polarized microtubules or by inhibiting Rab11 activity. Conversely, inhibiting exocytic components Rab8a or Kinesin-1 in WT chondrocytes is sufficient to phenocopy Erc1 mutants. Our data implicate endo- and exocytic recycling pathways as a regulatory mechanism for spatially restricting vesicle cargo delivery to shape cell growth after chondrocyte differentiation.

Materials and methods

Fish maintenance and breeding

Zebrafish were raised and kept under standard laboratory conditions at 28.5°C as previously described (Montero-Balaguer et al., 2006). All experiments were conducted in accordance with the guidelines established by the IACUC at Vanderbilt University.

Genetic mapping and cloning

The *kimble* locus was mapped in an F2 intercross using bulked segregate analysis. DNA samples were PCR-genotyped with SSLP markers evenly spaced across the zebrafish genome (Knapik et al., 1998; Melville et al., 2011). The mapped kim^{m533} mutation was confirmed by Sanger sequencing of genomic DNA flanking the mutation site from two

homozygous wild-type F2 animals, six heterozygous F2 animals, six homozygous mutant F2 animals and two animals each from three different genetic backgrounds of wild-type fish (AB, IN and TL) (Knapik et al., 1996).

Cartilage proteoglycan staining

Alcian Blue staining was performed as previously described (Melville et al., 2011) with modifications. Larvae were fixed in 4% PFA, stained overnight in 0.1% Alcian Blue in 70% EtOH/1% HCL, de-stained in 70% ethanol/ 5% HCl, and then cleared in 50% glycerol/0.25% KOH. Differential interference contrast (DIC) images were acquired from dissected, flat-mounted cartilage using a 100x oil-immersion objective mounted on a Zeiss AxioImager Z1.

Morphometric analysis of chondrocyte cell shape

Due to the irregular shape of mutant chondrocytes, average cell width was calculated by measuring cell length and area in ImageJ and using the formula for the area of an ellipse, $A=\pi*a*b$, where a is the length of the major axis (cell length/2) and b is the length of the minor axis (cell width/2). Thus, average cell width was calculated using the formula, $width=(4*area)/(\pi*length)$.

Cell death analysis

Double strand DNA breaks were detected using the TUNEL method as previously described (Granero-Moltó et al., 2008). Embryos were anesthetized, fixed in 4% PFA,

and then processed for cryosectioning. TUNEL was performed using the Roche *In Situ* Death Detection Kit.

Electron microscopy

Samples were processed as previously described (Melville et al., 2011). Embryos were fixed in 2.5% glutaraldehyde in 0.1 M sodium cacodylate at room temperature for 1 hr. and then overnight at 4°C. After rinsing in 0.1 M sodium cacodylate, samples were post-fixed with 1% osmium tetroxide in 0.1 M sodium cacodylate for 1 hr. Following additional rinsing, specimens were dehydrated step-wise in ethanol and then propylene oxide, infiltrated with resin step-wise, and then embedded in resin for 48 hours at 60°C. 50 nm sections were collected on a Leica Ultracut Microtome and analyzed on a Phillips CM-12 Transmission Electron Microscope provided by the VUMC Cell Imaging Shared Resource.

Immunofluorescence (IF), fluorescence microscopy, and image processing

Processing for IF was performed as previously described (Sarmah et al., 2010) with modifications. Embryos were fixed in freshly prepared 2-4% PFA and incubated in 30% sucrose/PBS prior to embedding in Cryomatrix, (Thermo Scientific). Frozen sections were collected with a Leica CM-1900 cryotome. Primary antibodies used were GFP (Vanderbilt Antibody and Protein Resource), Erc1 (Abcam), alpha-tubulin (Abcam), and FLAG, M2 clone (Sigma). Alexa Fluor 488- and 555- (Life Technologies) or DyLight 550-conjugates (Thermo Scientific) were used for secondary antibodies. To-Pro-3 (Molecular Probes) or 4',6-diamidino-2-phenylindole (DAPI, Molecular Probes) was

applied as a nuclear counterstain. Proteoglycan and cortical staining was performed using Alexa Fluor-conjugated Wheat Germ Agglutinin (WGA, Life Technologies) and Phalloidin (Life Technologies), respectively. Slides were mounted in ProLong Gold (Life Technologies) prior to imaging, which was performed using Zeiss LSM-510 Meta or LSM-710 Inverted Confocal Microscopes (VUMC Cell Imaging Shared Resource) with a Plan-Apochromat 63x/1.40 Oil objective or an AxioImager Z1 equipped with an Apotome (Zeiss) and an EC Plan Neofluar 100x/1.30 Oil objective. Widefield fluorescence data were deconvolved using default settings using the Zen 2012 software package (Zeiss). For tubulin IF, samples were fixed in a buffer containing PFA and glutaraldehyde in Cytoskeletal Buffer (9 mM MES (2-(4-Morpholino)ethane Sulfonic Acid), 150 mM NaCl, 5 mM EGTA, 5 mM $MgCl_2$, 5 mM glucose), quenched in 0.1% $NaBH_4$, and then processed as described above. Post-acquisition data processing was limited to linear adjustments for brightness using the levels tool in Adobe Photoshop.

Live time lapse imaging

3 dpf WT or *kim*^{m533} Tg(col2α1:caax-eGFP) were anesthetized in tricaine and mounted in 1.2% low melting point agarose. Embryos were positioned laterally at a 45° angle with the ear capsule fixed close to the bottom of the glass dish. Confocal images were collected every 2 minutes for 4 hours using an LSM710 (Zeiss) with a 28.5°C heated chamber and 63x 1.4 NA objective.

Distance measurements of Erc1 puncta from the cell membrane

Embryos were fixed for 20 minutes in 2% PFA, and then processed for cryosectioning, IF, and confocal microscopy as described above. Z-stacks were processed in Imaris 8.0 (Bitplane) with standard Matlab extensions. The caax-eGFP channel was used to create a surface of the cell membrane of individual chondrocytes, and the spots tool was used to detect Erc1 puncta. The distance transformation extension was used to measure the distance of Erc1 puncta from the cell membrane surface and to pseudo-color Erc1 spots. Distance measurements of 10 cells from 3 animals were collected using the statistics tab.

3D rendering of whole cartilage elements

Embryos were anesthetized and fixed in 4% PFA overnight, bleached in H_2O_2 /KOH solution, permeabilized, and then stained with Alexa Fluor 488-conjugated Wheat Germ Agglutinin (WGA, Life Technologies) overnight. Embryos were then rinsed, cleared in glycerol overnight, mounted in agarose on glass bottom dishes, and confocal z-stacks of the entire hyosymplectic (HS) cartilage (approximately 80-100 μm thick) were collected using a Zeiss LSM-710 Inverted Confocal Microscope using a Plan-Apochromat 20x/0.8 M27 objective. 3D projections, rendering, and volume measurements were performed in Imaris 8.0 using the surfaces tool and statistics tab.

Generation of transgenic constructs

Transgenic constructs were generated using gateway cloning and the Tol2kit (Kwan et al., 2007). Primers used were: pCS2-Erc1, 5'-AGGGAATGAGTGATAGGTGC -3', 5'-AAGCGCCCTGGCTCTTAGAT-3'; pME-Erc1, 5’- GGGGACAAGTTTGTACAAA AAAGCAGGCTCCATGTATGGCAGTGCCCGATC-3’, 5’- GGGGACCACTTTGT

ACAAGAAAGCTGGGTCTGCCCAAATGCCCTCCTCA-3'; pEGFP-Rab8a, 5'-CCCCTCGAGCCATGGCGAAGACCTACGATTA-3', 5'-CCCAAGCTTTCACAG TAGCACACAGCGAA-3'; pME-eGFP-Rab8a, 5'-GGGGACAAGTTTGTACAAAA AAGCAGGCTCCATGGTGAGCAAGGGCGAGGAG-3', 5'-GGGGACCACTTTGT ACAAGAAAGCTGGGTCTCACAGTAGCACACAGCGAA-3'; pME-FLAG-Kif5Ba, 5'-ATGGATTACAAGGATGACGACGATAAGCCCATGGCGGACCCGGCGGAG TG-3', 5'-GCACGATCGATGCTCTCTTA-3', 5-GGGGACAAGTTTGTACAAAAA AGCAGGCTCCATGGATTACAAGGATGACGACGA-3', 5'-GGGGACCACTTTGT ACAAGAAAGCTGGGTCTCAGCTCTTCTCTTGTTTAGTGCC-3'; pME-FLAG-Kif5BaΔHead, 5'-ATGGATTACAAGGATGACGACGATAAGCCCAATGTGGAGCT GACAGCAGAG-3', 5'-GCACGATCGATGCTCTCTTA-3', 5-GGGGACAAGTTTGTA CAAAAAAGCAGGCTCCATGGATTACAAGGATGACGACGA-3', 5'-GGGGACCA CTTTGTACAAGAAAGCTGGGTCTCAGCTCTTCTCTTGTTTAGTGCC-3'; pME-EB3-GFP, 5'-GGGGACAAGTTTGTACAAAAAAGCAGGCTCCATGGCCGTCAAT GTGTACTC-3', 5'-GGGGACCACTTTGTACAAGAAAGCTGGGTCTTACTTGTACA GCTCGTCCATG-3' pME-eGFP-Rab11a was generated by the Link laboratory (Clark et al., 2011) and shared with us by the Bagnat laboratory (Ellis et al., 2013).

Whole mount *in situ* hybridization

Whole mount *in situ* hybridization with probes recognizing *sox9a* and *col2α1* was performed as previously described (Montero-Balaguer et al., 2006). The *erc1* probe was made by cloning 1041 nucleotides of 3' UTR from cDNA into the pGEM-T Easy Vector (Promega) using primers listed in Supplementary Table 1.

Histology

Processing for histology from JB-4 plastic resin was performed as previously described (Lang et al., 2006). Sections were stained with Toluidine blue (Sigma).

Embryo lysis and western blotting

Epiboly stage embryo lysates were prepared as previously described (Dohn et al., 2013) with modifications. Embryos were dechorionated with Pronase (Merck), de-yolked, lysed in RIPA buffer supplemented with protease inhibitor cocktail (RIPA+PI) by rocking at 4°c, and then clarified by centrifugation. For later-stage embryos, whole heads were dissected at the ear capsule, pestle-homogenized in RIPA+PI, and then prepared as described above. Lysates were boiled for 10 min in Laemmli sample buffer, separated by SDS-PAGE, and transferred to PVDF membranes (BioRad). Membranes were blocked with 2% non-fat milk in TBS–Tween (50 mM Tris, pH 7.4, 150 mM NaCl, 0.1% Tween-20), incubated overnight with primary antibody in 2% BSA in TBS-Tween at 4 °C, followed by peroxidase-conjugated secondary antibodies (Promega). Signal was developed using ECL substrate (Perkin Elmer), and detected using a ChemiDoc system (BioRad). Antibodies used were Erc1 (Abcam) and alpha tubulin, DM1A clone (Sigma).

Quantification of proteoglycan retention

Mean pixel intensity values of WGA fluorescence were measured in the cytoplasm and then divided by that of the directly adjacent ECM on individual z-sections using ImageJ.

Statistical analysis

For comparisons of 2 groups, p-values were calculated using two-tailed unpaired t-tests. For comparisons of more than 2 groups, one- or two-way analysis of variance (ANOVA) was used to test for significance followed by Tukey's test to determine p-values. Categorical data was analyzed using Fisher's exact test. All bar graphs are presented as mean ± SD.

BrdU incorporation assay

Embryos were incubated in 10 mM BrdU (Life Technologies) in 0.3x Danieau buffer continuously, and solution was replaced every 4 hours. After fixation, embryos were processed for cryosectioning and BrdU was detected with IF (clone G3G4, Developmental Studies Hybridoma Bank).

RNA isolation and RT-PCR analysis

RNA extraction and reverse transcription was performed as previously described (Melville et al., 2011; Müller et al., 2013, 2). cDNA was used as template for qPCR analysis using exon-spanning primers. The primer sequences used are: βactin, 5'-GACTCAGGATGCGGAAACTG-3', 5'-AAGTCCTGCAAGATCTTCAC-3'; xbp1, 5'-AAGGAGCAGGTTCAGGTACT-3', 5'-TAGATGTGGTCGAAGTGGAT-3', bip, 5'-GCCATGGTTTTGACCAAGATGAAG-3', 5'-GAAGTGCTCCATGACGCGCTGGTC-3'; sil15'-CAGGAAAGAGTAAAACAGCAACCG-3', 5'-CCGAAATTTTGCTCTCAC TGCATC-3'; chop, 5'-ATGACTGCGGAGTGGCTGTA-3', 5'-GAAGGAGATCTCCGG ATGAG-3'; erol1b, 5'-AAACAACTGCTGCTGGAGAT-3', 5'-CTGCAGCCGACGCA

GTCCAT-3'; ppp1r15a, 5’-TCGTTCCTCAATAATGGCGA-3' , 5’-CTGCTCGCAT AACTCCAGAC-3'.

Results

Model of mesenchymal cell shape changes

As a model for mesenchymal cell shape regulation, we chose the zebrafish hyosymplectic (HS) cartilage, which is formed as condensed, non-proliferative progenitor clusters rearrange into a stack of differentiated chondrocytes (Kimmel et al., 1998). For the purpose of quantitative cell shape analysis, we divided HS cartilage formation into three phases. First, at the condensation phase (CP, 2.5 dpf), cartilage was composed of clusters of small, round cells that were Alcian blue-negative before the onset of ECM production (Fig. 2.2A). In the subsequent elongation phase (EP, 3 dpf), chondrocytes showed evidence of stacking and cell elongation, as measured by the cell length-to-width (l/w) ratio (Fig. 2.2B,G,H). EP chondrocytes were also Alcian blue-positive, indicating that ECM proteins are synthesized and secreted during cell growth. Finally, at the isometric growth phase (IGP, 3.5 dpf), chondrocytes were characterized by additional cell growth but without increases in the l/w ratio (Fig. 2.2C,G,H). The CP-IGP stages define a progression from progenitor-to-differentiated cell undergoing polarized and then proportional cell growth and were used as a staging system throughout this study. In summary we confirm that cell shape changes and ECM secretion are both executed during chondrocyte differentiation.

By screening a collection of chemically induced mutations in zebrafish, we found that the *kimble* (*kim*^{m533}) (Neuhauss et al., 1996) line exhibits extreme cell shape abnormalities during stacking, leading to a malformed jaw. While CP *kim*^{m533} chondrocytes were indistinguishable from wild types (Fig. 2.2A,D,G,H), later-stage EP *kim*^{m533} chondrocytes were highly elongated and narrow cells, resulting in a significantly greater l/w ratio than wild types (Fig. 2.2E,H,I). In the next IGP, mutant chondrocytes remained elongated and appeared further constricted in width, thereby forming an hourglass-like shape (Fig. 2.2F). When viewed in 3D using confocal microscopy and surface rendering, mutant chondorcytes were also misshapen along the z-axis (Fig. 2.3A,B), suggesting that during cell elongation mutant chondrocytes grow circumferentially at polarized ends and fail to maintain or expand in width.

Stacked *kim*^{m533} chondrocytes appeared to occupy less space than wild types (Fig. 2.2A-F, brackets), suggesting that impaired cell shape regulation restricts cartilage growth. To quantify the size of cartilage, we imaged whole HS cartilage with confocal microscopy and then performed 3D surface rendering and volume measurements (Fig. 2.4A-C). IGP *kim*^{m533} cartilage was 34.4% smaller than WT (Fig. 2.4C), highlighting the importance of cell shape regulation for organ size and growth. Cell shape dysregulation also led to later functional deficits. A primary role of cartilage is to serve as a template for endochondral bone formation. *Kim*^{m533} mutants lacked endochondral bones, although intramembranous ossification was unaffected, demonstrating a cartilage-specific defect in ossification (Fig. 2.4D). In summary, impaired chondrocyte cell shape regulation during organogenesis leads to restricted growth and function of the organ later in development.

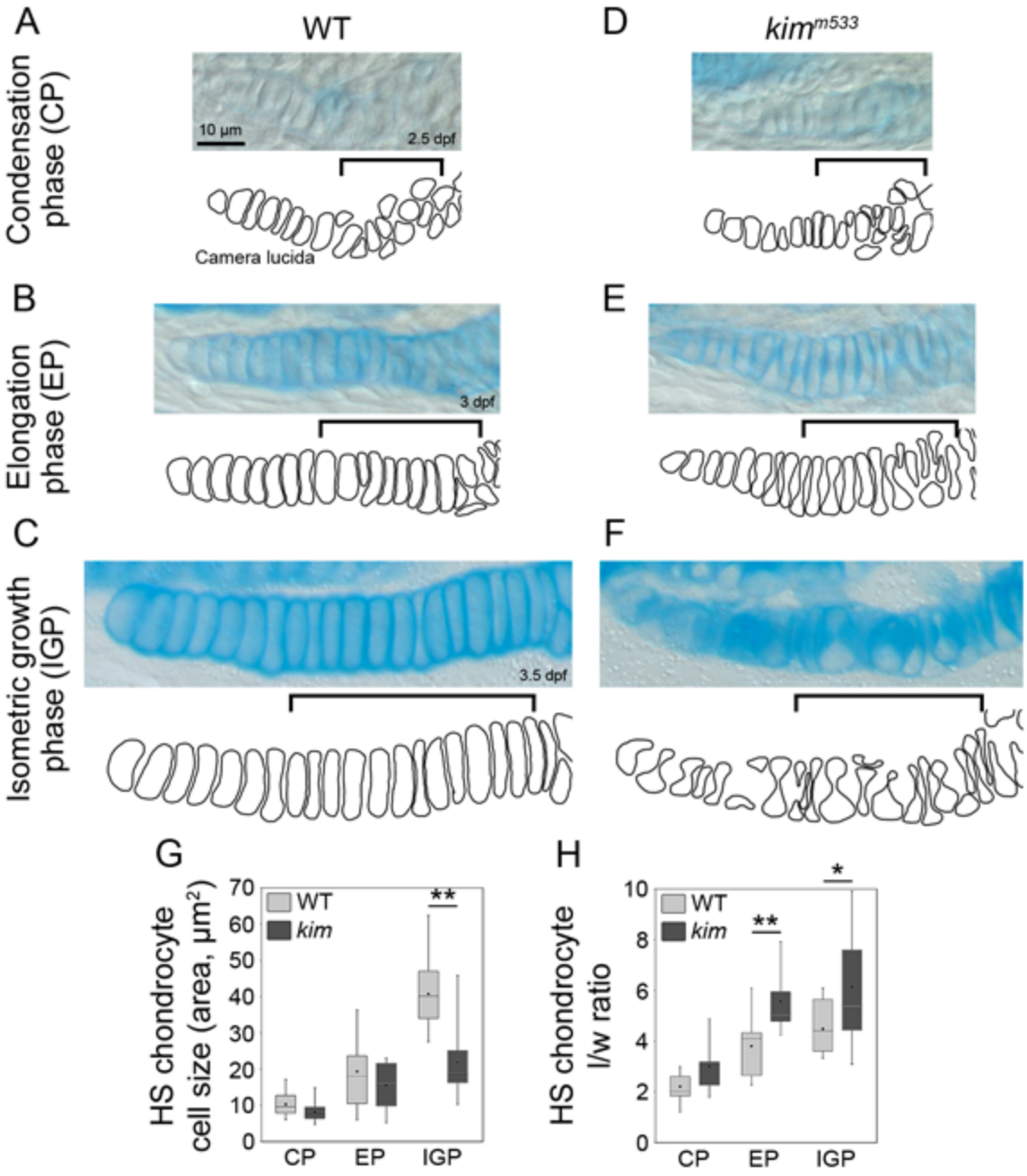

Figure 2.2. Polarized cell growth and ECM secretion accompany chondrocyte differentiation.

(A-F) DIC images and camera lucida cell outlines of Alcian-blue stained hyosymplectic (HS) cartilage. Brackets indicate stacking chondrocytes. The CP-EP transition is characterized by cell elongation and ECM secretion (A,B), while the EP-IGP transition is accompanied by isometric cell growth (B,C). CP-EP *kim*^{m533} chondrocytes stack but elongate disproportionally (D,E). EP-IGP *kim*^{m533} chondrocytes appear to grow only at polarized ends, resulting in an hourglass cell shape (F). (G,H) Quantification of cell size and shape changes during differentiation. *p<0.05, **p<0.01

Cell shape and organ size defects (Fig. 2.5A) were not caused by an altered chondrocyte differentiation program, as shown by similar expression patterns of *sox9a* and *col2α1* in WT and *kim*^{m533} cartilage (Fig. 2.5B,C). Furthermore, although hourglass-shaped cells resemble mitotically dividing cells, proliferation analysis using 12 hour BrdU incorporation assays in CP-EP cells indicated that these cells remained in interphase (Fig. 2.5D-F), excluding disturbances in cell division as a potential cause of shape changes.

The microtubule cytoskeleton regulates mesenchymal cell shape during growth

To determine the cause of cell shape dysregulation, we tested whether chondrocyte elongation is dependent on the cytoskeleton, which was implicated in cell shape regulation by various mechanisms (Picone et al., 2010; Dent et al., 2011; Sehring et al., 2014). We treated CP-IGP *kim*^{m533} and WT embryos with chemical modulators of actin or microtubule (MT) filaments for 24 hr and then performed cell shape analysis using fluorescence microscopy.

In WT embryos treated with low concentrations of the MT destabilizing compound nocodazole (0.6 μM), chondrocytes were more closely appositioned than controls, but otherwise exhibited normal cell shape (Fig. 2.6A). Strikingly, nocodazole-treated *kim*^{m533} chondrocytes no longer exhibited an hourglass shape and instead were relatively similar to WT, indicating that mutant cell shape chages are mediated by microtubules (Fig. 2.6A,B). Paclitaxel-mediated MT stabilization (20 μM) did not cause cell shape changes in WT or *kim*^{m533} chondrocytes. Thus, although MT destabilization rescues *kim*^{m533} cell shape, MT stabilization alone in WT chondrocytes is not sufficient to induce the

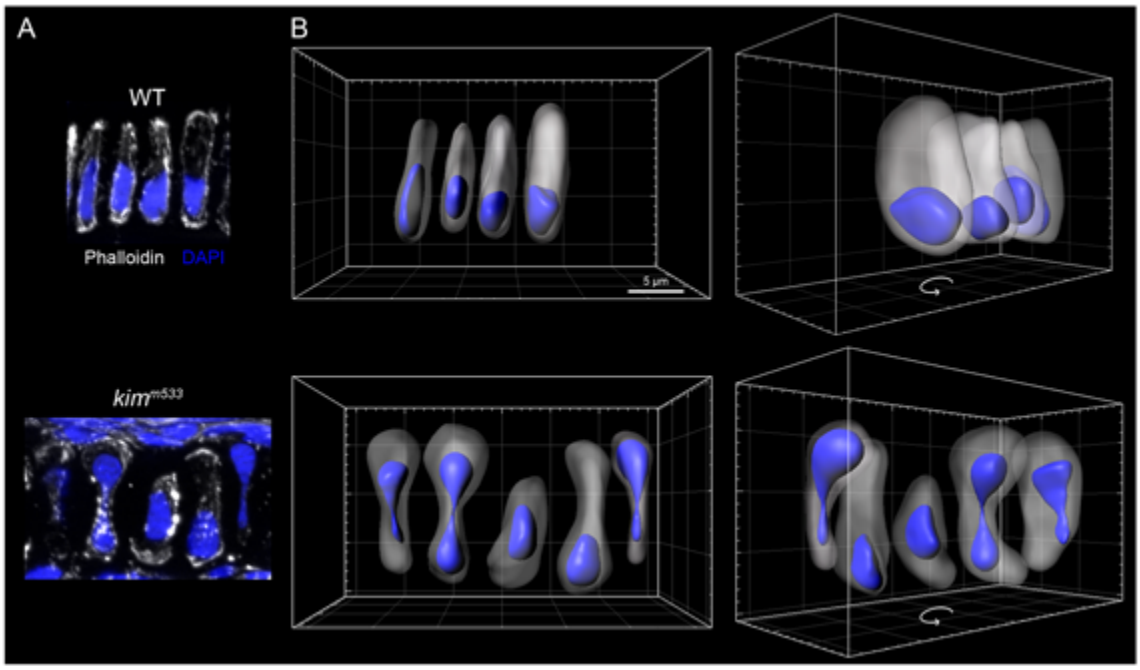

Figure 2.3. *Kim*^{m533} chondrocytes grow circumferentially at polarized cell ends. **(A)** Fluorescence microscopy and **(B)** 3D rendering of cell (phalloidin) and nuclear (DAPI) shape. WT chondrocytes exhibit a flattened coin-like shape, while *kim*^{m533} chondrocytes are constricted in cell width and elongated along the circumference of polarized ends.

elongated, narrow shape seen in mutant cells (Fig. 2.6A,B).

Because we observed nuclear deformation in *kim*^{m533} chondrocytes (Fig. 2.3A,B), we tested whether cell shape dysregulation impairs cell survival. A small percentage of EP *kim*^{m533} chondrocytes were TUNEL+ (Fig. 2.7A,B), although cell shape changes were clearly evident at this stage (Fig. 2.2E); however, a much greater portion of IGP *kim*^{m533} chondrocytes was TUNEL+ (Fig. 2.7A,B). The defect in cell survival was MT-dependent, since nocodazole treatment significantly decreased the portion of TUNEL+ *kim*^{m533} chondrocytes (Fig. 2.7A,B). Electron microscopy (EM) analysis indicated that cell death was executed through the apoptotic pathway, which in chondrocytes is accompanied by membrane blebbing, patchy heterochromatin condensation at the nuclear periphery, and ultimately cell membrane disintegration (Roach et al., 2004) (Fig. 2.7C). qPCR analysis of unfolded protein response (UPR) pathway genes such as *bip* and *sil1* showed that cell death was not associated with ER stress (Fig. 2.7D), a potential cause of chondrocyte apoptosis. Rather, these results strongly suggest that that *kim*^{m533} chondrocyte apoptosis is primarily due to defective MT-dependent cell shape changes.

We tested whether cell shape changes were specifically dependent on MTs or whether actin also played a role. Although cortical F-actin was significantly altered after cytochalasin B treatment (Fig. 2.8A-C), cell shape was not affected in WT embryos, and *kim*^{m533} chondrocytes remained hourglass shaped (Fig. 2.8D-F). Thus we excluded F-actin as having a primary role in chondrocyte cell shape regulation.

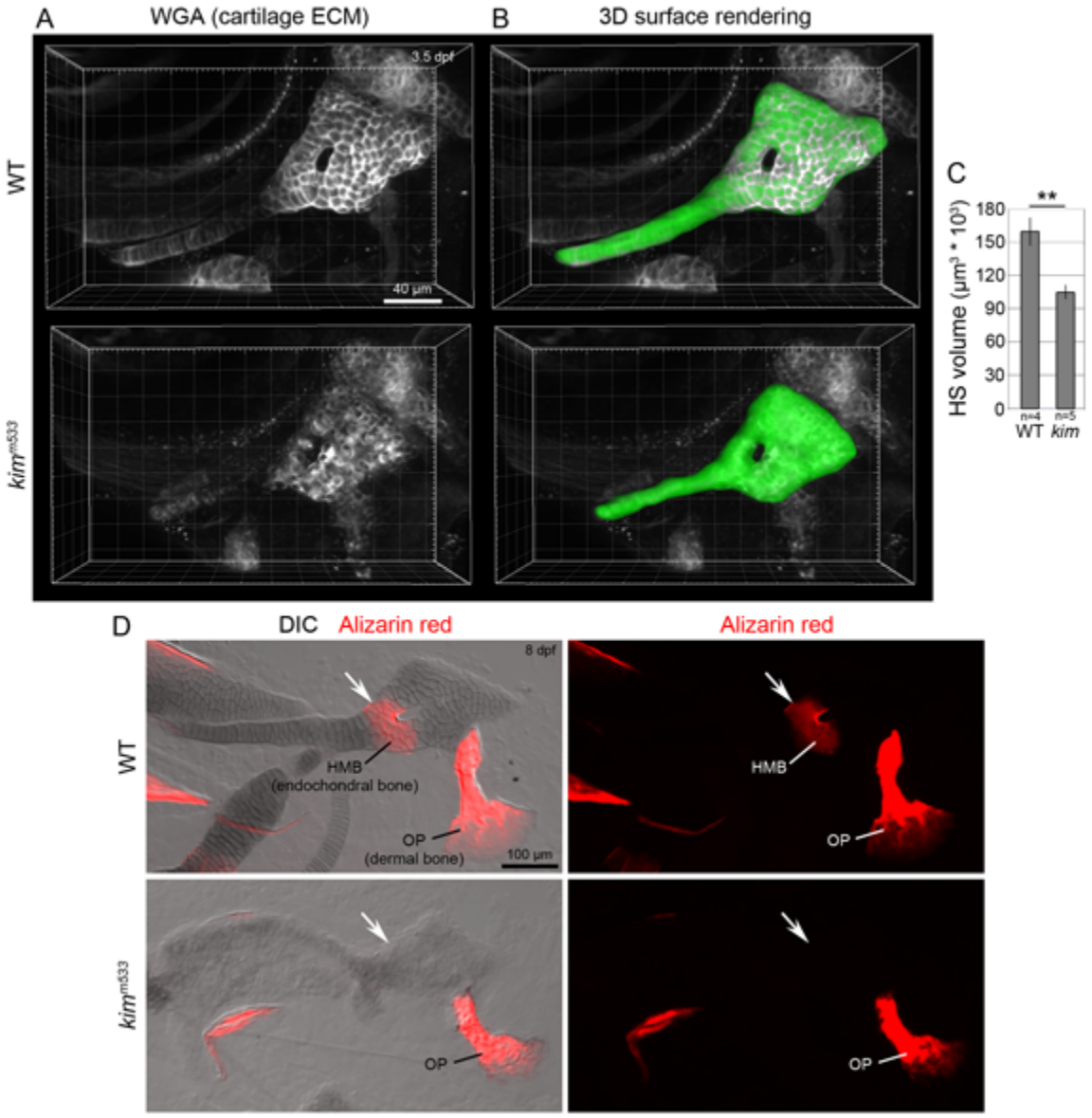

Figure 2.4. Cell shape dysregulation restricts cartilage growth and function.
(A,B) Confocal imaging and 3D rendering of HS cartilage at IGP. In *kim*^{m533} mutants, cell shape dysregulation leads to impaired organ growth. Confocal z-stacks of wheat-germ agglutinin (WGA) stained embryos (A) were used for rendering (B) and quantification (C). (D) Nomarski bright field and fluorescence microscopy of Alizarin red stained hyosymplectic (HS) show lack of endochondral bone formation in the hyomandibular bone (HMB) in *kim*^{m533} mutants (white arrows), whereas the dermal bones, such as the opercle (OP), are present. **p<0.01

Because mutant cell shape changes were suppressed by nocodazole treatment, we hypothesized that MT organization was altered in *kim*^{m533} chondrocytes. To test this possibility, we measured the angle of MT filaments relative to the long cell axis using immunofluorescence (IF) on cryosections (Fig. 2.9A), and categorized MTs either as being oriented parallel with (0-45°) or perpendicular to (45-90°) the long cell axis. WT chondrocytes exhibited radially arrayed MTs with about equal proportions of MTs oriented parallel and perpendicular to the long axis, while in *kim*^{m533} chondrocytes, 76% of MTs were parallel to the long axis (Fig. 2.9B,C). Nocodazole treatment of CP-EP WT chondrocytes (12hr, 0.6 μM) partially destabilized MTs (Fig. 2.9C), as indicated by increased non-filamentous fluorescence after aldehyde fixation (Mimori-Kiyosue et al., 2005), although a subpopulation of nocodazole-resistant MTs remained. Nocodozole treated *kim*^{m533} chondrocytes also exhibited destabilized MTs, and the orientation of the remaining nocodazole-resistant MTs was more similar to WT ($p=0.184$) than to DMSO-treated *kim*^{m533} chondrocytes ($p=0.012$) (Fig. 2.9B,C). These results indicate that polarized MTs contribute to the aberrant cell elongation.

To assess MT polarity, we analyzed the subcellular distribution of the MT plus-end binding protein EB3-GFP (Stepanova et al., 2003) and measured fluorescence intensity values at the cell cortex relative to non-cortical cytoplasm. WT chondrocytes displayed relatively homogenous distribution of EB3-GFP in the cytoplasm without cortical enrichment (Fig. 2.9D,E). Relative fluorescence levels were greatest in the cytoplasm and diminished at the cortical region of WT chondrocytes (Fig. 2.9D,F). In contrast, EB3-GFP localization in *kim*^{m533} cells was enriched in polarized cortical regions located at the

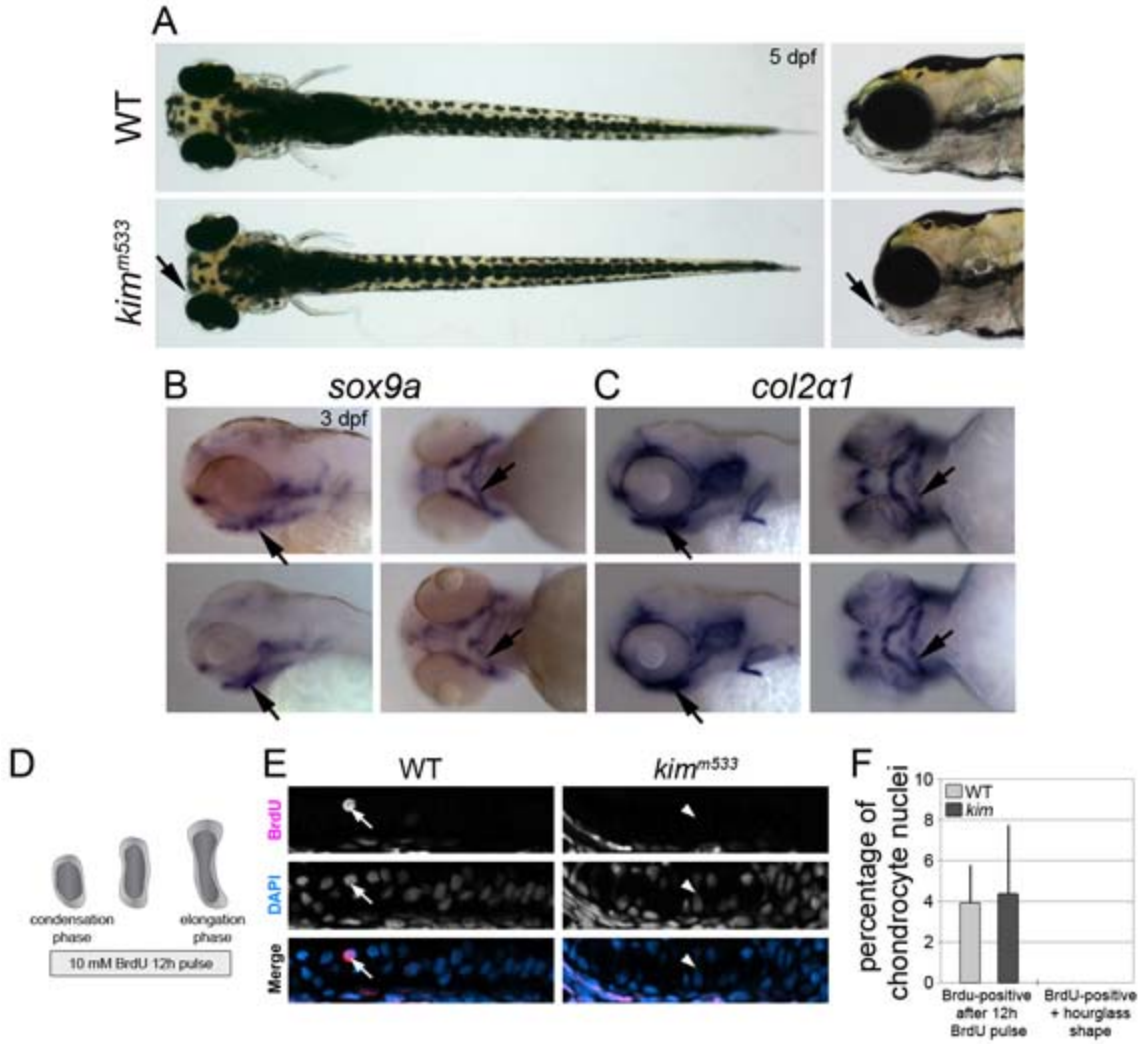

Figure 2.5. The *kimble* mutation impairs craniofacial cartilage growth after chondrocyte differentiation.
(A) *Kim*^{m533} mutant larvae (5 dpf) have a specific defect in jaw morphogenesis (arrow). (B,C) Whole mount *in situ* hybridization of chondrogenic differentiation transcription factor *sox9a* and cartilage ECM component *col2α1* at 3 dpf. No differences in spatiotemporal expression (arrows) were observed between WT and *kim*^{m533} embryos.

elongating ends of the cell (Fig. 2.9D,E). Relative fluorescence levels increased toward the cell edge and were highest at the cortical region in mutant cells, while they were diminished at constricted areas (Fig. 2.9D,F). Together, these data indicate that a subpopulation of nocodazole-sensitive, polarized MTs mediates kim^{m533} cell shape changes.

A nonsense mutation in zebrafish *kimble* embryos ablates Erc1 activity

To determine the mechanism of chondrocyte cell shape regulation, we used a positional cloning strategy to identify the *kim^{m533}* mutation (Knapik et al., 1998). After restricting the critical region to a 500 kb interval containing a single gene on the proximal arm of chromosome 4 (Fig. 2.10A), we identified a C>T transition at base pair 757 of *erc1* in *kim^{m533}* mutants, resulting in a Q253X nonsense mutation (Fig. 2.10B). Double-blinded genetic replacement experiments via mRNA injection and mosaic transgene expression confirmed that *erc1* expression was sufficient to restore normal jaw morphogenesis in *kim^{m533}* mutants (Fig. 2.10C) as well as rescue chondrocyte cell shape and survival cell autonomously (Fig. 2.10D-G). Consistent with cell autonomous function, whole mount *in situ* hybridization using riboprobes against the *erc1* 3' UTR showed enriched expression in developing cartilage, with prominent expression in EP pharyngeal cartilage (Fig. 2.10H). *Erc1* mRNA expression in chondrocytes was confirmed by RNA-Seq of fluorescent activated cell sorted (FACS) head chondrocytes (data not shown). Our cell shape analysis suggested that the Erc1 protein would be localized to a cellular domain where it could potentially influence MT organization. Erc1 localization has been shown

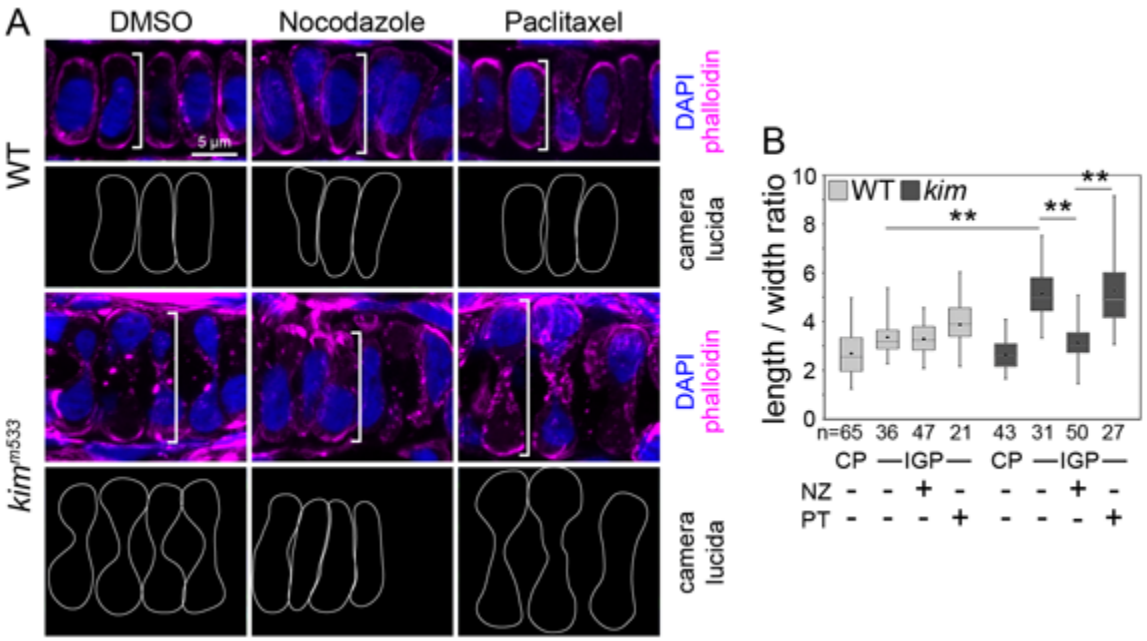

Figure 2.6. Destabilizing microtubules suppresses mutant cell shape changes.
(A) Imaging of cell (phalloidin) and nuclear (DAPI) shape after treatment with 1% DMSO (control), 0.6 µM nocodazole (NZ), or 20 µM paclitaxel (PT) from CP-IGP. Nocodazole suppresses *kim*^{m533} chondrocyte cell shape changes, but paclitaxel treatment of WT embryos does not phenocopy *kim*^{m533}. Brackets indicate representative chondrocytes. (B) Quantification of cell shape after indicated treatment. n values are number of cells analyzed from at least 3 animals.

to vary within different cultured cell lines (Monier et al., 2002; Ohara-Imaizumi et al., 2005; Lansbergen et al., 2006; Nomura et al., 2009), but its distribution in non-neuronal cells *in vivo* has not been reported. Using IF we found that endogenous Erc1 is present at the cell cortex in discrete puncta within WT chondrocytes (Fig. 2.10I). We performed 3D rendering of confocal z-stacks of whole cartilage IF and distance mapped Erc1 voxels relative to the plasma membrane (PM), which was marked by caax-eGFP. Our results show that most Erc1 puncta were less than 1 μm from the PM (93.8 ± 4.7%, 95% CI, n=145) (Fig. 2.10J,K). By performing parallel Erc1 IF on WT and *kim*^{m533} chondrocytes followed by confocal imaging using identical microscope settings, we observed nearly complete loss of Erc1 signal in *kim*^{m533} chondrocytes (Fig. 2.10L), indicating that the *kim*^{m533} mutation is an *erc1* null allele. We confirmed that the Erc1 antibody recognizes the zebrafish Erc1 protein using western blot detection of a GFP fusion construct (Fig. 2.10M), and subsequent western blot analysis of endogenous Erc1 showed that *kim*^{m533} lysates lacked one of two closely migrating bands at approximately 130 kDa (Fig. 2.10N), consistent with predicted molecular weight. The remaining band in *kim*^{m533} lysates likely represents Erc2, a closely related but neuron-specific Erc family member (Wang et al., 2002). This notion is supported by the fact that *kim*^{m533} embryos exhibit strong signal in the brain by IF (data not shown), despite loss of signal in chondrocytes. In summary these data show Erc1 is expressed in chondrocytes, where it localizes to the cell cortex and functions cell autonomously to regulate cell shape.

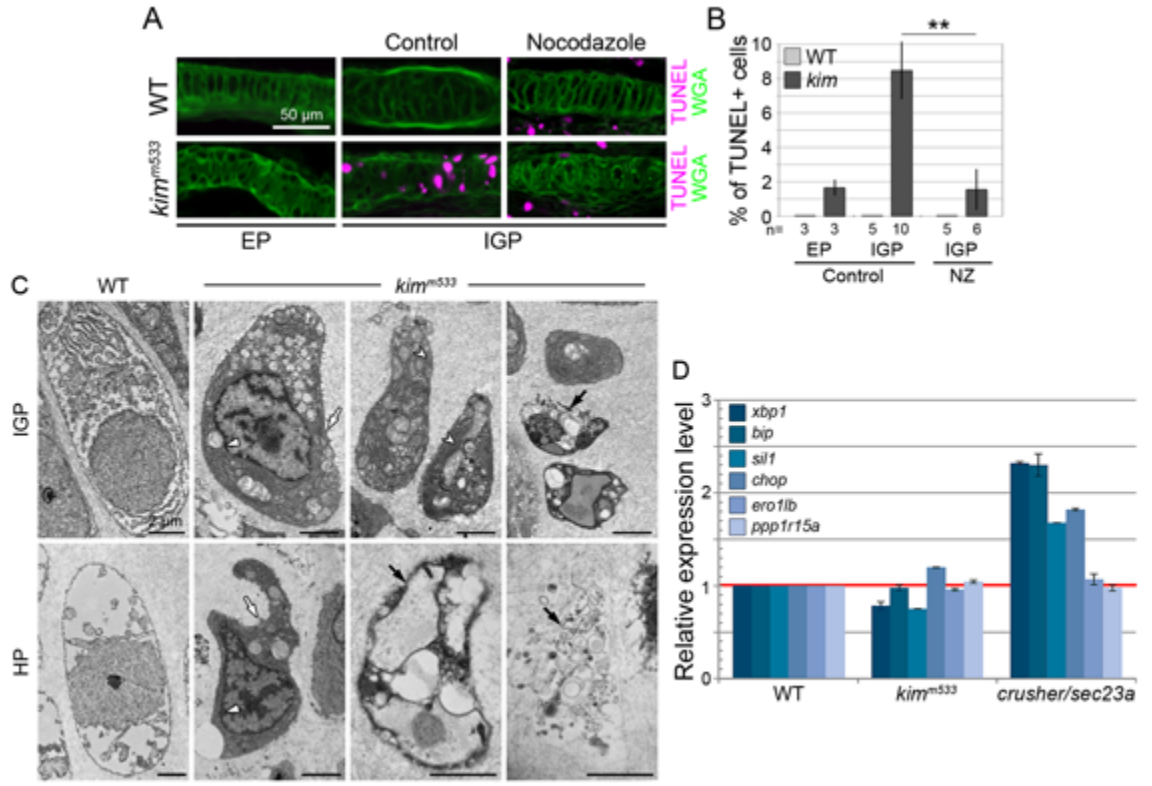

Figure 2.7. Destabilizing microtubules suppresses *kim*^{m533} chondrocyte apoptosis. (A,B) TUNEL assay and quantification of chondrocyte cell death. Nocodazole treatment suppresses *kim*^{m533} chondrocyte cell death. (C) EM analysis of cell death, which shows morphological characteristics of chondrocytes apoptosis in *kim*^{m533} chondrocytes, including heterochromaton condensation at nuclear periphery (arrowhead), rER condensation (concave arrowhead), membrane blebbing (white arrow), and disintegration of the PM with release of the cytoplasm content into the extracellular space (black arrow). (D) qRT-PCR analysis of fold expression change of ER-stress-related transcripts in IGP *kim*^{m533} and *crusher* (*sec23a* (Lang et al., 2006), positive control) mutants compared to WT embryos. Data are normalized to β-actin and then to WT. **p<0.01

Erc1 regulates cell shape and growth by directing ECM vesicular cargo traffic

Given that Erc1 regulates vesicular traffic in cultured cells (Grigoriev et al., 2007, 2011), we asked whether impaired cell shape regulation in *kim*^{m533} chondrocytes stems from defects in exocytosis, reasoning that membrane delivery to the cell surface could provide a plausible mechanism for cell shape changes (He et al., 2007). As an indicator of impaired exocytosis, we examined vesicle retention at the cell cortex by EM analysis of EP chondrocytes. While both WT and *kim*^{m533} chondrocytes displayed hallmarks of highly secretory cells such as extensive rER, *kim*^{m533} chondrocytes also contained abundant small, electron-dense vesicular structures (Fig. 2.11A) that were concentrated at the cell cortex ($\bar{x} = 0.597 \pm 0.084$ μm from cell membrane, 95% CI, n=121). Similar vesicles were present in wild types, but they were significantly more abundant in *kim*^{m533} chondrocytes (Fig. 2.11A,B).

We expected exocytic vesicle accumulation to result in ECM protein backlog in the cytoplasm since chondrocytes are exclusively responsible for cartilage ECM secretion. To test this, we labeled type II collagen with IF and glycosaminoglycans (GAGs) with wheat germ agglutinin (WGA), a lectin binding to sialic acid and *N*-acetylglucosaminyl residues of proteoglycans abundant in cartilage ECM (Lang et al., 2006). In WT cartilage, type II collagen and proteoglycans were localized primarily in the ECM but were also present in perinuclear and subcortical areas, which likely represent traffic through the secretory pathway (Fig. 2.11C). In *kim*^{m533} cartilage, although ECM components were present in the extracellular space, large amounts were intracellular (Fig.

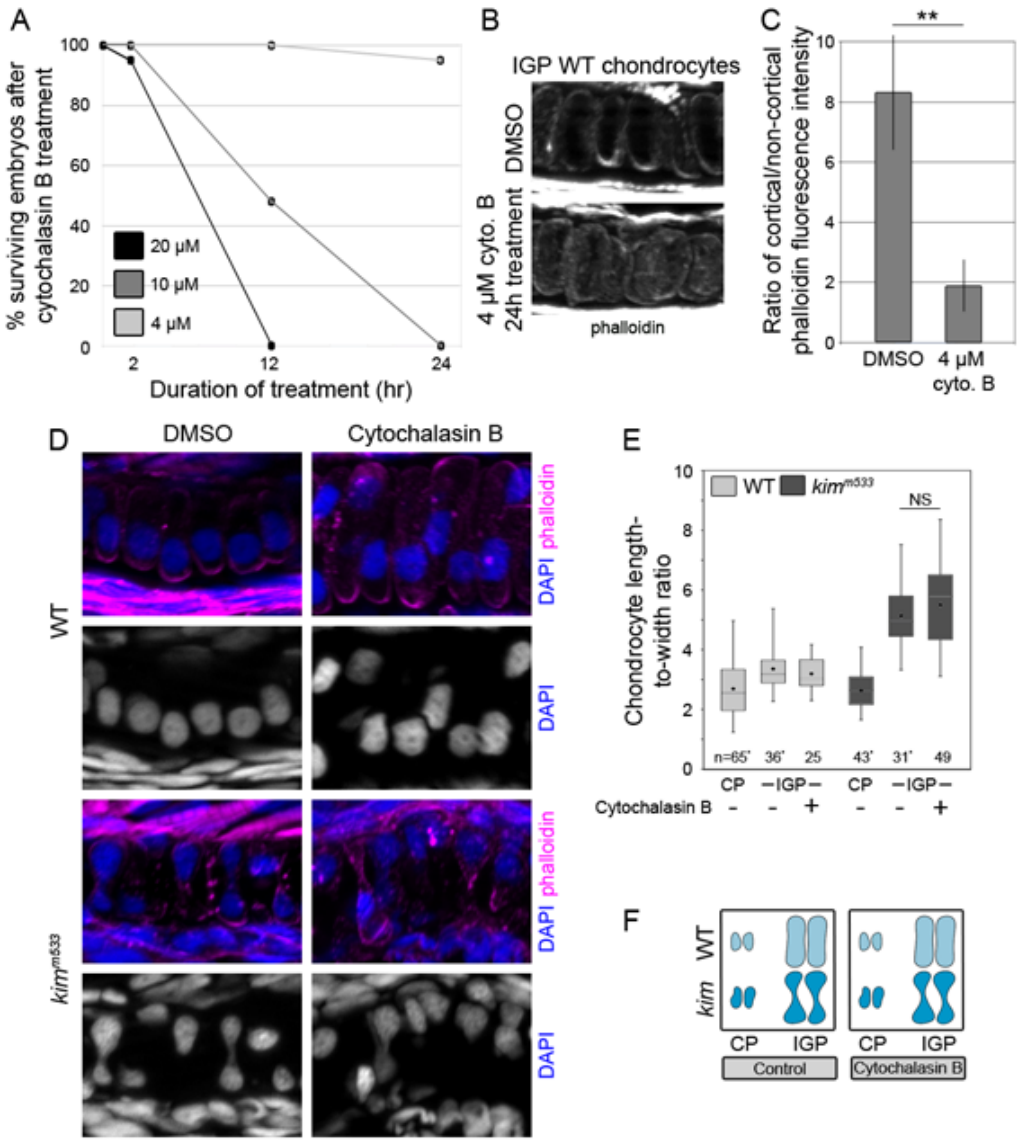

Figure 2.8. Cytochalasin B treatment does not affect chondrocyte cell shape. (A) Survival curve after CP-IGP treatment of WT embryos with 4, 10, and 20 µM cytochalasin B. 4 µM was chosen for experiments in this study due to toxicity associated with higher concentrations. (B) Phalloidin staining of F-actin in chondrocytes after CP-IGP treatment with 4 µM cytochalasin B or 1% DMSO. Cytochalasin B treatment led to increased non-cortical labeling with phalloidin, indicating a redistribution of F-actin relative to DMSO-treated chondrocytes. (C) Quantification of phalloidin cortical enrichment. Data are presented as an average ratio of cortical (0-500 nm from cell edge) fluorescence intensity relative to non-cortical, cytoplasmic (> 500 nm from cell edge) intensity. (D) Cortical (phalloidin) and nuclear (DAPI) labeling of WT and *kim*^{m533} embryos after CP-IGP treatment with 1% DMSO or 4 µM cytochalasin B. (E) Quantification of chondrocyte cell shape after 4 µM cytochalasin B treatment. Data for control groups (non-cytochalasin B treated) are the same data set as presented in Fig. 3b. (F) Schematic illustrating cell shape changes after cytochalasin B treatment. **p<0.01

2.11C), suggesting that ECM secretion is impaired but not abolished. To assess ECM secretion quantitatively, we labeled proteoglycans with WGA and measured fluorescence intensity levels of the chondrocyte cytoplasm relative to that of the surrounding ECM. As expected, *kim*^{m533} chondrocytes had significantly higher levels of intracellular proteoglycans compared to wild types (Fig. 2.11D,E). After nocodazole treatment, *kim*^{m533} chondrocytes had comparable levels of intracellular proteoglycans as wild types (Fig. 2.11D,E), suggesting that MT destabilization suppresses ECM traffic backlog.

If chondrocyte cell shape regulation depends primarily on cargo traffic, then inhibiting other components that function in Erc1-dependent exocytosis should also impair cell shape changes. To test this possibility, we used dominant negative approaches to inhibit the exocytic vesicle component Rab8a (Wakana et al., 2012) and Kinesin-1, which both function in vesicle traffic to Erc1 cortical platforms (Grigoriev et al., 2007, 2011). We cloned zebrafish *rab8a* and made a dominant negative (DN) allele (Rab8aT22N) by introducing a variant in the G1 domain (Fig. 2.12A) (Peränen et al., 1996). We then generated mosaic transgenic WT embryos by expressing either eGFP-Rab8a or DN eGFP-Rab8aT22N in individual chondrocytes and performed cell shape analysis (Fig. 2.12A). eGFP-Rab8a exhibited a subcellular localization similar to mammalian cells (Grigoriev et al., 2011), with perinuclear and cortical enrichment along with diffuse cytoplasmic distribution, and overexpression did not lead to chondrocyte cell shape changes (Fig. 2.12B,D). Conversely, DN eGFP-Rab8aT22N expression resulted in cell shape defects highly similar to *kim*^{m533} chondrocytes, and just as with *kim*^{m533} chondrocytes DN eGFP-Rab8aT22N-mediated shape changes were suppressed by

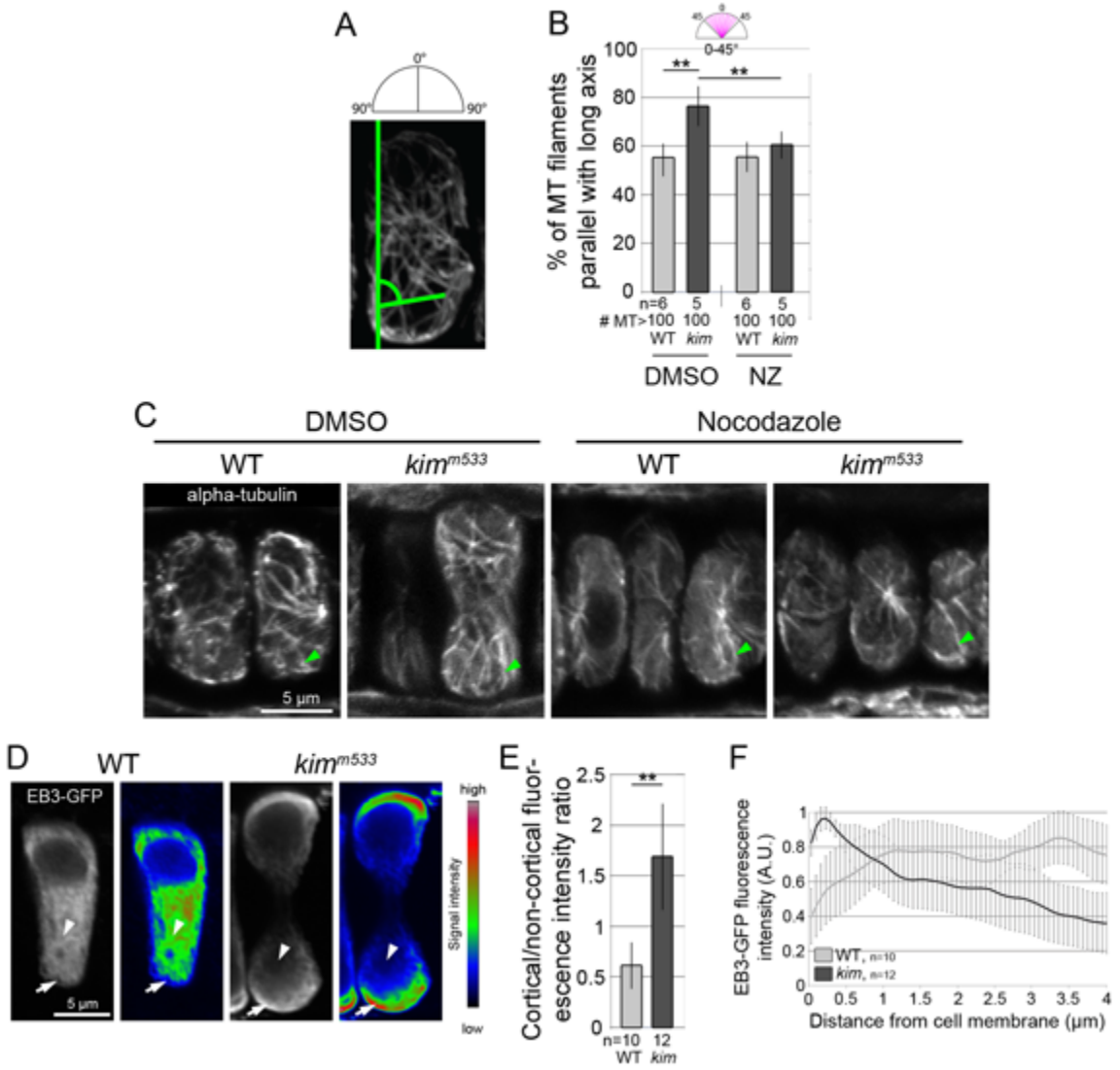

Figure 2.9. Microtubules are polarized toward growing cell ends in *kim*^{m533} chondrocytes.

(A) Schematic illustration of MT (alpha-tubulin) orientation relative the long cell axis. (B,C) Quantification and imaging of MT orientation in EP chondrocytes treated with 1% DMSO or 0.6 µM nocodazole for 12 hr. Control *kim*^{m533} chondrocytes have more MTs oriented toward the growing ends compared to WT, but nocodazole resistant *kim*^{m533} MTs are similar in orientation to WT. Green arrowheads show examples of MTs parallel with long cell axis. (D) 8-bit grayscale and pseudo-colored LUT (lookup table) image of EB3-GFP in EP chondrocytes. *kim*^{m533} chondrocytes show enriched localization at the polarized ends (arrows) and diminished signal in the non-cortical cytoplasm (arrowhead). (E) Quantification of EB3-GFP localization. Data are presented as an average ratio of cortical (<0.5 µm from cell edge) mean fluorescence intensity relative to non-cortical, cytoplasm (0.5-4 µm from cell edge). Image selections were taken parallel to the long cell axis. (F) Plot of normalized EB3-GFP mean fluorescence intensity values relative to position from cell edge using the same data set as panel E. **p<0.01

destabilizing MTs (Fig. 2.12B,D). To further test the role of the exocytic pathway in cell shape, we cloned zebrafish *kif5Ba*, which encodes the motor domain of Kinesin-1 (Campbell and Marlow, 2013), and made a DN allele by deleting the head domain at amino acid 332 (Fig. 2.12A) (Uchida et al., 2009). As with Rab8a, DN Kinesin-1 overexpression in WT cartilage recapitulated *kim*^{m533} chondrocyte cell shape in a MT-dependent manner (Fig. 2.12C,D). These data indicate that cell shape changes following chondrocyte differentiation depend on Kinesin-1-dependent traffic of Rab8 vesicular carriers to Erc1 cortical platforms.

Cargo traffic through Rab11 recycling compartments contributes to polarized cell growth

To determine how loss of Erc1 disrupts cell shape changes, we performed time lapse confocal imaging of chondrocytes' plasma membrane in live embryos using a caax-eGFP transgene. We found that WT chondrocytes exhibit subtle cell membrane movements that lead to proportional growth in length and width over a period of 3-4 hours (Fig. 2.13A-C). In contrast to wild types, *kim*^{m533} chondrocytes grew in cell length but collapsed in cell width. Most *kim*^{m533} chondrocytes progressively decreased in width over time, while others exhibited oscillatory patterns of expansion and contraction before ultimately collapsing in width (Fig. 2.13A-C).

Because *kim*^{m533} chondrocytes exhibited a specific defect in maintain cell width, we hypothesized that cell shape changes were caused by removal of plasma membrane from the lateral sides of the cell. We reasoned that membrane recycling may contribute to cell growth by uptake and subsequent redelivery of membrane and cargo to the cell surface.

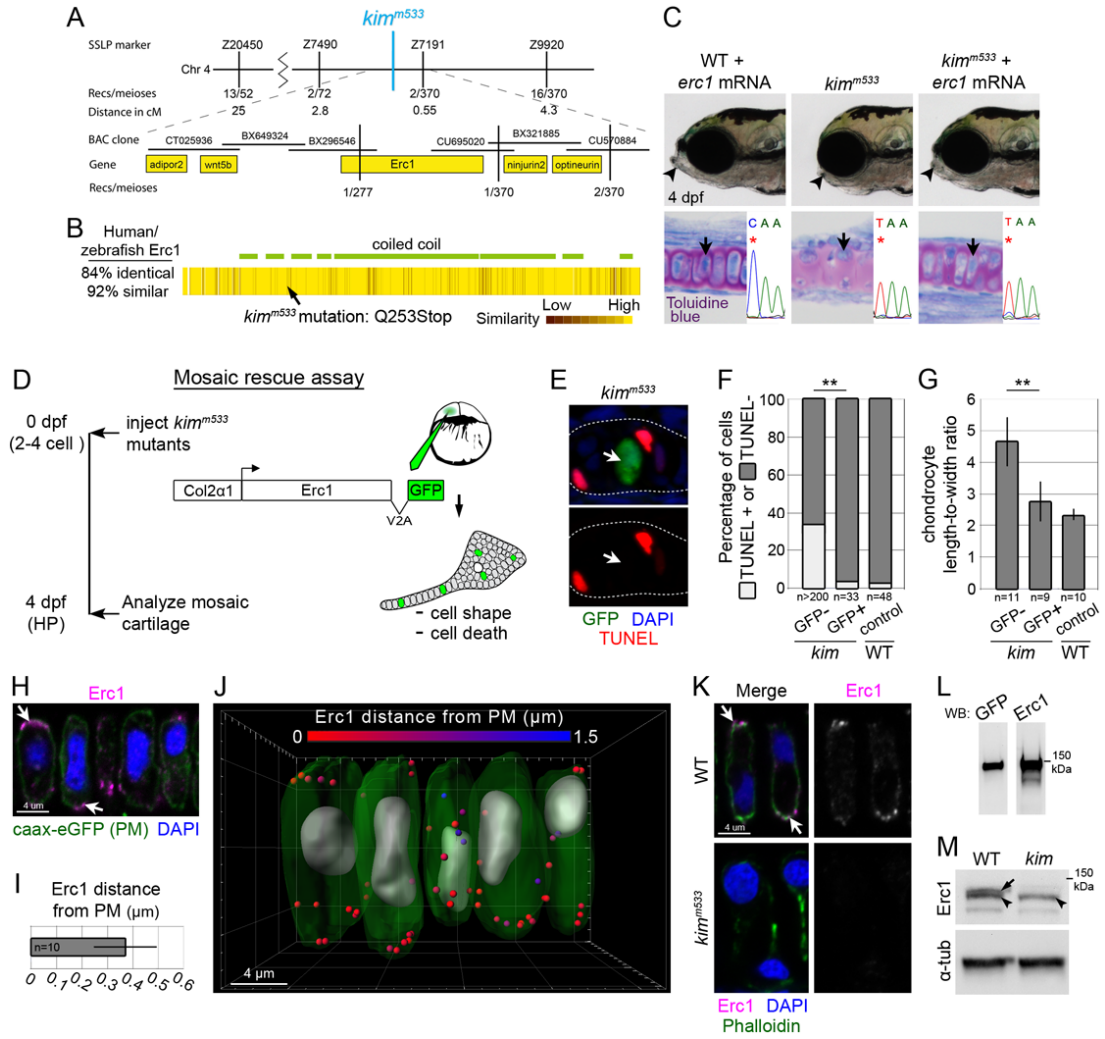

Figure 2.10. The *kimble* mutation disrupts Erc1, a chondrocyte cell cortex protein. (A) Schematic illustration of the *kim*^{m533} mutation critical interval. (B) Heat map schematic of Erc1 amino acid conservation. (C) Expression of WT *erc1* mRNA in *kim*^{m533} mutant embryos rescues jaw morphogenesis (arrowhead) and cell shape (arrow). Analyzed embryos were genotyped (asterisks). (D) Schematic illustrating mosaic rescue assay used for testing cell-autonomous function. Rescue construct *col2α1:erc1-v2a-eGFP* drives expression of untagged Erc1 in chondrocytes, and v2a-eGFP reporter marks transgenic cells. (E-G) *Erc1* expression cell-autonomously suppresses *kim*^{m533} chondrocyte cell death (E,F) and shape changes (G). (H) *Erc1* mRNA expression is enriched in cartilage, including the neurocranium (arrow) and pharyngeal skeleton (arrowhead). (I) Endogenous Erc1 protein (magenta) is localized in close proximity to the chondrocyte plasma membrane (PM). (J,K) Quantification and 3D reconstruction of Erc1 localization. (L) Erc1 protein expression is lost in *kim*^{m533} chondrocytes. (M) Erc1 antibody recognizes zebrafish fusion protein in western blots of *eGFP-erc1* injected embryo lysates. (N) Western blot analysis of Erc1 protein expression in WT and *kim*^{m533} lysates. *Kim*^{m533} lysates show loss of immuno-reactivity of one of the two prominent bands (arrow) close in molecular weight between 100-150 kDa. The second band (arrowhead) is unaffected. Uncropped blot images are in Fig. S5. **p<0.01

To test this hypothesis, we inhibited the recycling pathway by expressing dominant negative Rab11a. We generated mosaic transgenic WT and *kim*^{m533} embryos expressing eGFP-Rab11a or DN eGFP-Rab11aS25N (Fig. 2.13D) in isolated or small clones of chondrocytes. This approach eliminates potential non-cell-autonomous effects on cell shape, and it allows use of neighboring non-transgenic chondrocytes for an internal control for quantitative cell shape analysis in *kim*^{m533} mutants. eGFP-Rab11a in WT chondrocytes exhibited a subcellular localization similar to that of many mammalian cell-types, with cortical and perinuclear enrichment that partially overlapped with intracellular proteoglycans (Fig. 2.13E), suggesting they may represent sorting compartments and post-Golgi vesicles. In *kim*^{m533} chondrocytes, eGFP-Rab11a was more homogenously distributed in the cytoplasm along with the accumulated proteoglycans present in mutant cells (Fig. 2.13E). In contrast to eGFP-Rab11a, which did not alter chondrocyte cell shape, expression of DN eGFP-Rab11aS25N suppressed *kim*^{m533} chondrocyte cell shape changes. Transgenic *kim*^{m533}*;eGFP-rab11aS25N* chondrocytes were more similar to WT cells than to their neighboring non-transgenic control *kim*^{m533} chondrocytes (Fig. 2.13E,F). Collectively, our data indicate that Erc1 functions at the chondrocyte cell cortex to regulate cell growth via MT organization and cargo trafficking from Rab11-positive recycling compartments.

Discussion

In this study we present in vivo analysis of cell shape changes occurring in a mesenchymal cell-type, chondrocytes, during differentiation and organ morphogenesis in

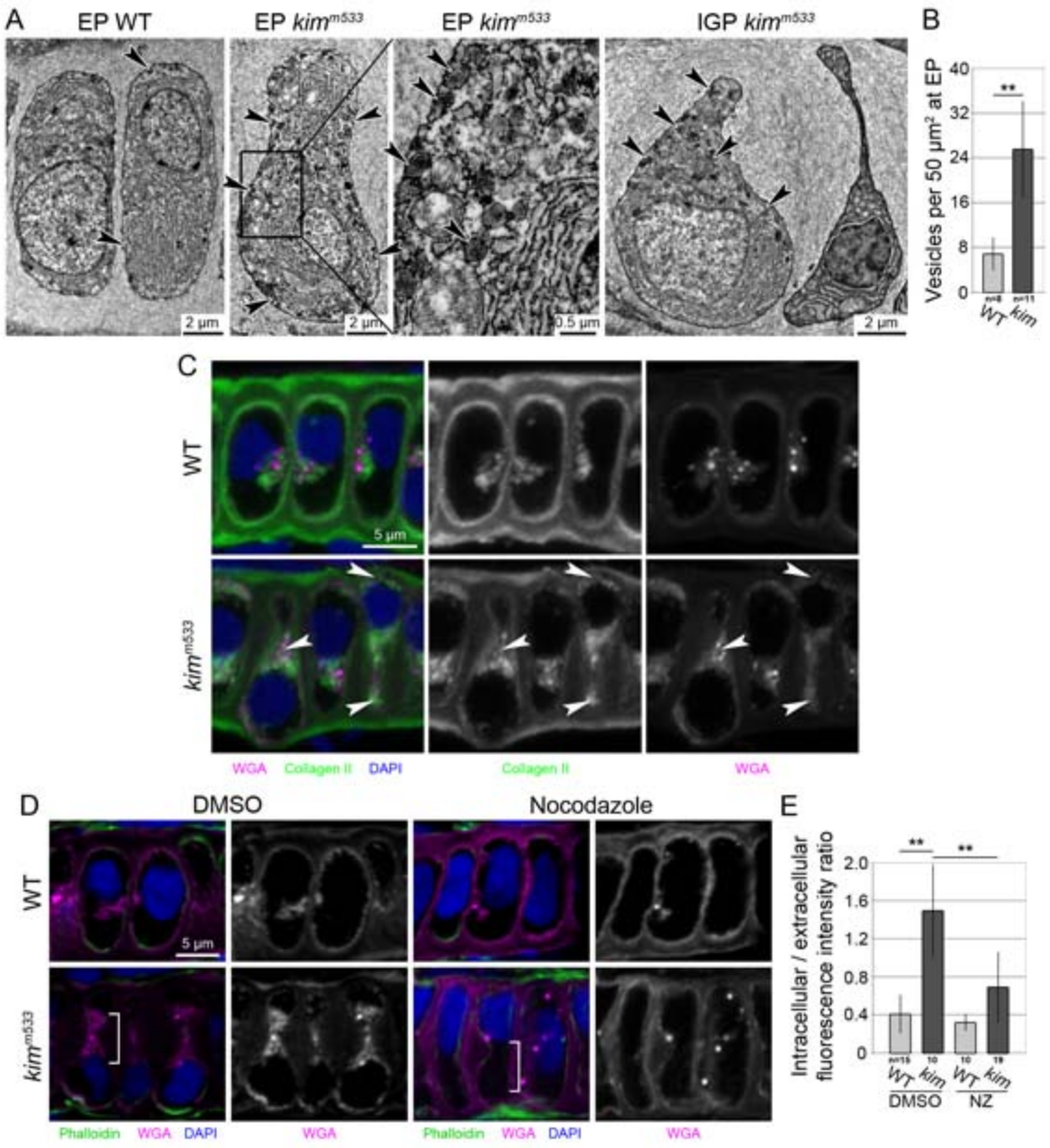

Figure 2.11. ECM cargo trafficking is impaired in *kim*^{m533} chondrocytes.
(A,B) EM analysis and quantification of cortical vesicle accumulation. The boxed region of the second panel is shown in higher magnification in the third panel, and arrowheads point to accumulating vesicular structures. (C) IF of type II collagen (green) and proteoglycans (WGA, magenta) on EP WT and *kim*^{m533} chondrocytes. Arrowheads indicate intracellular localization of ECM cargo in *kim*^{m533} chondrocytes. (D,E) Fluorescence microscopy and quantification of proteoglycans (WGA, magenta) localization. Graph represents the ratio of average intracellular WGA fluorescence ratio divided by that of the surrounding ECM. Nocodazole (NZ) treatment suppresses proteoglycan retention in *kim*^{m533} chondrocytes (brackets). **p<0.01

a zebrafish model. Cell shape regulation in mesenchymal cells (e.g. fibroblasts, myocytes, chondrocytes, mesenchymal stem cells) is poorly understood and likely differs from epithelia, which rely heavily on cell-cell interactions for shape changes. Here, we have identified a new pathway regulating growth of mesenchymal cells that relies on Erc1-dependent microtubule (MT) organization and cargo transport to the plasma membrane. We observed that in the absence of Erc1, a large scaffolding protein localized to subcortical regions, chondrocytes lengthen but fail to maintain cell width, thereby forming elongated but collapsed cells that subsequently undergo cell death and compromise organ function. We propose a working model where Erc1-dependent MT organization directs the delivery of vesicular cargo (lipids and proteins) to the plasma membrane, sculpting small round progenitors into large rectangular mature cells. Regulation of endo- and exocytic membrane recycling ensures proportional cell growth in mature chondrocytes. Cargo traffic serves the dual functions of regulating cell shape changes and cartilage ECM deposition that occur simultaneously during chondrocyte differentiation, promoting rapid organ growth with negligible impact from cell division.

The cytoskeleton is an important regulator of cell shape. Studies in *Ciona intestinalis* notochord cells have linked actomyosin-based mechanisms to cell elongation (Sehring et al., 2014). Conversely work in HeLa cells and cultured drosophila S2R+ cells distinguished that an actomyosin-based mechanism is not involved in cell elongation, but instead is dependent on polarized MTs (Picone et al., 2010). Two potential mechanisms could account for expansion of plasma membrane by MTs: 1) mechanical stretching or 2)

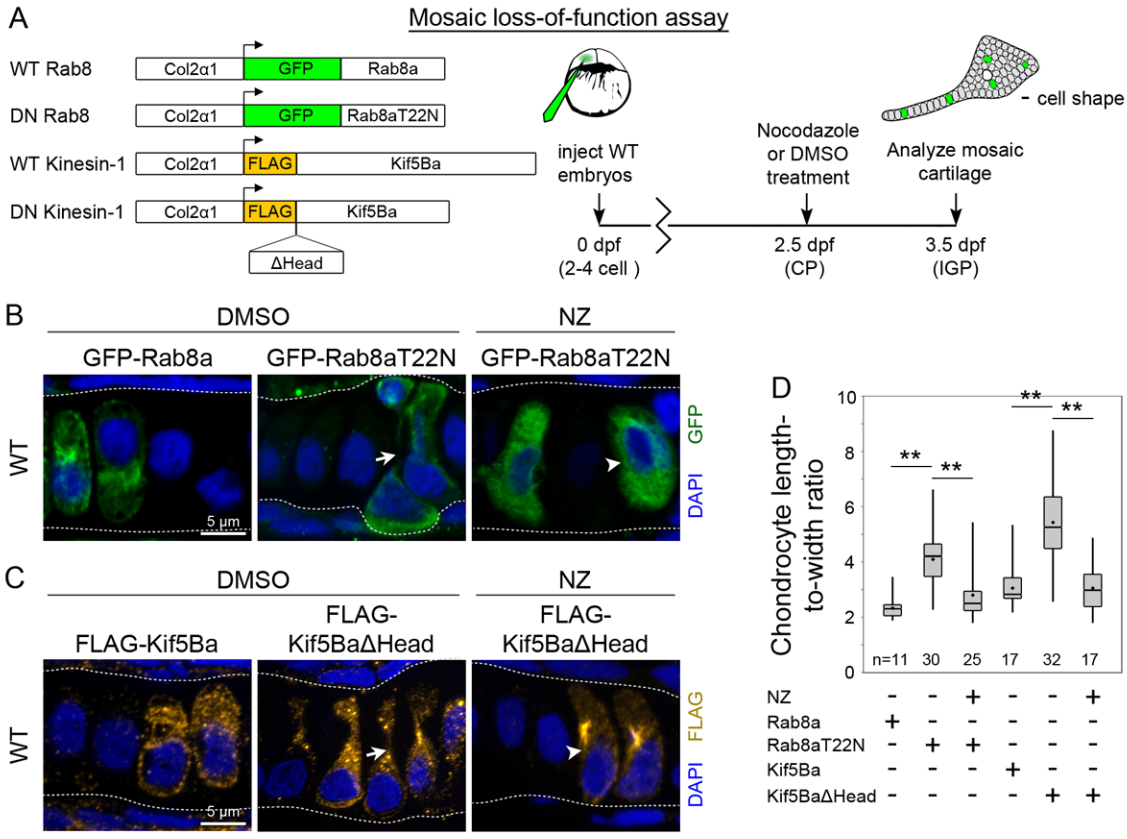

Figure 2.12. Inhibiting exocytic components phenocopies *kim*^{m533} cell shape. **(A-D)** Mosaic expression of dominant negative GFP-Rab8aT22N or FLAG-Kif5BaΔHead in WT chondrocytes phenocopies *kim*^{m533} chondrocyte cell shape changes (arrows). Nocodazole (NZ) treatment suppresses cell shape changes in GFP-Rab8aT22N and FLAG-Kif5BaΔHead-expressing chondrocytes (arrowheads). **p<0.01

directed addition to the plasma membrane. Studies indicate that the latter hypothesis is more likely to be correct. For example, experiments testing plasma membrane mechanical properties revealed that cells are not sufficiently elastic for growth to be facilitated by stretching (Morris and Homann, 2001), and plasma membrane addition was shown to contribute to cell growth in NIH3T3 cells (Gauthier et al., 2009). It is plausible that MTs regulate cell growth/length by functioning as a conduit for directed membrane cargo delivery, but the specific protein complexes that regulate this process were unknown. Here, we used an unbiased forward genetics approach and showed that in the absence of Erc1, chondrocytes elongate but collapse in width (Fig. 2.12A-C), resulting in circumferential growth at polarized cell ends (Fig. 2.3A-B). The cell shape changes of Erc1-deficient chondrocytes is mediated by a subpopulation of dynamic MTs that are oriented toward the growing ends of cells. Nanomolar concentrations of nocodazole that do not affect cell shape in normal chondrocytes are sufficient to destabilize polarized MTs in Erc1-deficient cells and restore normal shape. Our model also addresses how changes in MT polarity lead to cell shape dysregulation. We propose that vesicular traffic from the recycling pathway is directed to polarized ends along MT tracks but is not delivered to lateral sides of the cell, resulting in cell elongation but not width expansion. Erc1 has been shown to promote exocytosis by acting as a positive regulator of vesicle docking at the cell cortex in *in vitro* experiments (Grigoriev et al., 2007, 2011). In Erc1-deficient chondrocytes, we observed a three-fold increase in the accumulation of cortical vesicles (Fig. 2.11A,B), as well as an accumulation of intracellular ECM cargo (Fig. 2.11C), supporting a conserved function of Erc1 in promoting vesicle trafficking. However, Erc1 likely only plays an auxiliary role in chondrocyte exocytosis since *kim*^{m533}

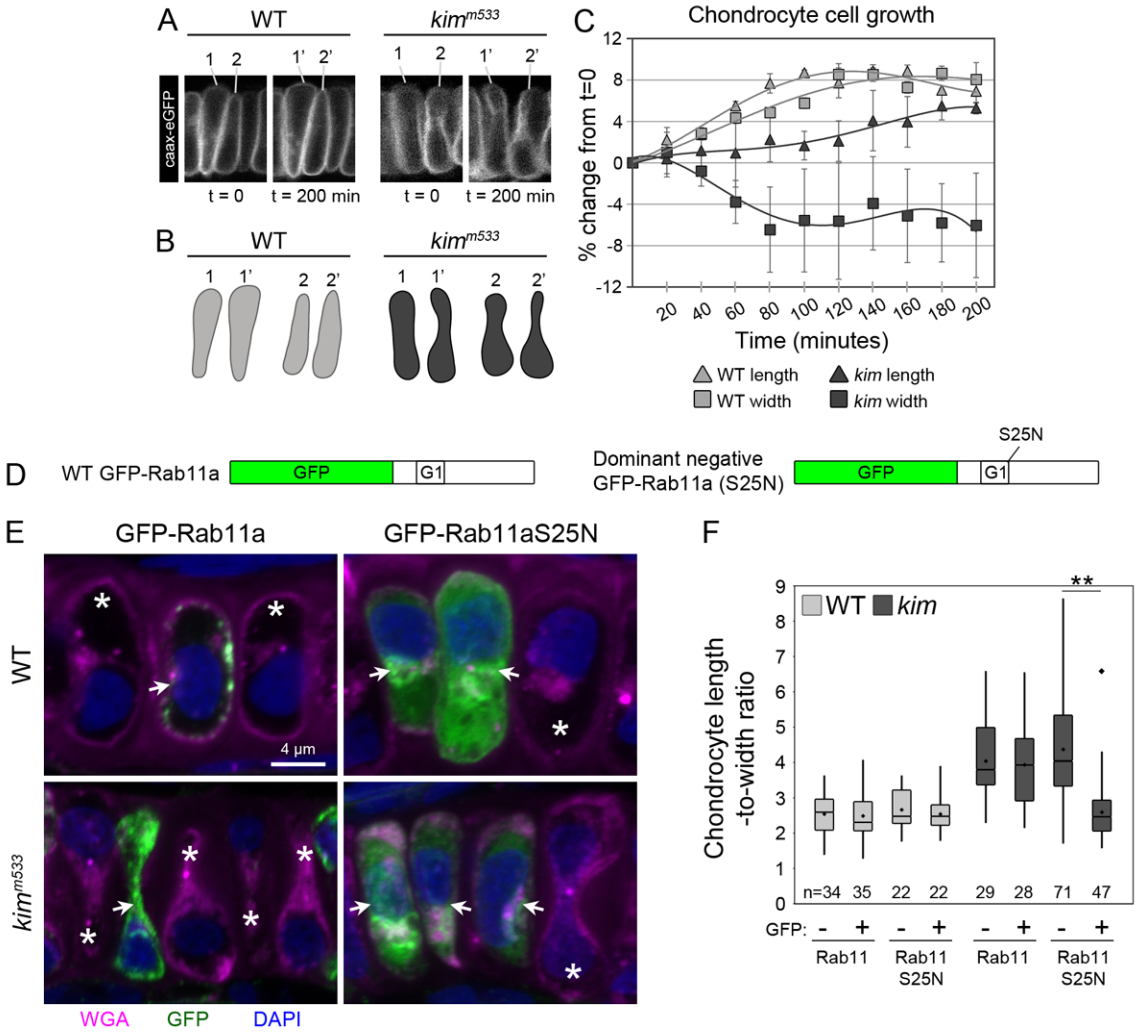

Figure 2.13. Inhibiting Rab11 function suppresses chondrocyte cell width collapse cell-autonomously.

(A-C) Time-lapse imaging of chondrocyte cell shape changes. Individual frames WT and *kim*^{m533} Tg(col2a1:caax-eGFP) symplectic cartilage at t=0 and t=200 minutes (A). Camera lucida drawings of the cell membrane (B). Quantification of cell shape chondrocyte cell shape changes from time-lapse analysis (C). (D-F) Mosaic expression of dominant negative eGFP-Rab11aS25N rescues *kim*^{m533} chondrocyte shape cell-autonomously. IF of transgenic (GFP+, white arrows) and non-transgenic (GFP-, asterisks) neighboring chondrocytes (A) was used for quantitative analysis of cell shape (B). n-values are total number of cells analyzed from a minimum of 4 animals. **p<0.01

cartilage appears to have ECM deposition as confirmed by EM, histology, and IF analysis.

We also discovered that loss of membrane in the middle of the cell creating an "hourglass" shape stems from Rab11-dependent mechanisms. In our experiments inhibiting the function of Rab11, a critical regulator of the recycling pathway (Welz et al., 2014), suppresses *kim*^{m533} cell shape changes (Fig. 2.13E,F). We postulate that chondrocyte cell shape changes depend on traffic through Rab11-positive recycling compartments, which deliver new membrane/specialized cargo to the cell surface. In Erc1-deficient chondrocytes, cargo traffic is skewed towards polarized ends due to changes in MT polarity.

Our study provides unique insight to regulation of cell behaviors during differentiation and organ growth, especially how changes in cell behavior are executed during the transition from a progenitor to a mature differentiated cell. In the case of chondrocytes, this transition involves high-level trafficking and secretion of ECM cargo proteins, as well as polarized cell growth. Our data indicate that both processes are tightly linked and co-regulated during chondrocyte differentiation, where cargo trafficking controls both ECM formation and proper cell shape. We previously found that inhibiting ER-to-Golgi traffic arrests cell growth, forming small round chondrocytes that do not secrete ECM proteins (Sarmah et al., 2009, Lang et al., 2006). In this study, we found that inhibiting post-Golgi trafficking has a different effect, forming highly elongated chondrocytes due to changes in MT polarity. We propose that high secretory activity, with lipid and protein

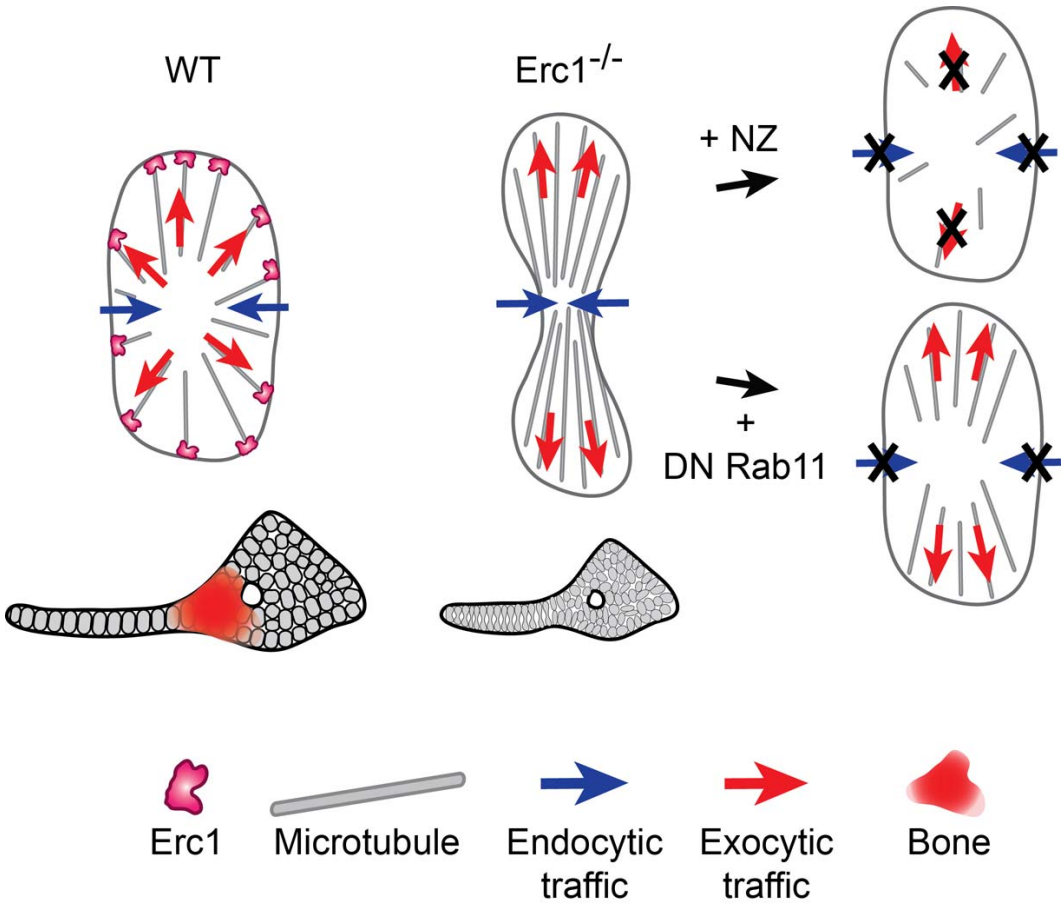

Figure 2.14. Model of chondrocyte cell shape regulation.
Small, round mesenchymal progenitors differentiate into elongated chondrocytes to promote organ growth and function. Cargo trafficking has dual functions of regulating ECM formation and polarized cell growth during differentiation. At the cell cortex, Erc1 spatially regulates cargo trafficking from endo/exocytic recycling by balancing MT polarity and organization, acting in a cell autonomous manner. In Erc1-deficient chondrocytes, MT orientation is skewed toward the long cell axis, and cargo delivery from Rab11-positive recycling compartments is enriched toward polarized cell ends. Destabilizing polarized MTs with low concentrations of nocodazole rescues cell shape, possibly by inhibiting cargo traffic. Dominant negative Rab11 expression suppresses cell width collapse by inhibiting endocytic recycling.

cargos being continuously delivered to the cell surface, promotes cell growth in newly differentiated chondrocytes. However, regulation of post-Golgi traffic along MT tracks determines to which areas of the plasma membrane cargos are delivered in order to direct cell shape changes. According to this model, cargo traffic regulation at different levels of the secretory pathway acts as both positive and negative regulators of cell growth. Future studies of cell autonomous mechanisms integrating the components of the endocytic and secretory pathways will be needed to understand the complex pathways regulating cell and organ growth.

CHAPTER III

ANIMAL MODEL OF SAR1B DEFICIENCY PRESENTS LIPID ABSORPTION DEFICITS SIMILAR TO ANDERSON DISEASE

Daniel S. Levic[1,2], JR Minkel[1], Wen-Der Wang[1,3], Witold M. Rybski[1], David B. Melville[1,2,4] and Ela W. Knapik[1,2,#]

[1]Department of Medicine, Division of Genetic Medicine; [2]Department of Cell and Developmental Biology, Vanderbilt University Medical Center, Nashville, TN 37232, USA

Present Address: [3] Department of Bioagricultural Science, National Chiayi University, Chiayi 60004, Taiwan;

[4]Department of Molecular and Cell Biology, University of California at Berkeley, CA 94720-3370, USA

This chapter was published under this title in *The Journal of Molecular Medicine* (Levic et al., 2015).

Abstract

Anderson Disease (ANDD) or Chylomicron Retention Disease (CMRD) is a rare, hereditary lipid malabsorption syndrome associated with mutations in the *SAR1B* gene

that is characterized by failure to thrive and hypocholesterolemia. Although the SAR1B structure has been resolved and its role in formation of coat protein II (COPII) coated carriers is well established, little is known about the requirement for *SAR1B* during embryogenesis. To address this question, we have developed a zebrafish model of Sar1b deficiency based on antisense oligonucleotide knockdown. We show that zebrafish *sar1b* is highly conserved among vertebrates, broadly expressed during development, and enriched in the digestive tract organs, brain and craniofacial skeleton. Consistent with ANDD symptoms of chylomicron retention, we found that dietary lipids in Sar1b deficient embryos accumulate in enterocytes. Transgenic expression analysis revealed that Sar1b is required for growth of exocrine pancreas and liver. Furthermore, we found abnormal differentiation and maturation of craniofacial cartilage associated with defects in procollagen II secretion, and absence of select, *neuroD*-positive neurons of the midbrain and hindbrain. The model presented here will help to systematically dissect developmental roles of Sar1b and to discover molecular and cellular mechanisms leading to organ-specific ANDD pathology.

Introduction

Role of SAR1B in chylomicron and lipid transport

Dietary lipids are absorbed primarily by enterocytes, where they are processed in the endoplasmic reticulum (ER) to triacylglycerols (TAG) (Abumrad and Davidson, 2012). Newly synthesized TAGs are packaged into prechylomicrons and exit ER to the Golgi complex for further processing (Iqbal and Hussain, 2009). ER-to-Golgi protein transport is mediated primarily by the COPII complex, consisting of five core proteins: Sar1

GTPase and Sec23-Sec24 of the inner coat, and Sec13-Sec31 of the outer coat (Miller and Barlowe, 2010). Subsequently, prechylomicron transport vesicles fuse to Golgi membranes (Siddiqi et al., 2003). Lipoprotein cargo is further transported to numerous target tissues, including liver, muscle, adipose tissue and brain (Walther and Farese, 2012). Although protein secretion has been extensively studied *in vitro*, lipoprotein cargo secretion mechanisms are largely unknown primarily because of lack of animal models to address these complex questions (Mansbach and Siddiqi, 2010).

Anderson Disease

Chylomicron Retention Disease, also known as Anderson Disease (CMRD/ANDD, OMIM 246700), is a rare autosomal recessive disorder characterized by failure to absorb dietary lipids and lipid soluble vitamins, shown to be caused by mutations in the *SAR1B* gene (Jones et al., 2003; Georges et al., 2011). Patients are mostly diagnosed early in life based on collective symptoms of steatorrhea, failure to thrive, and hypocholesterolemia with normal TAG, along with small intestine biopsy and histological analysis showing lipid droplets in the cytoplasm (Jones et al., 2003; Peretti et al., 2009). However, some patients are diagnosed later in life (Silvain et al., 2008) and go undetected until their children are diagnosed with ANDD. Recent case reports besides the gut and liver involvement have implicated the heart, skeletal muscle, bone, adipose tissue and pancreas, although the full spectrum of affected organs is unknown (Peretti et al., 2009; Silvain et al., 2008; Bernard et al., 2010). The combination of multiple organ involvement, age of onset/diagnosis and lack of phenotype-genotype relationship in patients complicates diagnosis and treatment of the disease, which can be effectively

managed by prompt implementation of low-fat diets and supplements of lipid-soluble vitamins (Peretti et al., 2009).

The pleiotropic nature of the syndrome and lack of published mutations affecting the *Sar1b* gene in vertebrate animal models prompted us to establish a zebrafish model using morpholino-based global knockdown strategies. Zebrafish has been previously used for studying lipid metabolism, benefiting from accessibility of the gastrointestinal organs to live imaging (Schlegel and Stainier, 2006; Anderson et al., 2011; Carten et al., 2011; Maddison and Chen, 2012; Walters et al., 2012).

The purpose of this study is to develop a vertebrate animal model system that could be used to (1) characterize the pathophysiology of Sar1b deficiency, (2) study the mechanisms of lipid malabsorption in Sar1 deficient animals, and (3) establish an *in vivo* model for future study of human SAR1B variants. We show that Sar1b deficiency leads to developmental deficits in multiple organs including gut, pancreas and liver of the gastrointestinal (GI) tract, but also skeletal dysmorphology due to failure of cartilage differentiation and maturation, and CNS nuclei specification. Our findings stress the possibility that ANDD patients' failure to thrive might not only stem from diarrhea and malnutrition but also multi-organ developmental deficits.

Materials and methods

Gene nomenclature

Gene names in the text are according to nomenclature guidelines, with human genes in capital italic (e.g. *SAR1B*) and zebrafish in lowercase italic (*sar1b*). Protein names are in roman font in the sentence case.

Zebrafish lines

AB strain zebrafish were raised and maintained under standard laboratory conditions at 28.5°C (Kimmel et al., 1995). For whole mount in situ hybridization experiments, embryos were raised in 0.2 mM 1-phenyl-2-thiourea (Sigma) to block pigmentation. The transgenic fish *Tg:[(fabp10a:dsRed;ela3A:GFP)gz15]* line was generated by the Gong laboratory (Korzh et al., 2008) and shared with us by the Leach laboratory. The transgenic fish *Tg:[(P0-pax6b:GFP)^{ulg515}]* (abbreviated *pax6b:GFP)* was generated by the Martial laboratory (Delporte et al., 2008) and shared with us by the Chen laboratory. For live imaging WT and sar1b-MO larvae were anesthetized in Tricaine (Sigma) and mounted in low-melt agarose. All confocal imaging in this manuscript was taken with a Zeiss LSM510 inverted confocal microscope (Vanderbilt Cell Imaging Shared Resource), while all other imaging was taken with a Zeiss AxioImager Z1.

All experiments were conducted in accordance with the guidelines established by the IACUC at Vanderbilt University.

Cloning and sequencing

Zebrafish *sar1b* cDNA (NCBI Reference Sequence: NM_001024377.1) was cloned using the primers 5'-GGCGGATCCTGAGAGCGGAGTTTGTCCAC-3' and 5'-GCCTCTAGATGTGTTTAGTCGATGTACTGA-3' (MWG Operon). The cDNA without the morpholino targeting site was subcloned from this plasmid for use with the rescue experiments. A 110 bp region of the *sar1b* 5'UTR and coding region was cloned using the primers 5'-CCCCTCGAGTTCTCCGGTGTTTCCTCATTG-3' and 5'-CCCCCGCGGACTATAAAT CCAATCAAATATG-3'. Zebrafish *sar1a* cDNA (NM_001017882) was cloned using the primers 5'-GCAGTGTTTCGCCTGCTTAC-3' AND 5'-GCTTACCTGTCACTAAACTGG-3'. Human *SAR1B* cDNA (NM_001033503) was cloned using the primers 5'-GGATATGTCCTTCATATTTGATTG-3' and 5'-TGTGTTAATCAATGTACTGTGC-3'.

Zebrafish *sar1b* and human *SAR1B* are located in syntenic regions of chromosome 21 and 5, respectively.

Cartilage proteoglycan staining

Alcian Blue staining was performed as previously described (Sarmah et al., 2010). 5 dpf larvae were fixed in 4% PFA, bleached in H_2O_2/KOH solution, stained overnight in 0.1% Alcian Blue in 70% EtOH/1% HCL, and then de-stained in acidic ethanol (70% ethanol, 5% HCl).

Whole mount in situ hybridization

Whole-mount in situ hybridization with probes recognizing *col2a1* and *sox9a* (Sachdev et al., 2001; Montero-Balaguer et al., 2006), *neuroD, dlx2*, *foxa3*, *trypsin*, *pax6b*, *nkx2.2*,

prox1, and *ceruloplasmin* (http://zfin.org/) (Bradford et al., 2010) were performed as previously described (Müller et al., 2006, 2013). The *sar1b* probe was made by cloning 862 nucleotides from the 3' UTR of the *sar1b* cDNA into the pGEM-T Easy Vector with the primers 5'-TTGACAAACCCGAGGCCATC-3' and 5'-CATTCCACCGCTGCTCCATG-3'.

Immunofluorescence and lectin staining

Type II collagen and wheat germ agglutinin (WGA) staining was performed as previously described (Sarmah et al., 2010) using 1:200 diluted primary antibody against collagen type II (Polysciences) and 1:200 WGA–Alexa-Fluor-555 conjugate (Molecular Probes), followed by 1:300 Alexa Fluor 488-conjugated secondary antibody (Molecular Probes) and TO-PRO-3 (Molecular Probes).

For acetylated tubulin staining, 5 dpf larvae were fixed overnight in Prefer Fixative (Anatech), rinsed, post-fixed for 10 minutes in 4% PFA, and then permeabilized in 0.5% triton X-100 for 10 minutes. Larvae were then bleached in H_2O_2/KOH solution for 20 minutes and then washed in blocking solution. 1:250 primary antibody against acetylated tubulin (Sigma) (Granero-Moltó et al., 2008) was applied overnight at 4°C followed by 1:300 Alexa Fluor 488-conjugated secondary antibody (Molecular Probes) for 3 hours at RT. After washing, larvae were post-fixed in 4% PFA for 20 minutes and then cleared in glycerol overnight. Images are presented as maximum intensity z-projections.

Morpholino Oligonucleotides

Antisense morpholino oligonucleotides (MOs) (Gene Tools, Corvallis, OR) were designed to target the *sar1b* 5'UTR sequence (sar1b-MO): 5'-CAGTCCAACGGGGATCAATGAGGAA-3'. The sar1b-MO targets bp 41-65 of the *sar1b* 5'UTR, which is 45 bp upstream of the ATG site. This target site is unique to *sar1b* and is not present in *sar1a*. 1 nl was injected into 1-2 cell stage embryos at increasing doses (0.4 ng-3 ng) to determine optimal concentrations. To confirm morpholino-targeting efficiency, 60 pg of sar1b-eGFP mRNA (see Fig. 1J, K) was co-injected with 0.4 ng and 1 ng of sar1b-MO, and loss of eGFP expression was analyzed. All data presented in figures are at 0.4 ng, determined to be the optimal concentration. Control morpholino provided by manufacturer did not generate morphological changes.

Dietary lipid clearance assay

The lipid clearance assay was modified from Schlegel and Stainier (Schlegel and Stainier, 2006). Live 5 dpf larvae were incubated with 10% chicken egg yolk (CEY) suspension in 0.3x Danieau buffer for 6 hours at 28.5°C and then rinsed in several washes in fresh egg water and then either processed immediately for lipid staining or fasted 16 hours and then processed. To ensure uniform micelle formation before feeding, CEY suspension was vortexed for 5 minutes, force pipetted, and then examined with a 100x objective before feeding. After feeding, larvae were processed using detergent-free conditions (Schlombs et al., 2003). They were fixed in 4% PFA, rinsed in PBS, bleached in H_2O_2/KOH solution, washed in 60% 2-propanol, and stained in 0.3% Oil Red O (Sigma) in 60% 2-propanol for 3 hours at room temperature, followed by washing in water. For analyzing lipids in enterocytes, larvae were fed as described above, fixed in

4% PFA, and then embedded in OCT. Cryosections were collected using a Leica CM-1900 cryotome and stained with Oil Red O. For TEM analysis of lipid droplets, larvae were processed as previously described (Melville et al., 2011) and imaged on a Phillips CM-12 Transmission Electron Microscope provided by the VUMC Cell Imaging Shared Resource.

Cholesterol absorption assay

NBD-cholesterol (Invitrogen) stock solution was added to EY suspension to a final concentration of 3 μg/mL and vortexed for 1 minute. Incorporation into EY micelles was confirmed using a 100x objective with fluorescence. Larvae were fed for 4 hours at 28.5°C, rinsed briefly in fresh Danieau buffer, anesthetized and then mounted in 1% low melting point agarose on glass bottom dishes with the intestinal bulb secured to the bottom of the dish. Confocal images of the anterior intestine near the swim bladder were collected.

Quantification of transgenic fish organ size

Live embryos were anesthetized and mounted in 1% low melting point agarose. Confocal z-stacks were collected and maximum intensity projections were used to calculate 2-D area using ImageJ.

Results

Sar1 genes and their expression during embryonic development

Vertebrate genomes contain two *Sar1* paralogs, *Sar1a* and *Sar1b*. We cloned the zebrafish *sar1a* and *sar1b* genes and found that both are highly evolutionarily conserved. Zebrafish *sar1b* shares 91% identity and 98% similarity with the human gene and is located in a syntenic region on chromosome 21. The 11.6 kb locus contains 8 exons that code for a predicted 198 amino acid peptide (Fig. 3.1).

Sar1b is selectively expressed throughout development (Fig. 3.2). Initially, transcripts are maternally deposited into the egg (Fig. 3.2A) and zygotically expressed throughout gastrulation in all germ layers (Fig. 3.2B). During organogenesis, highest expression levels are found in the central nervous system and eye (Fig. 3.2C). At 3 days of development the transcripts are highly enriched in the craniofacial skeleton and the alimentary tract (Fig. 3.2E,F), a trend that continues throughout day 4 (Fig. 3.2G-I). On the contrary its close paralog, *sar1a*, is expressed ubiquitously throughout development (Fig. 3.3A-H). Thus, it appears that *sar1* genes are expressed in overlapping domains, with *sar1b* being enriched in the CNS, craniofacial cartilage, gut and other organs of the digestive system.

In order to develop an in vivo model system to characterize the pathophysiology of the Sar1b deficiency, we designed a morpholino-labeled antisense oligonucleotide targeting the 5'UTR of the *sar1b* transcript (Fig. 3.4A). The morpholino (MO) blocked translation

of a Sar1b reporter construct (Fig. 3.4B), and we have used in all of the experiments presented here the lowest effective dose (0.4 ng).

To test specificity of the MO, we conducted rescue experiments in a double-blinded fashion by co-injecting synthetic RNA. We injected either buffer alone as a control, sar1b-MO alone, or co-injected sar1b-MO along with zebrafish *sar1b* mRNA lacking the MO target sequence (Fig. 3.4C), human *SAR1B* mRNA, or zebrafish *sar1a* mRNA. Injected embryos were analyzed at 4 dpf and grouped into normal, moderate, or severe phenotypic categories, according to body length, head size, and pectoral fin morphology (Fig. 3.4D), and the identity of the treatment groups was revealed after phenotypic categorization. Sar1b morphant embryos presented shortened body length, a malformed jaw, and kinked pectoral fins (7% normal, 54% moderate (as shown in Fig. 3.4E), 39% severe). These morphant phenotypes were efficiently rescued by co-injection of synthetic zebrafish *sar1b* mRNA (87% normal, 13% moderate) or human *SAR1B* mRNA (83% normal, 14% moderate, 3% severe) (Fig. 3.4D). Zebrafish *sar1a* mRNA co-injection partially rescued the morphant phenotypes (57% normal, 31 % moderate, 12% severe) but less effectively than *sar1b*. To quantitatively assess rescue efficiency, we measured body length (Fig. 3.4E), which showed a similar trend as observed with phenotypic categorization.

Sar1b-deficient zebrafish fail to absorb dietary lipids

The hallmark of ANDD is failure of dietary lipid absorption due to impaired secretion from enterocytes. To test the efficiency of lipid absorption in Sar1b morphants, we used a

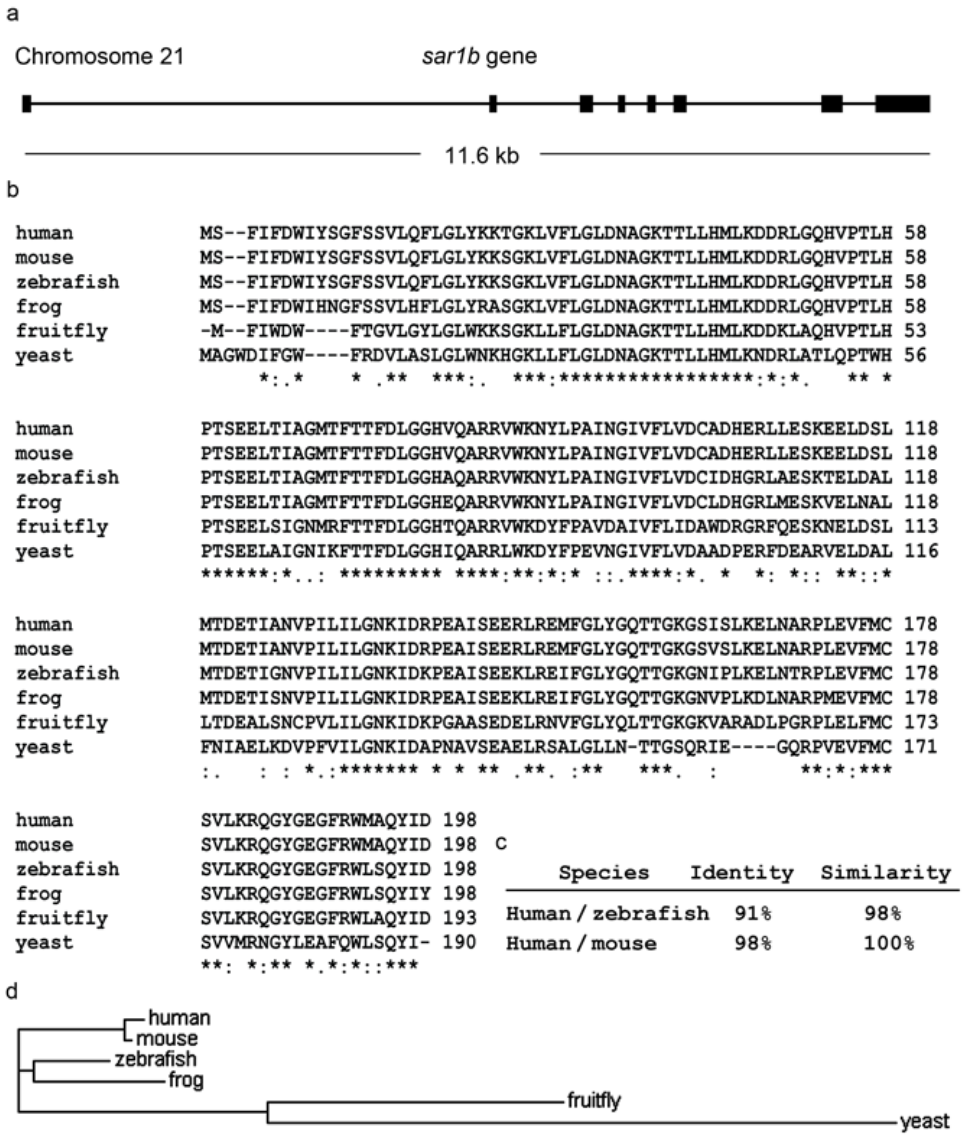

Figure 3.1. Sar1b is highly conserved during evolution.
(A) Schematic representation of the zebrafish *sar1b* gene on chromosome 21. (B) Amino acid sequence alignment from human, mouse, zebrafish, frog, fruit fly and yeast. Sequences were obtained from RefSeq: human (*Homo Sapiens*: NP_001028675.1), mouse (*Mus musculus*: NP_079811.1), zebrafish (*Danio rerio*: NP_001019548.1), frog (*Xenopus laevis*: NP_001080924.1), fruit fly (*Drosophila melanogaster*: NP_732717.1), yeast (*Saccharomyces cerevisiae*: NP_015106.1); (*) identical; (.) conserved; (:) highly conserved substitutions among sar1b orthologs. The zebrafish Sar1b gene is an ortholog of the human gene as confirmed by syntenic blocks on respective chromosomes, and the zebrafish genome does not contain a duplicated Sar1b gene. (C) Pairwise comparison of amino acid conservation between human, mouse, and zebrafish *sar1b*. (D) Phylogenetic tree of Sar1b primary sequence from the species listed in B.

dietary lipid clearance assay (Schlegel and Stainier, 2006). First, we fed 5-day old larvae with a high fat meal (chicken egg yolk suspension) and assayed lipid content in enterocytes with Oil Red O (ORO). We found that WT and Sar1b-morphant enterocytes formed abundant lipid droplets in response to feeding (Fig. 3.5A,B). We then tested the efficiency of clearing ingested lipids from the intestinal bulb using a pulse-chase approach (Fig. 3.5C). We fed larvae for 6 hours, removed the feeding solution, and fasted the animals for 16 hours before processing them for ORO staining. To exclude any effects of feeding behavior differences, we excluded larvae that did not participate in feeding, which can be visually confirmed because of the transparency of the zebrafish gut (Walters et al., 2012). We found that 80% of WT larvae cleared lipids from the intestinal bulb after fasting. After Sar1b depletion, however, only 21% of larvae cleared ingested lipids. Dietary lipid retention in Sar1b morphants could be efficiently rescued with *sar1b* expression ($p < 0.001$, Fisher's exact test) but not *sar1a* expression ($p = 0.17$). Transmission electron microscopy analysis showed that both WT and sar1b morphant enterocytes formed lipid droplets in response to feeding, but Sar1b morphants failed to clear lipid droplets after fasting (Fig. 3.6A-C). These findings confirmed that Sar1b morphants are able to ingest and uptake dietary lipids into enterocytes but have diminished capability to secrete lipid droplets, a phenotype resembling that of ANDD patients (Peretti et al., 2009).

Another characteristic of ANDD is hypocholesterolemia, which may result directly from cholesterol malabsorption in enterocytes or secondarily from impaired liver function. To test whether Sar1b is required for dietary cholesterol absorption, we fed larvae with

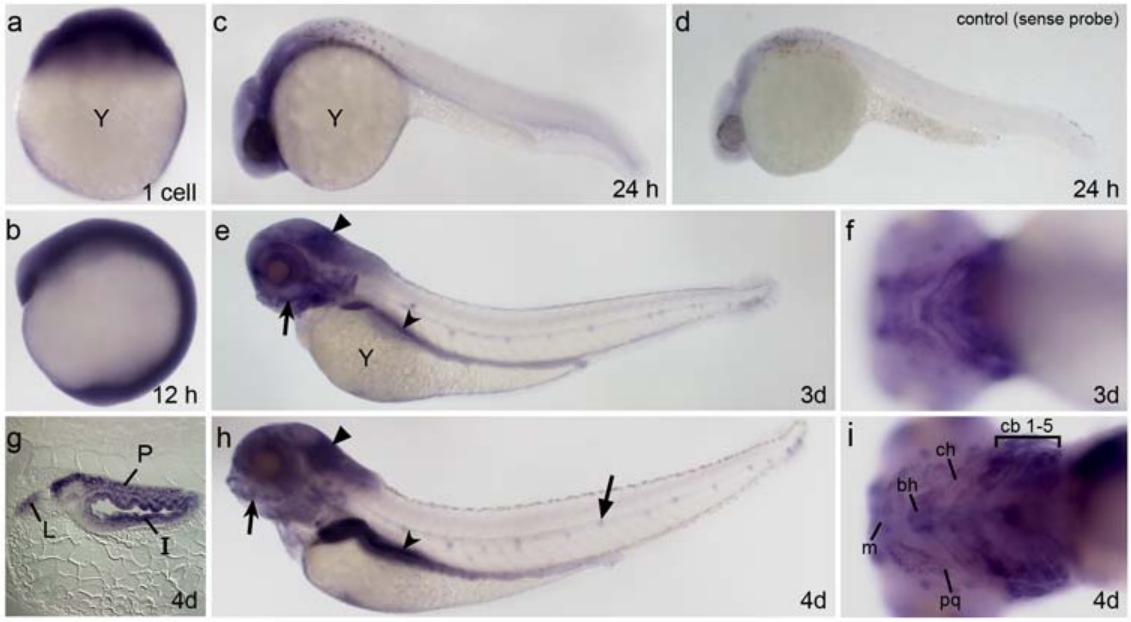

Figure 3.2. Sar1b is expressed in select neural tissues, pharyngeal arches and gut. *Sar1b* mRNA expression by whole mount in situ hybridization at 1cell stage (A), 12 hpf (B), 24 hpf (C), 3 dpf (E, F) and 4 dpf (G-I). Embryos are oriented with head towards the left in lateral views (C,D,E,H), ventral views (F,I) and sagittal section of the mid-gut region at 4 dpf (G). At 24 hpf, expression is concentrated within the ventral brain region (C) and not detected by the sense probe (D). Pigment cells appear as dark spots in C and D. By 3 dpf, transcripts are present throughout the brain, eye, lateral line organ (flat arrow) and enriched in pharyngeal arches (concave arrow) gut (concave arrowhead), and cerebellar plate (flat arrowhead) (E). By 4 dpf the expression persists in the same locations (H), including intestinal epithelium, pancreas, and liver (G), as well as the pharyngeal arches.

NBD-cholesterol, a fluorescent cholesterol analog, in chicken egg yolk suspension (NBD-Ch+EY) for 4 hours and then imaged live enterocytes using confocal microscopy. We found that 91% of WT larvae fed with NBD-Ch+CEY exhibited fluorescent puncta within enterocytes (Fig. 3.6D,E). In contrast, only 28% of Sar1b morphants had up-taken NBD-cholesterol into enterocytes (Fisher's exact test, $p<0.001$). Both WT and Sar1b morphants ingest NBD-cholesterol normally, as indicated by high levels of fluorescence in the intestinal lumen. These findings provide for the first time direct evidence that Sar1b might be required for cholesterol uptake into enterocytes and suggests that hypocholesterolemia in ANDD patients may not be an exclusive result of defects in lipid metabolism. Collectively, our findings show that Sar1b depletion in zebrafish closely resembles ANDD deficits. Conservation of this major ANDD phenotype in zebrafish could establish a practical animal model to study lipid malabsorption and test effective therapeutic strategies.

Sar1b is essential for digestive tract development

Sar1b is highly expressed in the zebrafish gut, pancreas and liver. Patients with ANDD exhibit exocrine pancreas deficiency and sporadic hepatomegaly (Georges et al., 2011; Charcosset et al., 2008). This phenotype was ascribed to chronic diarrhea and altered lipid metabolism postnatally, not to developmental defects. To test whether digestive organs develop normally in Sar1b depleted embryos, we examined expression of patterning and differentiation markers of liver and pancreas (Shin et al., 2007). Using whole mount in situ hybridization with *foxa3* (a transcription factor directing GI tract patterning), we found that the gut primordium, including liver and pancreas buds, are

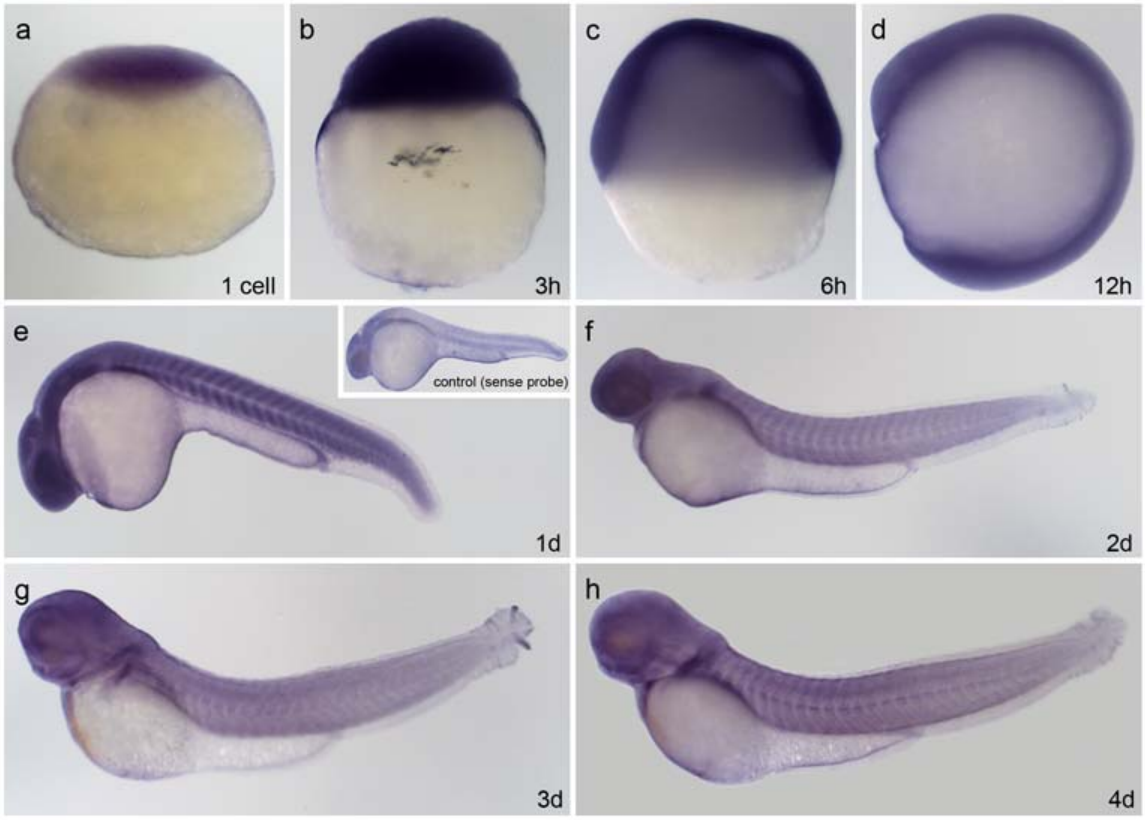

Figure 3.3 Sar1a is ubiquitously expressed throughout development.
Sar1a mRNA expression at 1 cell stage (A), 3 hpf (B), 6 hpf (C), 12 hpf (D), 1 dpf (E), 2 dpf (F), 3 dpf (G) and 4 dpf (H). Embryos are oriented with head towards the left in lateral views. *Sar1a* transcripts are detected at the one cell stage (A) before the onset of zygotic transcription at 3 hpf, indicating maternal deposition. Sar1a is expressed ubiquitously during gastrulation (B-D). The expression is essentially evenly distributed throughout tissues during segmentation and organogenesis stages. The segmented expression in the trunk is not detected by the sense probe (E, inset).

largely unaffected (Fig. 3.7A) at 2 dpf. Similarly, pancreas patterning markers nkx2.2 and pax6b (Fig. 3.7B-C) were largely unaffected at 2 dpf, and at 3 dpf in live *pax6b:eGFP* transgenic fish (Fig. 3.7D-E). Liver patterning was also not affected in Sar1b morphants, using *prox1* and *ceruloplasmin* in situ probes at 2 dpf (Fig. 3.7F-G). However, at 5 dpf the exocrine pancreas, as marked by *trypsin* probe (Fig. 3.7H) and in live LiPan transgenic line (Fig. 3I-J), failed to grow and expand caudally (Korzh et al., 2008), and liver growth was also significantly reduced (Fig. 3.7I-K), which could be partially rescued with injection of synthetic *sar1b* mRNA (Fig. 3.7I-K). The intestinal bulb and adjacent anterior intestine was correctly patterned, but slightly distended as marked by *ifabp* gene expression, and hematoxylin and eosin staining of enterocytes revealed normal columnar epithelia and brush border morphology (our unpublished observations). These data indicate that Sar1b is not essential for patterning of the digestive organs, but is required for their growth.

Sar1b-depletion affects brain patterning

ANDD patients were reported to present with cerebellar ataxia and sensory neuropathy symptoms, which were attributed to Vitamin E deficiency due to dietary malabsorption (Bernard et al., 2010). To test whether the neuronal deficits are secondary to dietary depravation, or alternatively, are the primary developmental defect occurring before the fish begin food intake, we conducted a whole mount mRNA in situ hybridization to assess expression of *neuroD*, a bHLH transcription factor specifying progenitor populations of neuronal precursors in retina, epibranchial ganglia, cerebellum, hindbrain rhombomeres, thalamus and optic tectum (Fig. 3.8). We found normal *neuroD* expression

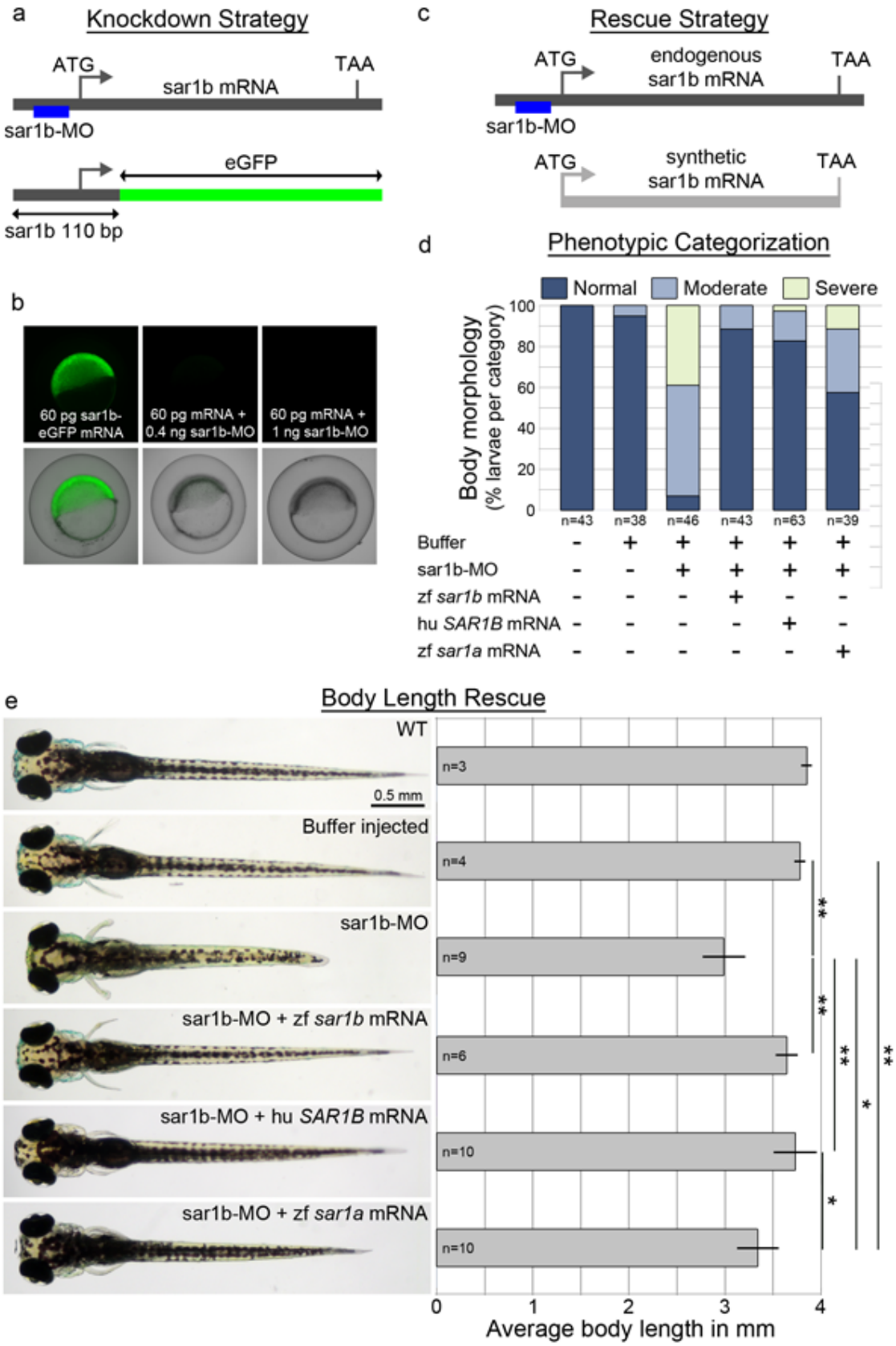
a
Knockdown Strategy
ATG
TAA
sar1b mRNA
sar1b-MO
eGFP
sar1b 110 bp
b
60 pg sar1b-eGFP mRNA
60 pg mRNA + 0.4 ng sar1b-MO
60 pg mRNA + 1 ng sar1b-MO
c
Rescue Strategy
ATG
endogenous sar1b mRNA
TAA
sar1b-MO
ATG
synthetic sar1b mRNA
TAA
d
Phenotypic Categorization
Normal
Moderate
Severe
Body morphology (% larvae per category)
100
80
60
40
20
0
n=43
n=38
n=46
n=43
n=63
n=39
Buffer - + + + + +
sar1b-MO - - + + + +
zf sar1b mRNA - - - + - -
hu SAR1B mRNA - - - - + -
zf sar1a mRNA - - - - - +
e
Body Length Rescue
WT
0.5 mm
Buffer injected
sar1b-MO
sar1b-MO + zf sar1b mRNA
sar1b-MO + hu SAR1B mRNA
sar1b-MO + zf sar1a mRNA
n=3
n=4
n=9
n=6
n=10
n=10
**
**
**
**
*
*
0
1
2
3
4
Average body length in mm

Figure 3.4. Efficient inhibition and rescue of Sar1b function with synthetic morpholino oligonucleotide and mRNA injection.
Targeting efficiency of sar1b-MO (A-B). (A) Schematic representation of the knockdown strategy showing *sar1b* mRNA and position of the translation blocking morpholino (sar1b-MO). The sar1b 5'UTR-eGFP fusion protein mRNA construct contains the sar1b-MO binding site. (B) Double injected embryos with fusion construct and increasing doses of sar1b-MO show almost complete knockdown of GFP expression at 0.4 ng (middle panel) and complete absence of GFP expression at 1 ng of sar1b-MO (right panel). Targeting specificity of sar1b-MO (C-E). (C) Schematic representation of the rescue strategy showing *sar1b* mRNA and synthetic *sar1b* mRNA, which lacks the sar1b-MO binding site and which is used for rescue experiments. (D) Double-blinded phenotypic categorization of overall morphology at 4 dpf according to body length, head size, and pectoral fin shape. 54.3% of sar1b-MO injected embryos exhibit a moderate phenotype (representative example in panel N), while 88.4% of embryos co-injected with sar1b-MO and *sar1b* mRNA are morphologically normal at 4 dpf. Human (hu) *SAR1B* mRNA rescues morphogenesis similarly to zebrafish (zf) *sar1b*, while zf *sar1a* mRNA partially compensates for *sar1b* knockdown. (E) Images of live embryos with body length quantification for rescue experiments. Sar1b morphants exhibit reduced body length while sar1b-MO + zf *sar1b* mRNA or hu *SAR1B* mRNA co-injected embryos do not have significant reduction of body length at 4 dpf. zf *sar1a* partially rescues body length in sar1b-MO injected embryos. Error bars are ± SD. Abbreviations: y, yolk, m, Meckel's cartilage, bh, basihyal, pq, palatoquadrate, ch, ceratohyal, cb, ceratobranchials 1-5, I, intestine, L, liver, P, pancreas; zf, zebrafish; hu, human. * $p < 0.05$, ** $p < 0.01$; One-way ANOVA standard weighted means analysis with Tukey's test.

in epibranchial ganglia, but expression was significantly reduced in retina, cerebellum, hindbrain rhombomeres, thalamus, and optic tectum (Fig. 3.8A-B).

These findings suggest that Sar1b function is required in select neural stem cells of the brain. Because neuronal deficits appear before the larvae become dependent on dietary lipid absorption, we conclude that the observed phenotypes are most likely due to primary developmental defects. Moreover, the position of neurons in epibranchial ganglia matched the corresponding developmental stage, indicating that the deficits do not represent developmental delays in morphants. Acetylated tubulin staining revealed the presence of all major axonal tracks, although the positioning and density of the axonal projections in the optic tectum and rhombic lip appear to be underdeveloped (Fig. 3.8C). These findings reveal potential for broad developmental deficits in the CNS, but their functional implications need to be further investigated in patients and animal models.

Sar1b knockdown disrupts skeletal morphogenesis

Depletion of Sar1b resulted in shorten body length, kinked pectoral fins and a compact head, particularly along the rostro-caudal axis (Fig. 3.9A,B). The craniofacial skeleton was significantly smaller and malformed as evident in Alcian blue stained preparations at 5 days of development (Fig. 3.9C,D). To determine at what developmental stage the first craniofacial deficits can be detected, we used whole mount mRNA in situ hybridization with probes for transcription factors *dlx2* and *sox9a* (Barrallo-Gimeno et al., 2004) marking craniofacial primordia at 2 dpf and 3 dpf, respectively (Fig. 3.9E,F). Although we did not observe any deficits at 2 dpf, the time of neural crest migration, at 3 dpf the

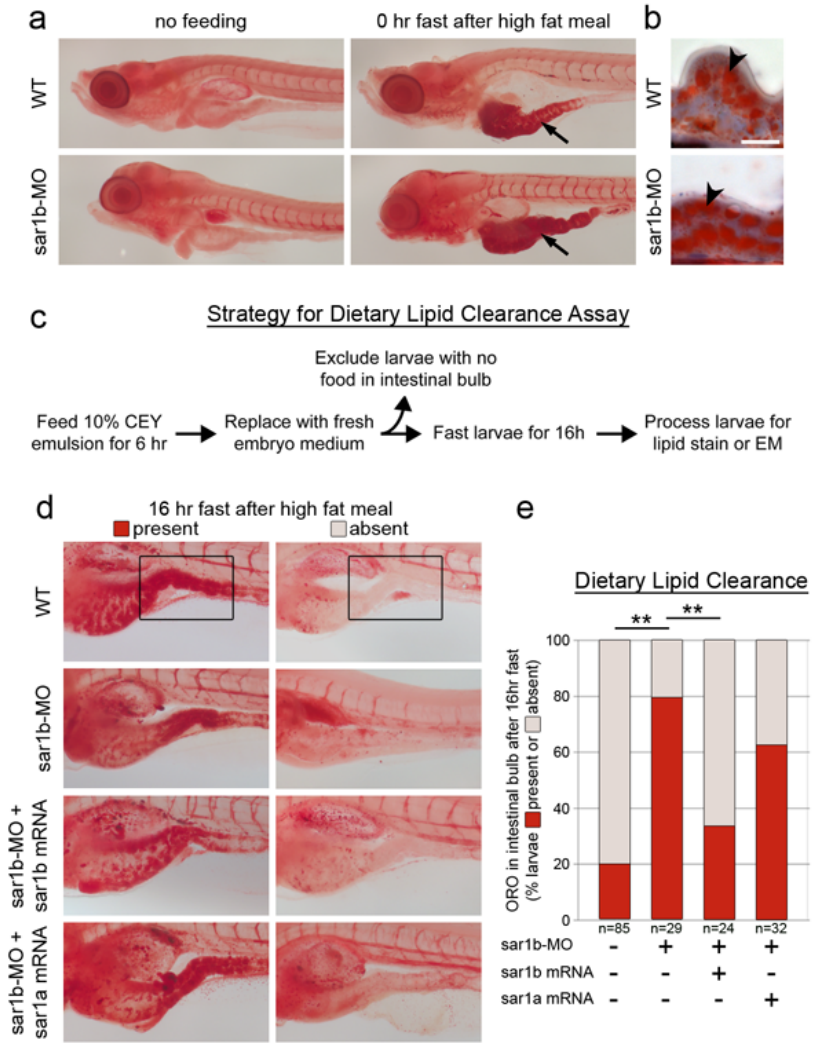

Figure 3.5. Sar1b knockdown impairs dietary lipid absorption.
(A) Whole-mount detergent-free Oil Red O (ORO) staining of WT and sar1b morphant embryos under non-fed fasting conditions (left) and immediately after feeding a high fat meal (10% chicken egg yolk). After feeding, the intestinal bulb contains abundant lipids (arrow). (B) ORO staining of gut cryosections after feeding shows that lipids accumulate within enterocytes (concave arrowhead). (C) Schematic of experimental design and workflow for testing dietary lipid clearance in zebrafish larvae. Sar1b knockdown impairs dietary lipid clearance from enterocytes (D-H). (D) ORO staining of WT, sar1b-MO, and sar1b-MO + mRNA co-injected larvae fasted 16 hours after feeding. Left panels show representative examples of larvae with lipids remaining in the gut after fasting (present), while right panels show larvae that have cleared lipids from the intestinal bulb (absent). (E) Quantification of ORO presence in intestinal bulb after lipid clearance assay. *Sar1b* knockdown significantly impairs dietary lipid clearance, which can be rescued with *sar1b* mRNA expression. *Sar1a* mRNA does not effectively compensate for *sar1b* knockdown. Scale bar is 10 µm. ** $p<0.01$, Fisher's exact test. Error bars are ± SD.

craniofacial cartilage primordia of *sar1b* morphants were already smaller than in controls.

Our prior works on Sec23a and Sec24D genes, two components of the COPII inner coat, revealed similar deficits in *sox9a* expression in zebrafish mutants (Sarmah et al., 2010; Lang et al., 2006). To test whether the phenotype stems from deficits in cartilage ECM secretion, we analyzed the expression of chondrogenic differentiation markers, including *col2a1*, the primary component of cartilage ECM, and *hsp47,* the collagen II specific chaperon required for its secretion from the ER. We noted smaller and misshapen cartilage elements expressing comparable levels of *col2a1* transcripts (Fig. 3.9G). However, expression of *hsp47* was highly upregulated in cartilage elements, consistent with patterns observed in other COPII mutants (our unpublished observations). The deficits in cartilage differentiation were likely a consequence of collagen II backlog in the ER as confirmed by immunofluorescence antibody labeling and the staining for N-glycosylated proteins by wheat germ agglutinin (WGA) of craniofacial chondrocytes, which revealed deficits in ECM matrix deposition and intracellular accumulation of collagen (Fig. 3.9H).

Discussion

Sar1b Gene and Genetics of Anderson Disease

Here we present the first vertebrate animal model for Anderson Disease (ANDD), a rare genetic disease associated with mutations in the *SAR1B* gene. The zebrafish genome, like the human genome, contains two *sar1* paralogs, *sar1a* and *sar1b*. The two paralogs differ

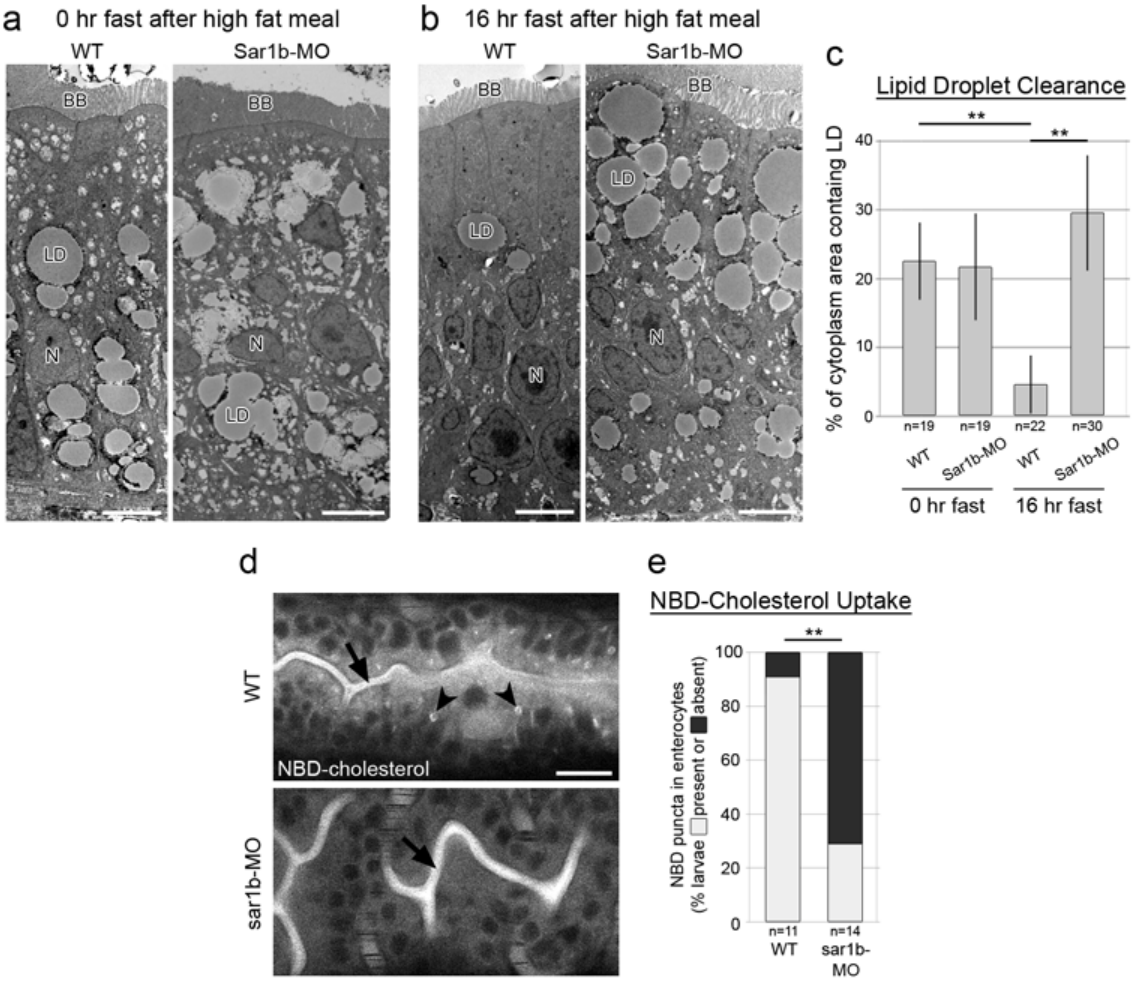

Figure 3.6. Sar1b is required for lipid droplet clearance and dietary cholesterol uptake.

(A) Transmission electron microscopy (TEM) analysis of WT and sar1b morphant larvae immediately after feeding 10% CEY. Lipid droplets (LD) are present in the enterocyte cytoplasm after a high fat meal (Zhu et al., 2009). Scale bars represent 5 µm. (B) TEM of WT and sar1b morphant larvae after lipid clearance assay. WT enterocytes contain few LDs compared to sar1b morphants (Roy et al., 1987; Dannoura et al., 1999). Scale bars represent 5 µm. (C) Quantification of lipid droplet abundance in enterocyte cytoplasm from TEMs. (D) NBD-cholesterol is present in the intestinal lumen of WT and morphants (arrows) when fed a high fat meal spiked with the cholesterol-fluorophore conjugate, but cholesterol positive inclusions are present only in the WT enterocytes (arrowheads) and absent in 71.4% of Sar1b morphants. Scale bars represent 20 µm. (E) Quantification of NBD fluorescence in enterocytes after feeding. ** $p<0.01$, Fisher's exact test (E) or two way ANOVA with Tukey's test (C). Error bars are ± SD. Abbreviations: BB, brush border; LD, lipid droplet; N, nucleus.

by only 20 residues in the 198 amino acid peptides in humans (Charcosset et al., 2008) and by 25 residues in zebrafish. Interestingly, none of the divergent residues were found to be mutated in described patients (Georges et al., 2011), suggesting that the specialized function of Sar1b may not depend on the divergent sequence differences. The zebrafish and human Sar1b are 91% identical and 98% similar (Fig. 3.1), prompting us to use zebrafish Sar1b depletion to model the pathophysiology of ANDD. Using a gene knockdown strategy, we show that Sar1b loss-of-function presents with phenotypes similar to ANDD, and leads to reduction of dietary lipid absorption as well as other developmental defects that are consistent with ANDD symptoms.

To date no mutations in *SAR1A* have been associated with ANDD or any other human syndrome, and it is unknown what phenotypes could be associated with SAR1A variants. We found that although *sar1a* is ubiquitously expressed in zebrafish embryos (Fig. 3.3A-H), its knockdown does not lead to gross morphological deficits (our unpublished observations). However, the combined depletion of Sar1a and Sar1b results in phenotypes similar to Sar1b knockdown, but with more severe phenotypes (our unpublished observations). Furthermore, overexpression of Sar1a is able to partially rescue Sar1b deficiency, suggesting that the two genes play largely similar roles in secretion with possible Sar1a partial compensation for Sar1b. This hypothesis may explain the broadly variable phenotype in spectrum and severity and is further supported by compensatory increase of *SAR1A* expression in enterocytes of ANDD patients (Georges et al., 2011). Additionally, Sar1 paralog- and cargo-specific transport could explain the rather modest and tissue-specific manifestations of the disease. Potential

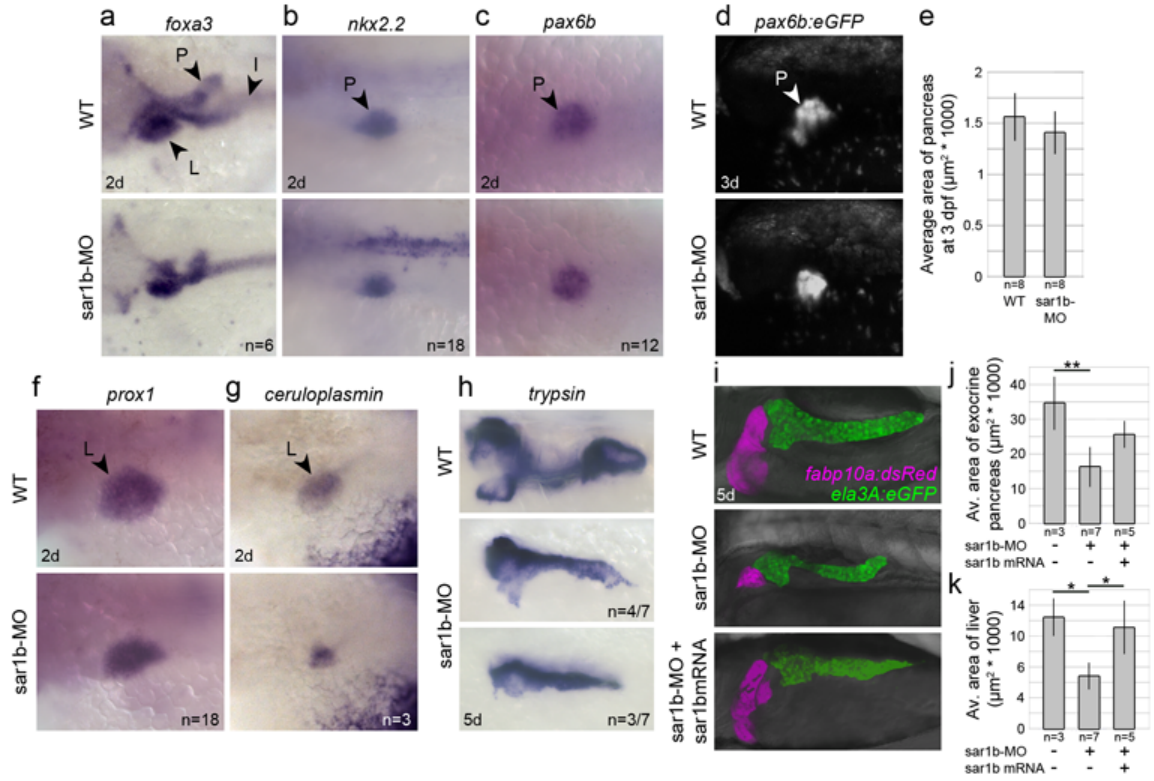

Figure 3.7. Sar1b knockdown results in reduced size of digestive organs.
(A-C) Transcripts of *foxa3*, *nkx2.2,* and *pax6b* detected by whole-mount in situ hybridization show no significant differences in spatiotemporal patterning and specification of pancreatic precursors at 2 dpf. (D-E) Expression of the (*pax6b:GFP*) transgene shows modest but insignificant reduction in pancreas size at 3 dpf. (F-G) Transcripts of *prox1* and *ceruloplasmin* show no significant differences in spatiotemporal patterning and specification of liver precursors at 2 dpf. (H) Transcripts of *trypsin* show reductions in pancreas size and change in lobular shape at 5 dpf. (I-K) Expression of the liver (*fabp10a:dsRed)* and pancreas (*ela3A:eGFP)* transgenes show consistently reduced size in 5 dpf Sar1b morphants, which can be partially rescued with *sar1b* mRNA expression. Error bars are ± SD. Abbreviations: L, liver, P, pancreas, I, intestinal bulb. * $p < 0.05$, ** $p < 0.01$; two-tailed unpaired t-test (E) or One-way ANOVA standard weighted means analysis with Tukey's test (J-K).

transcriptional control responsible for fine-tuning of *SAR1* gene expression has not been investigated and could explain unique and redundant functions of *SAR1* genes in lipid absorption and more broadly in COPII-dependent transport of other cargos (Melville et al., 2011). Further investigation of paralog-specific functions will be needed to address these interesting questions (Unlu et al., 2014).

Sar1b Function in Lipid and Cholesterol Absorption

ANDD diagnosis is made based on collective clinical symptoms of lipid malabsorption, hypocholesterolemia with normal serum triglycerides, and histology of small intestine biopsy samples showing accumulation of lipid droplets in enterocytes (Peretti et al., 2009). Although hypocholesterolemia is a hallmark of ANDD, its mechanism is unknown (Charcosset et al., 2008), and despite major research interest in cholesterol homeostasis and its role as a risk factor in cardiovascular diseases, numerous questions remain unanswered. For example, the mechanism by which cholesterol in intestinal micelles crosses the brush-border barrier is being investigated (Iqbal and Hussain, 2009), and the role of Sar1b in cholesterol transit to the basolateral membrane of the enterocyte is also actively pursued (Siddiqi et al., 2003).

In our model we fed a high-fat diet to Sar1b-deficient zebrafish larvae and observed that the enterocytes contained abundant lipid droplets (Fig. 3.6A), consistent with symptoms observed in ANDD patients. This shows that Sar1b morphant enterocytes are able to uptake lipids. When we spiked the dietary lipids with a fluorescent cholesterol analog, however, a significantly higher percentage of Sar1b-deficient larvae were negative for

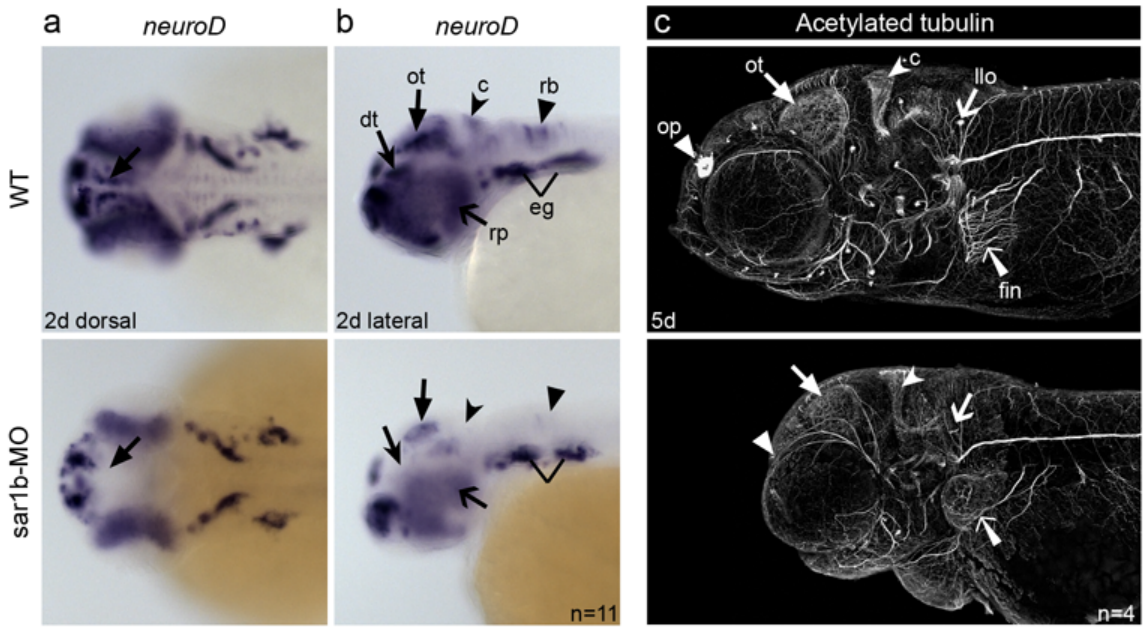

Figure 3.8. Depletion of Sar1b disrupts neural development.
(A, B) Whole mount in situ hybridization with riboprobe detecting *neuroD* transcripts in 2 dpf embryos shows relatively normal spatio-temporal expression in epibranchial ganglia (eg), but reduced or absent expression demarcating neuroprogenitors in the dorsal thalamus (dt), optic tectum (ot), cerebellum (c) and hindbrain rhombomeres (rb), as well as retinal progenitors (rp). Dorsal (A) and (B) lateral views. (C) Maximum intensity z-projections of acetylated tubulin stained axonal tracks reveals reduction in staining in the olfactory pits (op), lateral line (llo) sensory patches of the head and pectoral fin innervation (fin). The forebrain and the optic tectum (ot) are reduced in size and shifted anteriorly in the morphants.

intracellular cholesterol analog compared to wild-type siblings (Fig. 3.3D,E), suggesting that Sar1b might play a role in cholesterol absorption. Because ANDD is considered a lipid absorption disease, one might intuitively conclude that hypocholesterolemia is caused by a similar mechanism as lipid malabsorption in ANDD patients. If this was true, then one would expect cholesterol to be backlogged in chylomicrons in Sar1b-deficient enterocytes. Our findings, however, indicate that Sar1b is needed for cholesterol uptake into enterocytes, suggesting unexpected and complex function in cholesterol homeostasis. Studies of COPII-dependent transport of proteins that are required for cholesterol uptake, such as cholesterol esterase secretion from the pancreas and NPCL1 translocation to the enterocyte brush border (Iqbal and Hussain, 2009), may further clarify the mechanisms of cholesterol malabsorption in ANDD patients. Dietary cholesterol uptake represents less than a third of daily cholesterol supply, with the majority coming from endogenous production by the liver and peripheral tissues. Thus, malabsorption alone may not explain the severe and consistent hypocholesterolemia observed in ANDD patients. Further functional studies will be required to elucidate the mechanisms of Sar1b-dependent hypocholesterolemia.

Pancreas Function in ANDD

Besides lipid malabsorption, ANDD patients often present with exocrine pancreatic insufficiency (EPI) and require exocrine pancreatic enzymes supplemented to their diet to attain normal growth (Georges et al., 2011; Peretti et al., 2009). Prevailing interpretations of EPI conclude that chronic diarrhea and ensuing lipid malabsorption is responsible for reduced pancreatic function (Georges et al., 2011). In addition to this possibility, EPI

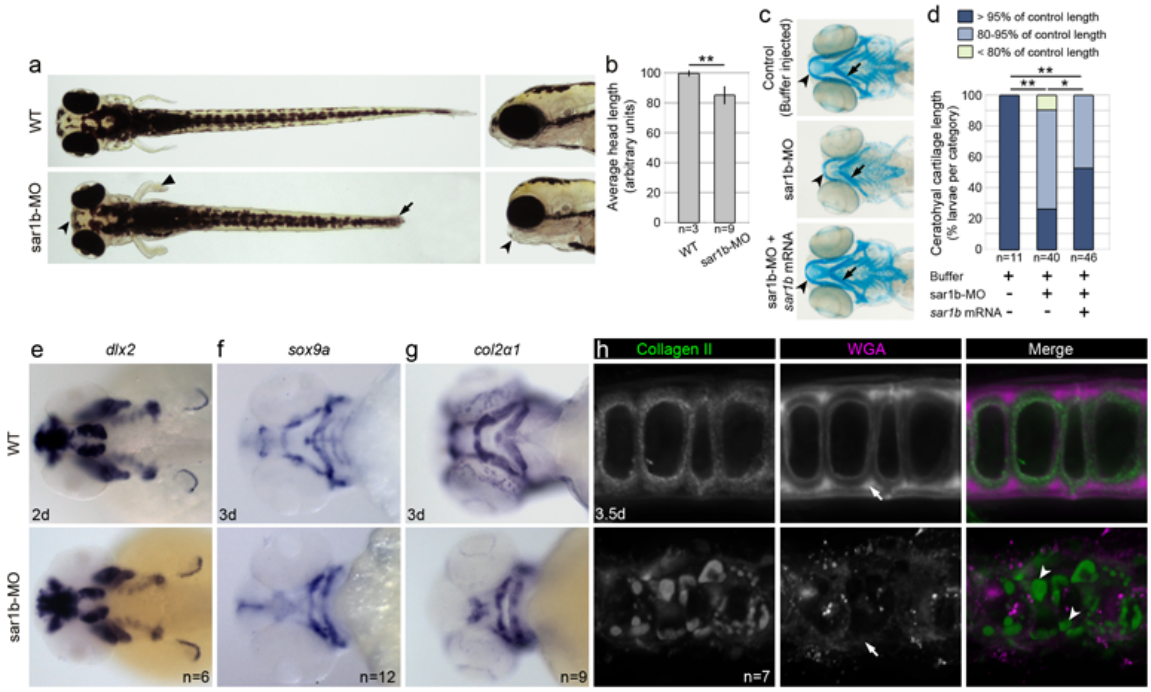

Figure 3.9. Sar1b knockdown results in skeletal dysmorphology.
(A) Live images of WT and *sar1b* morphants show shorter head in anteroposterior direction (concave arrowhead), kinked pectoral fins (flat arrowhead) and a shorter overall body length (arrow) in dorsal and lateral head views. (B) Quantification of anteroposterior head length measurements at 4 dpf. (C) Alcian blue stained head skeleton preparations revealed a shortened Meckel's (concave arrowhead) and malformed ceratohyal (Ch) cartilage elements (arrow) of Sar1b-MO compared to control embryos, while sar1b-MO + sar1b mRNA co-injection rescued cartilage morphology. (D) Quantification of Ch cartilage length of Alcian blue stained embryos. Control length refers to the average length of buffer-injected embryos. (E) Unchanged *dlx2* expression in Sar1b-MO shows that neural crest cell migration and patterning are normal in *sar1b* morphant embryos at 2 dpf. (F) Chondrogenic differentiation marker *sox9a,* (G) and its target gene *col2a1* show reduced size and malformed morphant cartilages compared to WT. (H) Immunofluorescence staining with antibody recognizing Collagen II and of N-glycans using wheat germ agglutinin (WGA) shows intracellular inclusions of procollagen type II (arrowheads) and reduced staining intensity of N-glycans within extracellular matrix (arrows). Error bars are ± SD. * $p < 0.05$, ** $p < 0.01$; two-tailed unpaired t-test (B) or Fisher's exact test (D).

could stem from reduced secretory capacity of the exocrine pancreas (COPII-dependent protein secretion), along with developmental deficits that lead to reduced pancreatic mass. This possibility is supported by our data. In Sar1b-depleted animals, we observed significant reduction in pancreas size and lobular structure ranging from very severe to mild (representative phenotypes shown in Fig. 3.7H,I) that could explain the variable penetrance of this phenotype in patients. Our finding that variable reductions in pancreas size occur during development and before feeding may suggest that steatorrhea is not a primary mechanism of EPI in ANDD patients.

Sar1b in Skeletal Morphogenesis

Prior Northern Blot analysis of adult human tissue RNA samples has shown *SAR1B* expression in the small intestine, liver, skeleton and heart muscle (Jones et al., 2003). Here, we have expanded the spectrum of the *sar1b* expression and deficiency phenotypes to include skeletal cartilage. Although French patients had decreased bone mineral density, this was attributed to poor nutritional regime due to malabsorption and not to an intrinsic role of SAR1B in bone homeostasis (Peretti et al., 2009). We show that lack of Sar1b leads to deficiencies in chondrocyte capacity to produce and maintain type II collagen, a predominant matrix component of cartilage (Fig. 3.9). Thus it is possible that osteopenia and osteoporosis observed in some patients might be a consequence of COPII-deficiency that impairs ECM secretion in skeletal tissues (Melville and Knapik, 2011).

Conclusions

Remarkably little is known about COPII-dependent lipid transport and the molecular mechanisms controlling these processes. Although biochemical studies have helped to clarify the mechanisms of Sar1b-dependent chylomicron transport, lack of genotype-phenotype correlation in ANDD complicates understanding of Sar1b function in vivo. The ANDD model presented here will help to address numerous outstanding questions related to pathophysiology of Sar1b-deficiency. Additionally, this model provides entry points to discover mechanisms of other complex traits. Obesity and other metabolic diseases such as atherosclerosis present formidable challenges to functionally dissect underlying molecular mechanisms because of small contributions of common and rare genetic variants, which do not grant sufficient quantitative power to explain the disease phenotype. Zebrafish models offer a unique experimentally amenable system to advance understanding of rare genetic diseases and metabolic disorders (Vacaru et al., 2014). Zebrafish genetic models can be used to perform chemical biology screens to discover novel compounds that may be used not just to treat ANDD but other disorders of cholesterol synthesis and homeostasis. The study presented in this manuscript sets the stage for future investigations and development of new high-throughput tools to address this problem, and importantly, a better understanding of the pathophysiology of SAR1B deficiency will lead to early differential diagnosis of new cases.

CHAPTER IV

COPII-DEPENDENT ECM CARGO TRAFFICKING DURING SKELETAL MORPHOGENESIS

Portions of this chapter are adapted from a research to which I contributed:

Melville DM, Montero-Balaguer M, **Levic DS**, Bradley K, Smith JR, Hatzopoulos AK, Knapik EW. (2011) The feelgood mutation in zebrafish dysregulates COPII-dependent secretion of select extracellular matrix proteins in skeletal morphogenesis. Dis Model Mech. 2011. 6:763-76.

Introduction

Growth and morphogenesis during development depends heavily on cargo trafficking and secretion (Vacaru et al., 2014). After translation in the endoplasmic reticulum (ER), most secreted protein cargo is transported to the Golgi in coat protein II complex (COPII) vesicular carriers. COPII-dependent ER-to-Golgi transport is a critical step in cargo trafficking, and lesions in COPII components lead to a variety of human diseases, including Cranio-Lenticulo-Sutural-Dysplasia (CLSD) (Boyadjiev et al., 2006), Osteogenesis Imperfecta (OI) (Garbes et al., 2015), Congenital Dyserythropoietic Anemia Type II (CDAII) (Bianchi et al., 2009), and Chylomicron Retention Disease (CMRD) (Jones et al., 2003). Notable among these examples are CLSD and CDAII, which are caused by mutations in *SEC23A* and *SEC23B*, respectively. Remarkably, SEC23A and SEC23B share more than 95% amino acid similarity, yet cause these vastly

different diseases. Similarly, mutations in *SAR1B* but not its close paralog *SAR1A* lead to CMRD, and lesions in *SEC24D* but not *SEC24A-C* are associated with OI. Animal model studies have confirmed that inhibiting specific COPII paralogs lead to unique developmental deficits that are highly similar to the respective human diseases (Lang et al., 2006; Sarmah et al., 2010; Merte et al., 2010; Wansleeben et al., 2010; Levic et al., 2015).

Two models have been proposed to explain the tissue- and cell-type specific functions of COPII paralogs. The first model proposes that COPII paralogs are subject to differential gene regulation, resulting in higher expression levels of a COPII component relative to its paralog (Fromme et al., 2008). For example, in most cell-types *SEC23A* and *SEC23B* are expressed at similar levels, so ablating either paralog alone does not inhibit COPII function in most tissues; in erythroblasts, however, *SEC23B* is expressed 5-fold more highly than *SEC23A* (Schwarz et al., 2009). Therefore, *SEC23A* can compensate for loss of *SEC23B* in most cell-types except for erythroblasts. Whether other COPII paralogs exhibit tissue-specific expression level differences similarly to *SEC23* remains unknown. Moreover, a mechanistic understanding of how differential expression could be regulated is poorly understood.

The second model to explain tissue-specific requirements of COPII components is that paralogs have acquired minor structural differences that augment their function (Melville and Knapik, 2011; Unlu et al., 2014). For example, the cargo-binding COPII component Sec24 is encoded by four paralogs in vertebrate genomes, representing two syntenic

groups of two genes. Separate Sec24 paralogs are thought to have been present within ancestral opsithokonts, indicating that paralogous expansion of Sec24 occurred early in eukaryotic evolution (Schlacht and Dacks, 2015). As such, in vertebrate genomes Sec24 paralogs in different syntenic groups are highly divergent (~20% similarity). Because of its cargo binding function (Miller et al., 2002) Sec24 paralogs' structural differences paralogs are likely to influence COPII function, as has been demonstrated with select cargos for Sec24D and Sec24B (Sarmah et al., 2010; Merte et al., 2010). Although structural differences at least partially explain the tissue-specific functions of Sec24, it is unknown whether this model applies to other COPII components. For example, Sar1 and Sec23 paralogs share greater than 95% similarity, raising the question of whether proteins that are nearly identical can have functional differences.

In this study, we explored the mechanisms underlying the tissue-specific functions of COPII components. First, we tested the structure-function model of COPII component cargo specificity, focusing on Sec23. We show that although Sec23a and Sec23b are highly conserved, a divergent 18 amino acid variable loop region influences collagen trafficking and organ morphogenesis. Second, we show analysis of a zebrafish mutant of *creb3l2*, which encodes an ER-localized transcription factor. We show that *creb3l2* mutants exhibit impaired skeletal morphogenesis due to transcriptional dysregulation of specific COPII components. Our data suggest that both structural and expression level differences underlie the tissue-specific functions of select COPII paralogs.

Materials and methods

Zebrafish lines

AB strain zebrafish were raised under standard laboratory conditions at 28.5°C (Kimmel et al., 1995). The *feelgood* allele, designated *m662*, was isolated in the MGH genetic screen (Neuhauss et al., 1996; Driever et al., 1996). All experiments were conducted in accordance with the guidelines established by the IACUC at Vanderbilt University.

Cloning and sequencing

The *feelgood* locus was mapped in an F2 intercross using bulked segregate analysis. DNA samples were PCR-genotyped with SSLP markers evenly spaced across the zebrafish genome. The mapped *feelgood* mutation was confirmed by sequencing genomic DNA flanking the mutation site from three homozygous wild-type F2 animals, five heterozygous F2 animals, six homozygous mutant F2 animals and six animals each from three different genetic backgrounds of wild-type fish (AB, IN and TL).

Cartilage proteoglycan staining

Alcian Blue staining was performed as previously described (Sarmah et al., 2010).

Immunofluorescence and lectin staining

Immunofluorescence (IF) staining was performed as previously described (Sarmah et al., 2010) using primary antibodies against collagen type II (Polysciences), collagen type IV (Lab Vision), Laminin Ab-1 (LabVision), fibronectin (Sigma), and WGA–Alexa-Fluor-

555 conjugate (Molecular Probes), followed by 1:300 Alexa Fluor 488-conjugated secondary antibody (Molecular Probes) and TO-PRO-3 or DAPI for nuclear counterstain (Molecular Probes). IF imaging was performed with an AxioImager Z1 (Zeiss) equipped with an apotome. For analysis of intracellular collagen accumulation, images were transformed into binary and the area of the intracellular collagen signal was measured in ImageJ and divided by the area of the cell.

Quantitative PCR analysis

qPCR was performed as described previously (Sarmah et al., 2010). Total RNA was extracted from approximately 30 embryos at different embryonic time points using the TRIzol reagent (Sigma). 2 mg of total RNA were reverse transcribed to cDNA using M-MLV reverse transcriptase (Promega) and poly-T primer. Each PCR reaction was performed with 1 µl of cDNA using iQ SYBR Green Supermix (Bio-Rad) and 5 µM of each primer. Primer sets used were: βactin: 5′-GACTCAGGATGCGGAAACTG-3′, 5′-AAGTCCTGCAAGATCTTCAC-3′, Creb3l2: 5′-ACAGGAGA-GTCGCAGGAAAA-3′, 5′-CACAGAACCACCACCATGAG-3′, Sec23a: 5′-AGGTGGACGTGGAGCAATAC-3′, 5′-CGAGAACG-TCTCGGAGAAAC-3′, Sec23b: 5′-ATGCTGGGACTGA-TGAAACC-3′, 5′-TCCTGTGTTTGGGAAAGTCC-3′, Sec24D: 5′-TTTGCTGACACCAACGAGAG-3′, 5′-TGATTGGGGAAC-AGGAAGAG-3′, Sec24c: 5′-CAGGGAAGAGAGTGGACTGC-3′, 5′-GTCTTCAGCTCCTGGCAAAC-3′, S1P: 5′-GGATGTGGC-GGTGTCTTACT-3′, 5′-CCTCTTACTGCGTGGAGGAG-3′, Bip: 5′-CAGGAAAGAGTAAAACAGCAACCG-3′, 5′-CCGAAAT-TTTGCTCTCACTGCATC-3′, and Sil1: 5′-CAGGAAAGAG-TAAAACAGCAACCG-

3′, 5′-CCGAAATTTTGCTCTCACTG-CATC-3′. Three independent experiments in triplicates were performed using β-actin as internal control. Thermal cycling was carried out in an iQ5 (Bio-Rad).

Generation of Tol2kit based transgenic fish

The *bactin2:sec23a:polyA, bactin2:sec23b:polyA*, *col2α1:sec23a:v2a-eGFP* and *col2α1:sec23b:v2a-eGFP* constructs were created using Gateway cloning and the "Tol2 kit" approach (Kwan et al., 2007). Constructs containing swapped 18 amino acid divergent loops were created by PCR amplification with mutagenizing primers sec23btoaF 5'GCCGCTCAAGCGGGACGCGGACCACAGCAGCCTCAGGTTCCTCC CTCCAACAGATTTCTCCAGCCTGTGC3' and sec23atobF 5'ACATCCGGCCAACAA GGAAAACCACTGGCGCCTCATGATGCTGCAGCATCCTGCAGGTTTCTCCAGC CGGTGC3' followed by dpnI digestion of plasmid template and ligation.

Electron microscopy

After being anesthetized with tricaine (Sigma), zebrafish embryos were placed into fresh 2% gluteraldehyde and incubated overnight at 4°C. Fish were washed in PBS, transferred to 1% osmium textroxide and washed in diH_2O. Fish were stained en bloc in 1% aqueous uranyl acetate for 1 hour and washed in diH_2O. The samples were taken through a series of dehydration steps starting with 30% and followed by 50%, 70%, 95% and absolute ethanol. Propylene oxide was used as a transitional solvent to replace the dehydration solution. Samples were transferred to a 1:1 araldite:propylene oxide mixture then placed in pure araldite in a vacuum oven. Pure resin specimens were then transferred into

embedding molds containing fresh resin and finally placed into a 16°C oven overnight. Ultra-thin serial sections (50–60 nm) from polymerized blocks were obtained using a Leica UCT Ultracut microtome (Leica Microsystems), transferred to Formvar-coated slot grids and examined using a Phillips CM10 TEM (FEI Company, Hillsboro, OR) equipped with an Advantage Plus 2 mega pixel Digital CCD System for CM10 TEM (Advanced Microscopy Techniques, Danvers, MA).

Phylogenetic analysis

Protein sequences (downloaded from Genbank) were aligned using ClustalW2 (http://www.ebi.ac.uk).

Results

An 18 amino acid divergent loop in Sec23 influences collagen secretion

As an entry point to understand the mechanisms underlying Sec23 paralogs' functional differences, we analyzed human SEC23A and SEC23B primary sequences and performed pairwise alignments. Although the two paralogs are conserved throughout the protein, we identified an 18 amino acid stretch in the N-terminus that is highly divergent (Fig. 4.1A). Phylogenetic analysis and subsequent pairwise alignment showed that the divergent sequence is conserved in zebrafish (not shown). The 18 amino acid stretch forms a variable loop region in the Sec23 crystal structure that is located at the interface of the Sec24 binding region (Bi et al., 2002; Mancias and Goldberg, 2008) (Fig. 4.1B).

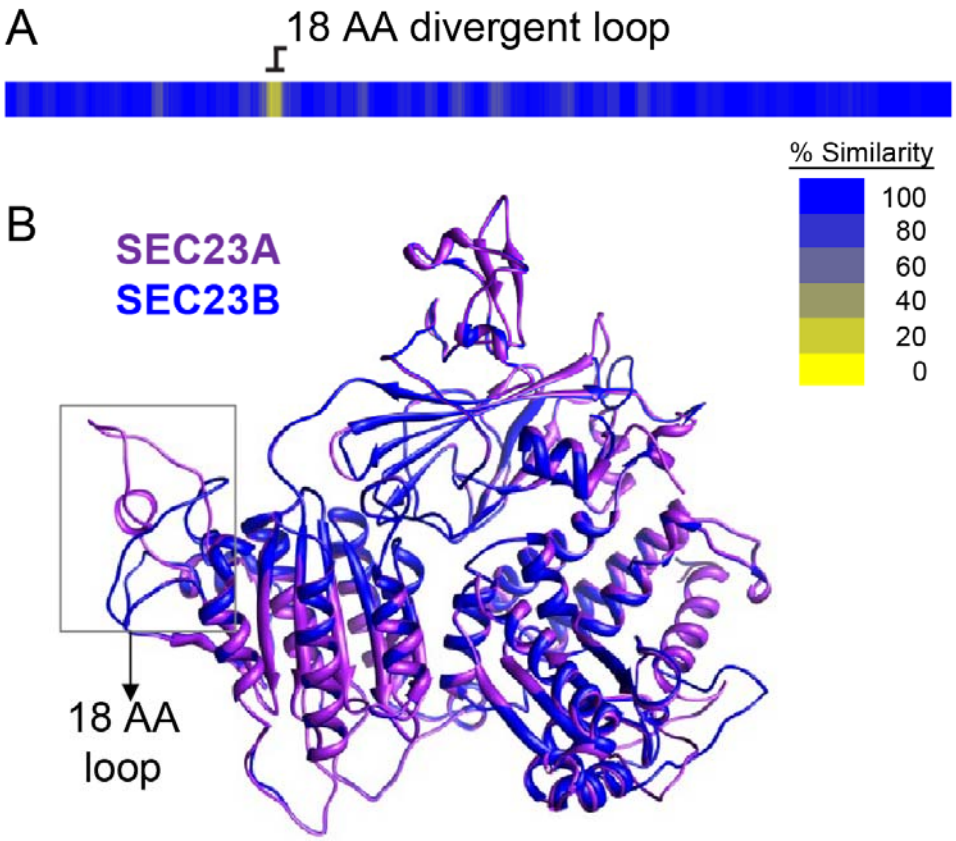

Figure 4.1. Vertebrate SEC23A and SEC23B are highly conserved but have an 18 amino acid divergent loop.
(A) Heat map secondary structure diagram showing amino acid similarity in human SEC23A and SEC23B. (B) Overlay of human SEC23A and SEC23B protein structure. The 18 amino acid loop is located adjacent to the SEC24 binding site.

To test whether the 18 amino acid loop influences cargo trafficking, we performed structure-function studies using genetic replacement with different Sec23 constructs in *sec23a* null mutant zebrafish (Lang et al., 2006). We assembled transgenes containing a *collagen2α1* promoter driving Sec23 linked to a viral 2a (v2a)-eGFP transgenic reporter. Injection into one blastomere of a 2-4 cell stage embryo results in mosaic expression of untagged Sec23 and eGFP in isolated chondrocytes at 3-5 dpf. Using this approach we expressed either Sec23a, Sec23b, Sec23a with the Sec23b loop (Sec23a/b-loop), or Sec23b with the Sec23a loop (Sec23b/a-loop) in *sec23a* mutant chondrocytes (Fig. 4.2A).

Compared to neighboring non-transgenic *sec23a*$^{-/-}$ cells that contained large intracellular collagen deposits, GFP+ chondrocytes expressing any of the Sec23 constructs partially restored collagen secretion. Sec23a expression significantly reduced intracellular collagen and resulted in the formation of collagen-rich lacunae encompassing the GFP+ cells. Expression of Sec23b and the loop-swap constructs similarly restored collagen secretion, although less effectively that Sec23a (Fig. 4.2B).

To analyze intracellular collagen accumulation quantitatively, we performed thresholding to detect collagen IF signal and then measured the portion of cytosol area containing collagen. The results showed that Sec23a expression nearly completely restored collagen secretion, while Sec23b expression did not significantly rescue collagen backlog. When the 18 amino acid loop regions were exchanged for Sec23a and Sec23b, this trend was reversed: Sec23b/a-loop restored collagen secretion more effectively that Sec23a/b-loop (Fig. 4.2C). These data show that Sec23b can partially compensate for loss of Sec23a in

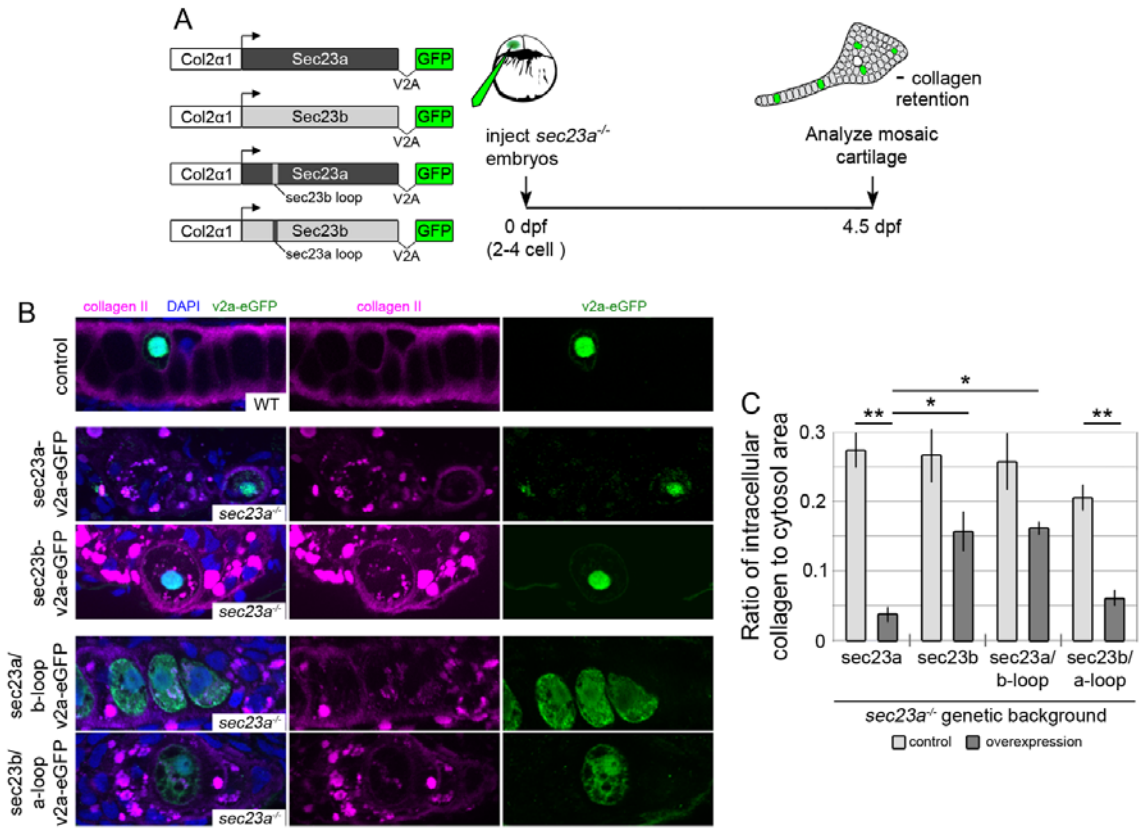

Figure 4.2. The Sec23 divergent loop influences collagen secretion in chondrocytes. (A) Experimental strategy for cell autonomous rescue experiments using mosaic transgenic overexpression. A minimal portion of the *col2α1* promoter drives the expression of untagged sec23 and a viral2a (v2a)-eGFP transgenic reporter in isolated chondrocytes. (B) Mosaic expression of WT and loop-swap sec23 constructs in 4 dpf WT and *sec23a*$^{-/-}$ mutant cartilage. Non-transgenic *sec23*$^{-/-}$ cells exhibit large accumulations of collagen II in the cytosol due to retention in rER (Lang et. al., 2006), but Sec23a and Sec23b/a-loop expression efficiently restores collagen secretion (arrows). Sec23b and Sec23a/b-loop also partially rescues collagen retention (arrowheads). (C) Quantification of collagen II cytosol retention in control and Sec23-overexpression mutant chondrocytes. Constructs containing the Sec23a divergent loop lead to reduced intracellular collagen. *p<0.05 **p<0.01, two-way ANOVA

collagen trafficking, and when its 18 amino acid look is substituted with the Sec23a variable loop, rescue of collagen traffic is comparable to Sec23a. In contrast, the Sec23b 18 amino acid loop substitution reverts the ability of Sec23a to promote collagen secretion to a much lower level comparable to Sec23b.

These data suggests that the Sec23a variable loop is sufficient to increase collagen traffic specificity in the Sec23b paralog and is necessary for collagen export from the cell.

Paralog-specific function of Sec23 in fin morphogenesis

Sec23a$^{-/-}$ mutants exhibit kinks in the pectoral fins (Lang et al., 2006) that occur at actinotrichia, which are collagen rich spicules forming fan-like arrays at the distal fin end. Similar to craniofacial chondrocytes, *sec23a*$^{-/-}$ cells in the distal fin have accumulations of collagen, and the extension of proteogycans to the actinotrichia is impaired (Figure 4.3). To test Sec23 paralog-specific function in tissue morphogenesis, we assembled transgenes containing the semi-ubiquitous β-actin promoter driving expression of Sec23a, b, a/b-loop, or b/a-loop, along with a separate cmlc2:eGFP transgenic reporter. We then injected one cell stage *sec23a*$^{-/-}$ embryos for broad transgenic incorporation throughout the embryo and selected embryos with strong cmlc2:eGFP expression for analysis. Sec23a expression partially reduced collagen accumulations in the distal fin and increased proteoglycan extension past the actinotrichia (Fig. 4.3), resulting in significantly fewer kinked fins *sec23a*$^{-/-}$ larvae. In contrast, Sec23b expression did not improve collagen secretion, proteoglycan extension or fin morphology. Substitution of the Sec23b loop with that of Sec23a, however, partially

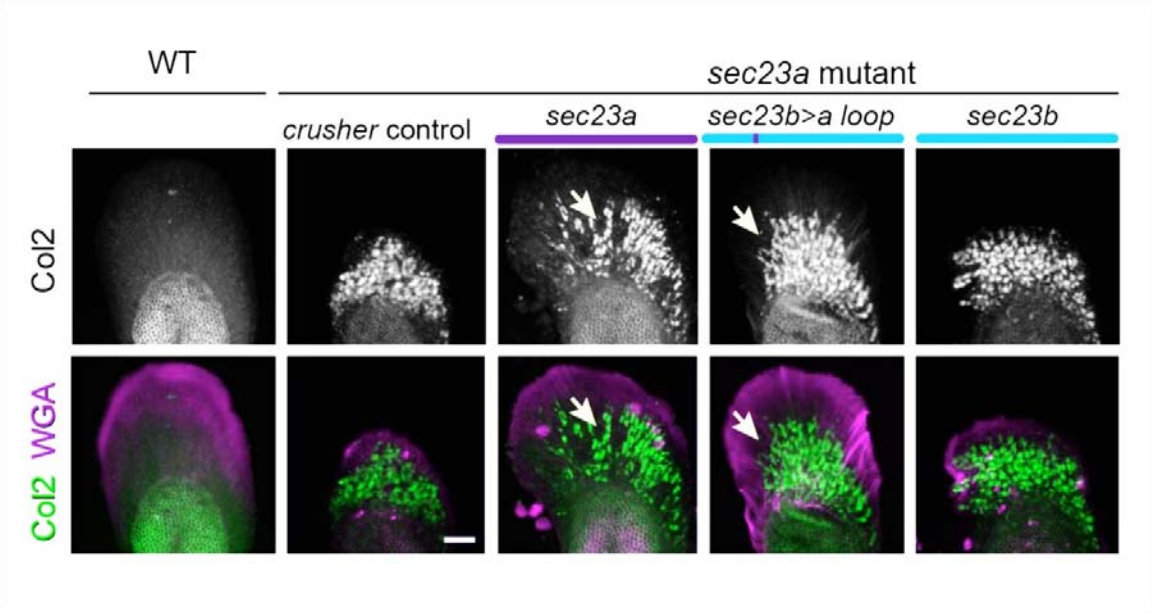

Figure 4.3. Sec23a is specifically required for fin morphogenesis.
Immunofluorescence of col2 and lectin staining of proteoglycans (WGA) in the pectoral fin actinotrichia of 6 dpf embryos expressing the indicated constructs.

restored proteoglycan extension and fin morphogenesis (Fig. 4.3). In summary these data show that, although highly conserved, Sec23a and Sec23b function differently in cargo transport, and an 18 amino acid divergent sequence partially confers these differences.

The zebrafish *feelgood* mutation causes craniofacial defects

To discover potential regulators of COPII-dependent trafficking, we analyzed a zebrafish mutant with highly similar phenotypes to *sec23a*$^{-/-}$ embryos. Toward this aim, we focused on the *feelgood* mutant. The primary features of the *feelgood* phenotype include a reduced lower jaw, shortened body length, and compact head, trunk and tail as measured from the posterior edge of the ear capsule to the tip of the tail (Fig. 4.4A-D). Alcian blue staining reveals that all cartilage elements of the head skeleton are present in *feelgood* mutants, but they are shortened and malformed, including abnormal curvature of the Meckel's and ceratohyal cartilages, and failure of the Meckel's cartilage to taper towards the anterior end (Fig. 4.4E-F). Thus, the spectrum of *feelgood* morphological phenotypes closely resemble those of *sec23a*$^{-/-}$ mutants (Lang et al., 2006).

Type II collagen trafficking is disrupted in *feelgood* mutant chondrocytes

To investigate whether abnormal cartilage shape in *feelgood* mutants is associated with impaired ECM cargo trafficking, as is the case with *sec23a*$^{-/-}$ and *sec24d*$^{-/-}$ mutants mutants (Lang et al., 2006; Sarmah et al., 2010), we examined the distribution of type II collagen (col II) in cartilage at 5 dpf, a stage following rapid cartilage growth and ECM deposition (Kimmel et al., 1998).

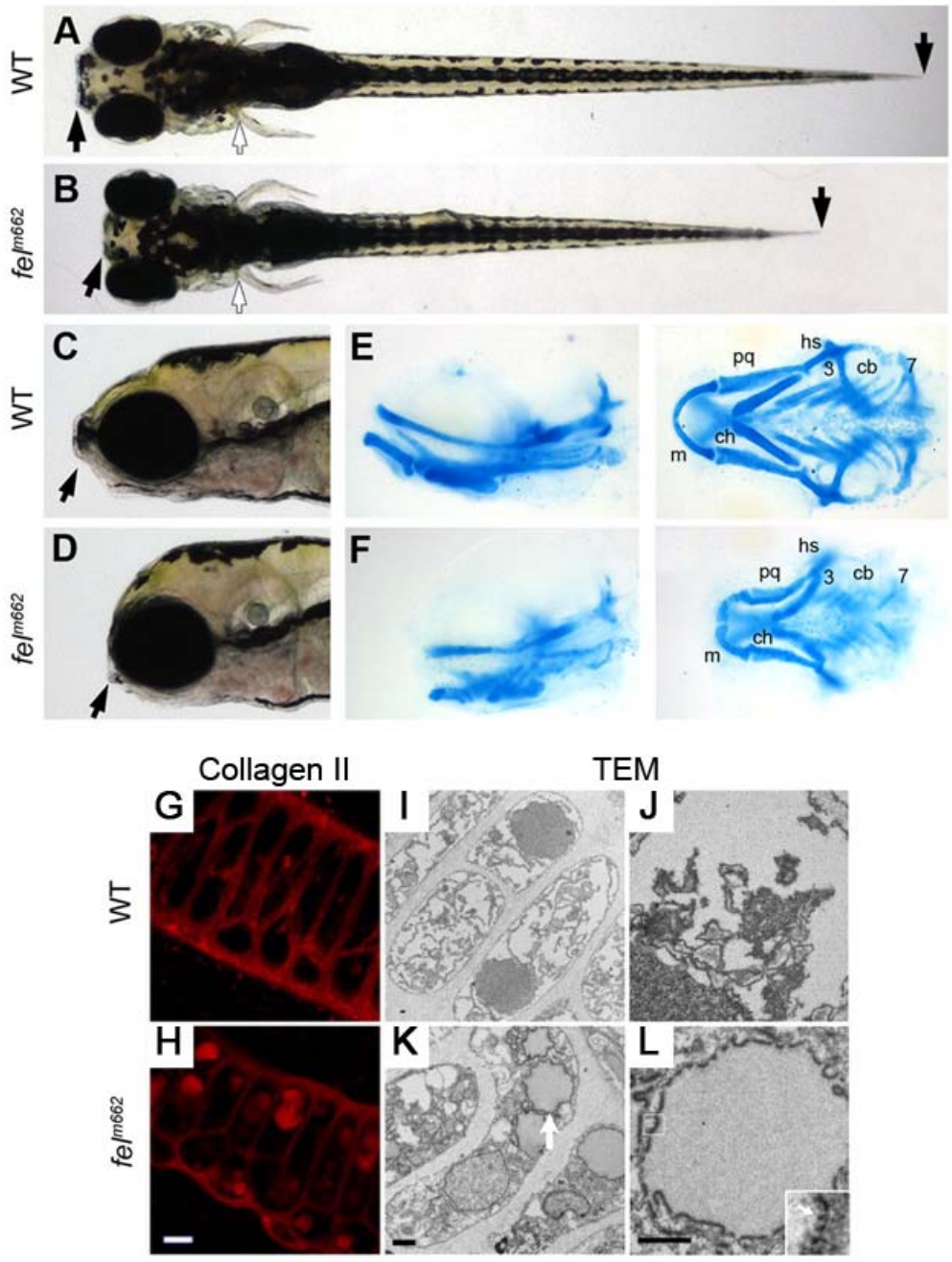

Figure 4.4. The *feelgood* mutation affects craniofacial skeletal development.
(A–D) Live images of wild-type (WT) and *feelgood* (*fel*^{m662}) embryos at 5 dpf. Arrows indicate reduced length of head and trunk in dorsal (A,B) and lateral (C,D) views. (E–F) Alcian blue staining of cartilage elements in head skeleton in lateral and ventral views. cb, ceratobranchials 3–7; ch, ceratohyal; hs, hyosymplectic; m, Meckel's cartilage; pq, palatoquadrate. (G-H) Col II immunofluorescence in 5 dpf WT and *feelgood* cartilage. (I-L) TEM analysis of 5 dpf WT and *feelgood* cartilage. Arrow indicates distended rER.

In 5 dpf WT embryos, col II was primarily localized to the extracellular space (Fig. 4.4G), with small clusters of intracellular staining representing their traffic through the secretory pathway. In *feelgood* mutants, immunofluorescence staining revealed deposition of col II to the extracellular space but also accumulation in cytosolic vesicle-like structures, which were larger and denser than the corresponding intracellular compartments in wild types (Fig. 4.4F).

To identify the intracellular localization of protein buildup, we used transmission electron microscopy (TEM). TEM images showed that WT chondrocytes were stacked in a regular fashion and many had undergone hypertrophic differentiation, lacking dense rough ER (Fig. 4.4I-J), which can be easily identified by ribosome studded membrane (Lang et al., 2006). *Feelgood* chondrocytes, in contrast, had a round morphology and were irregularly spaced, suggesting stacking defects (Fig. 4.4K). Additionally, mutant chondrocytes were arrested at earlier stages of maturation, containing large vacuoles of distended ER membranes filled with electron dense material consistent with collagen fibrills (Fig. 4.4L).

Together, these data indicate that the jaw deformity in *feelgood* mutants is a consequence of abnormal collagen secretion and continuous intracellular protein buildup. They also suggest that the maturation of *feelgood* chondrocytes towards a hypertrophic state is delayed or stalled, subsequent to insufficient matrix deposition.

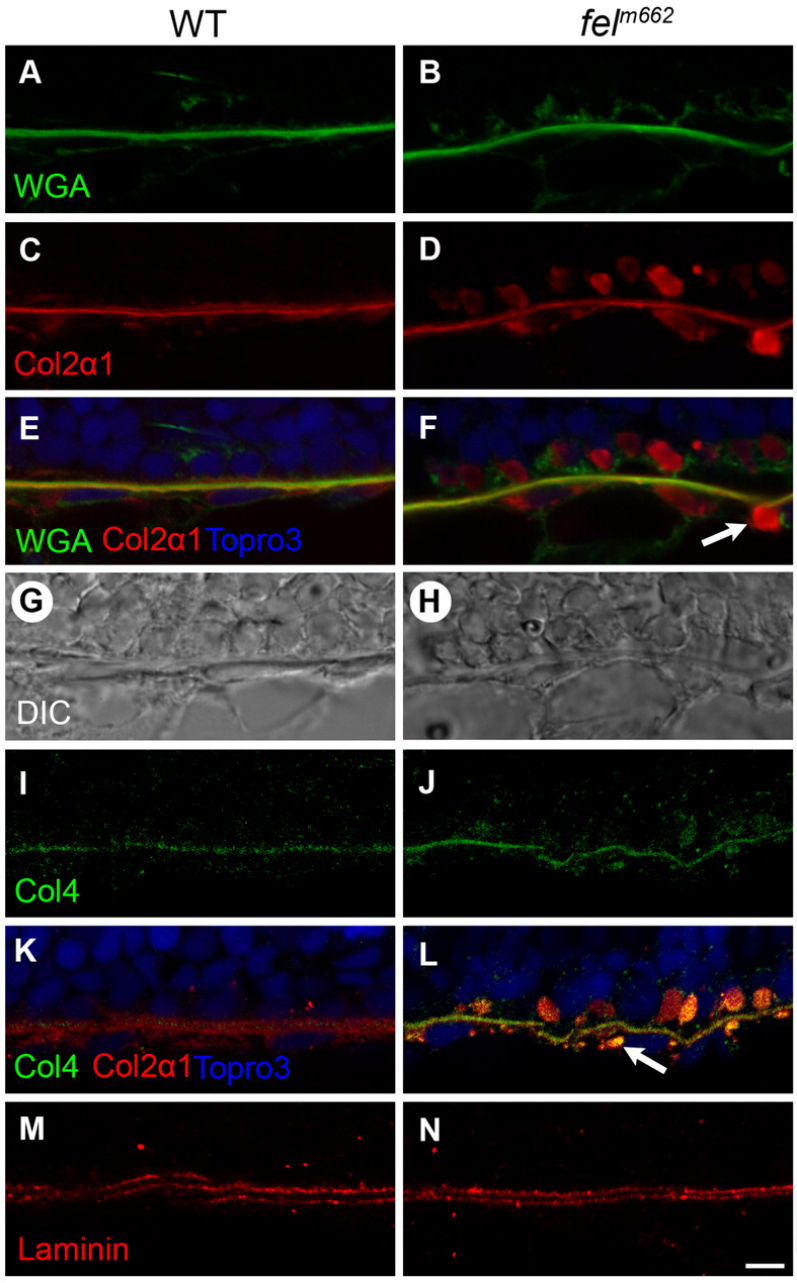

Figure 4.5. Collagen trafficking is preferentially disrupted in *feelgood* mutants, leading to notochord defects.
(A–F) Immunofluorescence of WGA, Col2α1 and merged images of 15-μm sagittal sections of the notochord of 28-hpf embryos. Arrow indicates vesicle-like collagen staining outside the notochord sheath. (G,H) DIC images of the corresponding sections in A–F. (I–N) Immunofluorescence of type-IV and type-II collagen (I–L) and laminin (M,N) in 15-μm sagittal sections of the notochord at 28 hpf. Scale bar: 5 μm.

Notochord sheath formation, but not glycosaminoglycan secretion, is disrupted in *feelgood* mutants

Feelgood mutant embryos exhibit shortened body length, indicating impaired notochord development. The embryonic notochord functions as a hydrostatic skeleton, and this mechanical property is conferred by an external fibrous sheath consisting primarily of collagen and laminin ECM as well as numerous internal vacuoles that enclose hygroscopic glycosaminoglycans (GAGs). These biomechanical components exert the appropriate notochord stiffness that is essential for embryo lengthening and maintenance of straight posture.

To determine the secretory status of GAGs in the notochord sheath, we used WGA staining. The results show that, at 28 hpf, WGA-stained proteins are present in the extracellular space of *feelgood* embryos similar to WT embryos, indicating that GAG trafficking in notochord sheath cells is unaffected in mutants (Fig 4.5A-B). The major components of the notochord sheath are type II and type IV collagen fibrils that are interlinked with laminins, nidogen and fibulins, representing a specialized basement membrane. We analyzed type II and type IV collagen localization by immunofluorescence and found that both are abnormally positioned within large vesicle-like structures similar to those seen in the craniofacial cartilage (Fig.4.5C-F, I-L).

To test whether secretory defects extend to other ECM proteins in *feelgood* notochord cells, we analyzed the localization of laminin in the notochord and somitic boundaries. In contrast to collagens, laminin secretion was not disrupted in *feelgood* mutants (Fig. 4.5M-

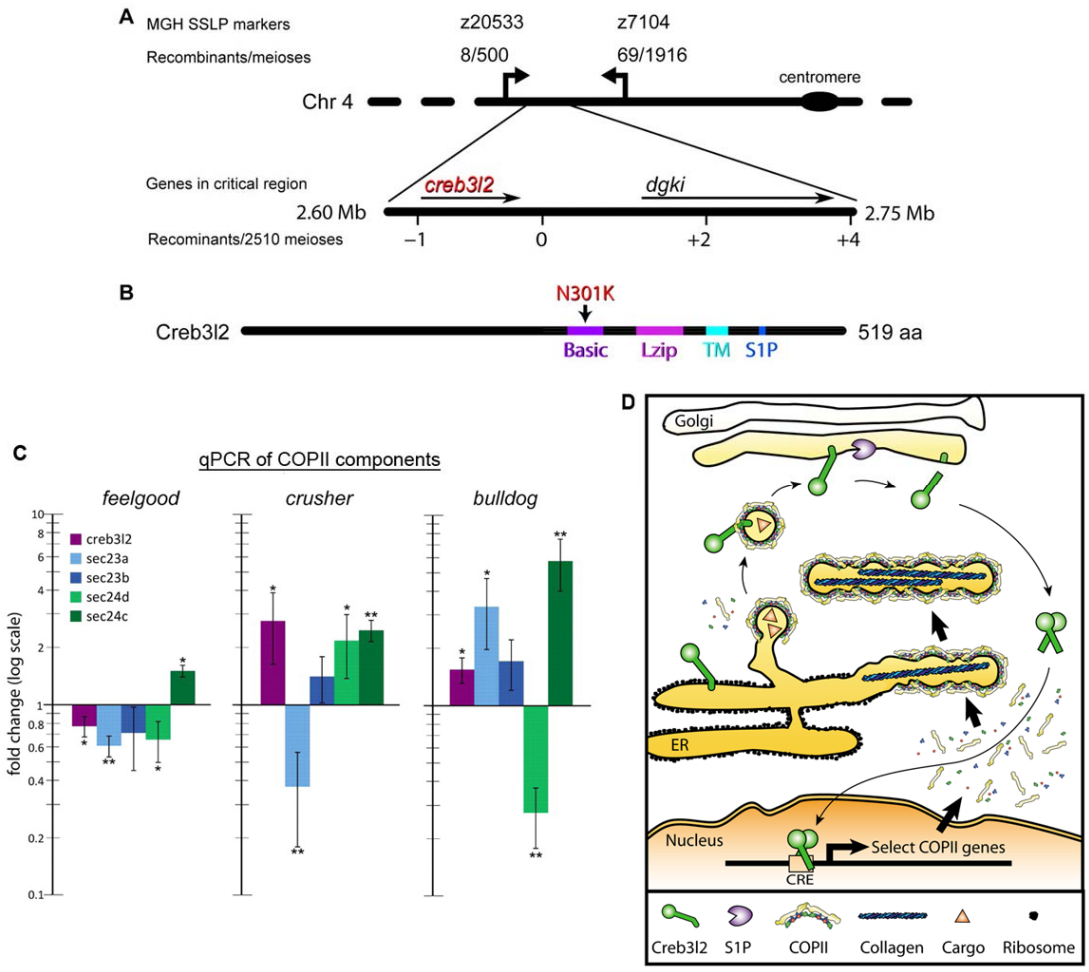

Figure 4.6. *Feelgood* is a missense mutation in *creb3l2*, which selectively regulates COPII component expression.

(A) The *feelgood* mutation was mapped to chromosome 4 between SSLP markers z20533 and z7104. Novel SSLP markers with the indicated number of recombinants reduced the critical interval to a ~50 kb region that contained two genes. The physical map of the critical region was based on the Zv7 assembly. (B) Schematic diagram of the Creb3l2 primary structure illustrating a missense N301K mutation in the DNA-binding basic motif. Basic, basic motif; Lzip, leucine zipper motif; TM, transmembrane domain; S1P, Site-1 protease recognition sequence. (C) qPCR analysis of the fold expression change of COPII-related transcripts *creb3l2*, *sec23a*, *sec23b*, *sec24d* and *sec24c* in *feelgood*, *crusher* (*sec23a*) and *bulldog* (*sec24d*) mutants compared with wild types. RNA was extracted form whole embryos at 80 hpf. All results are normalized to β-actin and then to wild type. **P*<0.05; ***P*<0.005. (D) Model of Creb3l2 function. When the secretory load of a wild-type cell increases beyond the capacity of the basal level of COPII protein expression, Creb3l2, which is normally localized in the ER, is cleaved by cis-Golgi-resident S1P. After cleavage, Creb3l2 dimerizes and enters the nucleus to bind *cre* sites in the promoters of select COPII genes, upregulating their expression and increasing the secretory capacity of cell.

N). Together, these data indicate a selective defect in cargo trafficking in *feelgood* mutants, in which large fibrillar proteins (collagens) are retained in rough ER, while relatively smaller GAGs and basement membrane proteins (laminin) are transported and secreted from the cell. These deficits impair the function of skeletal tissues in head and trunk but otherwise do not significantly affect patterning and organogenesis.

The *feelgood* mutation disrupts the *creb3l2* locus

The similarities between the *feelgood* phenotype and those of *sec23a*$^{-/-}$ and *sec24d*$^{-/-}$ mutants suggested that the *feelgood* locus encodes a protein participating in COPII-mediated transport. To identify the chromosomal location of the *feelgood* mutation, we used a positional cloning strategy. We genotyped fish from an F2 intercross and used the zebrafish genetic linkage map (Knapik et al., 1998) to establish that the *feelgood* mutation is located in a 5.2 cM region on the proximal arm of chromosome 4 (Fig. 4.6A). We then developed novel SSLP markers and calculated recombination events in a 2510 meioses F2 map cross to restrict the critical interval to a 58 kb region flanked proximally by a marker within an intron of the *creb3l2* gene, and distally by a marker in intron 20 of the *diacylglycerol kinase, iota* (*dgki*) gene. No other known genes are present in the critical region (Fig. 4.6A).

Sequencing of the coding region of the two candidate genes revealed a single C>G transversion at base pair 1128 of the *creb3l2* gene that results in an N301K missense mutation (Fig. 4.6B). The Creb3l2 protein contains a basic leucine zipper domain consisting of a basic motif that mediates sequence-specific DNA binding, a leucine

zipper motif that facilitates protein dimerization (Vinson et al., 1989) and a single-pass transmembrane domain preceding a Site-1 protease (S1P) recognition site (Fig. 4.6B). The *feelgood* mutation is located within the DNA-binding basic motif of Creb3l2, in a segment that is conserved from *Caenorhabditis elegans* to human. *Creb3l2* belongs to a family of five paralogs that are highly conserved among vertebrate species, including zebrafish.

The *feelgood* mutation leads to decreased expression levels of select cargo adaptor proteins

Collectively, our results indicate that *feelgood* (*creb3l2*) mutants have similar phenotypes as *sec23a*$^{-/-}$ and *sec24d*$^{-/-}$ mutants (Lang et al., 2006; Sarmah et al., 2010). This raises the possibility that the *feelgood* mutation leads to lower expression levels of *sec23a* and *sec24d.* Sec23A was previously shown to be a direct target of Creb3l2 (Saito et al., 2009a). We also found that Creb3l2 itself has a conserved *cre* site in its promoter, and therefore might be self-regulated.

To test whether the putative targets of Creb3l2 – *creb3l2*, *sec23a* and *sec24d* – are dysregulated in *feelgood* mutants, we analyzed total RNA samples from 80-hpf embryos. We also included *sec24c* and *sec23b* for comparison. Quantitative real-time PCR (qPCR) results show that the expression levels of *creb3l2*, *sec23a* and *sec24d* are decreased in *feelgood* mutants relative to WT embryos (Fig. 4.6C). In contrast, *sec24c* levels are upregulated in *feelgood* mutants. This outcome could be either due to *sec24c*

upregulation through Creb3l2-independent, compensatory mechanisms, or a Creb3l2-mediated, indirect suppression of *sec24c*.

To test whether expression levels of Creb3l2 targets are altered by disruption of ER-to-Golgi protein trafficking independently of Creb3l2, we analyzed RNA samples from *sec23a*$^{-/-}$ and *sec24d*$^{-/-}$ mutants. The results show that the expression levels of *creb3l2*, *sec23a* and *sec24d* are increased in these mutants relative to WT embryos, except for *sec23a* and *sec24d* in their respective mutants, which might be due to nonsense-mediated decay (Fig. 4.6C), while *sec24c* is increased in all three mutants.

Taken together, our results demonstrate that Creb3l2 regulates the expression of multiple COPII components. Interestingly, there is no evidence that the expression of *sec24c* is regulated by Creb3l2, consistent with the lack of craniofacial dysmorphology in *sec24c* morphants (Sarmah et al., 2010). Similarly, *sec23b* is modestly but not significantly downregulated in *feelgood* mutants, indicating that Creb3L2 selectively regulates the expression of COPII paralogs.

Discussion

In this study we present in vivo analysis of cargo trafficking to understand mechanisms underlying the tissue-specific functions of COPII component paralogs. Using the COPII inner coat components Sec23 and Sec24 as examples, we show that COPII paralogs have tissue-specific functions during development due to both structural variation and

differential transcriptional regulation. Our study provides a framework for understanding why mutations in COPII paralogs lead to vastly different human diseases.

Structure-function differences in COPII component paralogs

Sec23a, although 95% similar to Sec23b, is uniquely required for skeletal morphogenesis due to its function in collagen transport (Boyadjiev et al., 2006; Lang et al., 2006). Using cell-autonomous replacement assays, we found that Sec23b overexpression in *sec23a*$^{-/-}$ chondrocytes partially restored collagen secretion. Moreover, exchanging an 18 amino acid divergent loop in Se23b with that of Sec23a significantly reduced intracellular collagen backlog. Also consistent with this notion, our preliminary analysis indicates that collagen trafficking is not impaired in *sec23b* morphant embryos (not shown). Thus our data indicate that short sequence variations in Sec23 paralogs augment their cargo trafficking functions and partially explain their differential requirements during development.

Sec23 is not known to influence cargo selection for COPII vesicles, so it will be important to address how Sec23 regulates the transport of specific cargos. One possible explanation is the differential interaction of Sec23 with Sec24 paralogs, which regulates COPII cargo selection (Miller et al., 2002). The 18 amino acid loop of Sec23 that confers cargo specificity is located adjacent to the Sec24-interacting region. Therefore, Sec23a could preferentially interact with Sec24d, which is uniquely required for collagen transport among the Sec24 paralogs (Sarmah et al., 2010). According to this model,

different Sec23/Sec24 heterodimers regulate the transport of unique cargos, with Sec23a being a critical partner of the collagen specific Sec24d.

Transcriptional regulation of cargo trafficking

An important question in cell biology is how the trafficking demands of different cell-types coordinate with the secretory pathway to provide sufficient availability of cargo trafficking components. Conceivably, the secretory pathway responds to broad and constant demands for cargo delivery during development, physiological changes, and tissue repair. The mechanisms that govern these functions are poorly understood.

Using a forward genetics approach, we identified a missense mutation in *creb3L2* (*cAMP responsive element binding protein-3 like 2*) that results in similar phenotypes to *sec23a*$^{-/-}$ and *sec24d*$^{-/-}$ mutants. Creb3L2, also known as BBF2H7, is an ER-resident, transmembrane transcription factor that is highly expressed in chondrocytes. After COPII-dependent ER export, Creb3L2 is cleaved in the Golgi to an active, soluble peptide that dimerizes and then is translocated to the nucleus to activate the expression of target genes (Panagopoulos et al., 2007; Lui et al., 2008).

We found that Creb3L2 selectively regulates the expression of multiple COPII components. In addition its previously identified target Sec23a (Saito et al., 2009a), Creb3L2 is also required for Sec24D expression. Interestingly, the expression of other Sec23 and Sec24 paralogs were not significantly altered, demonstrating for the first time that COPII component paralogs are subject to differential expression regulation. We also

found that trafficking of collagen II in chondrocytes and collagen IV in notochord sheath cells were disrupted, whereas other cargos including laminins were not affected. These data suggests that spatio-temporal expression of COPII components is differentially regulated by Creb3L2.

Why are skeletal tissues specifically affected in *creb3l2* and other COPII mutants? We propose that in most cell-types large cargo secretion is modest and available coats from other COPII component paralogs are sufficient for proper trafficking. In specialized secretory cells that secrete high volumes of large cargo such as fibrillar collagen, specialized COPII coats formed by Sec23a and Sec24d are required to meet the demands of the cell. With decreased levels of Sec23a or Sec24d, there might be insufficient levels of COPII components to build the more complex tubular structures required for large cargos (Stagg et al., 2008), while the transport of smaller cargo into simpler COPII carriers proceeds normally (Fig. 4.6D).

Creb3L2 is, so far, the only transcription factor identified as a regulator of COPII-dependent collagen secretion. Future studies are needed to discover transcriptional regulatory mechanisms for the specific COPII components and mediators of post-translational modifications important for ECM secretion.

CHAPTER V

DISCUSSION AND FUTURE DIRECTIONS

Summary

The research presented here illustrates the utility of animal model studies for discovering tissue-specific functions of cargo trafficking components during development and for modeling human disease. The ability to combine forward genetics, in vivo imaging, and genetic mosaic analysis provides a system that is amendable to studying organogenesis at a cellular and molecular level. This principle is demonstrated by the studies detailed in Chapter II, where a genetic mutant from a phenotype-driven screen was the basis for discovering a mechanism that coordinates post-Golgi cargo trafficking, ECM secretion, and cell growth during organogenesis. Animal models can also be used for studying the pathogenesis of human diseases related to cargo trafficking. This concept is shown in Chapter III, where a reverse genetics approach was used to uncover a novel function of pre-Golgi trafficking in cholesterol uptake in the gut, providing a potential mechanistic basis for chronic hypocholesteremia in Chylomicron Retention Disease. The remainder of the current chapter discusses the implications and significance of these findings and outlines future lines of investigation.

Cytoskeletal regulation of cell shape in epithelial versus mesenchymal cells

In recent years many impactful studies have shown that cell shape regulation is critical for tissue and organ morphogenesis. For example, cell elongation in epithelia helps to orient cell divisions to promote cell spreading during early gastrulation (Campinho et al., 2013), whereas in lung epithelia, polarized cell shape changes induce tissue folds to help define branch points during early morphogenesis (Kadzik et al., 2014). These and other studies have helped to uncover how epithelial cell shape is regulated in vivo. Two common themes that have emerged from epithelial cell shape studies are 1) cell shape changes often rely heavily on non-cell-autonomous forces transmitted through junctional complexes and 2) these forces are typically mediated by actomyosin-based contraction. For example, apoptotic cells in some epithelia generate force in an actomyosin-dependent manner to shape neighboring cells and drive tissue folding (Monier et al., 2015).

Given that cell-cell junctions are crucial for epithelial cell shape regulation, and given that most studies of cell shape regulation have used epithelial models, this raises the question of how shape is regulated in mesenchymal cells. By definition, mesenchymal cells are isolated cells with no intercellular junctional complexes, so they likely regulate cell shape differently than epithelial cells. To date, mesenchymal cell shape regulation has remained poorly understood and has only been studied using cell culture models (Picone et al., 2010; Straube and Merdes, 2007). While potentially important as a discovery tool, in vitro studies of cell shape regulation are fundamentally lacking because these systems typically fail to maintain a physiologically relevant arrangement of multiple cell types within a native extracellular matrix, which could have important

effects on cell shape. It is therefore important to test whether mechanisms identified in cell culture models are relevant to mesenchymal cells in vivo. Nonetheless, cell culture studies have led to important findings. For example, in cultured myoblasts, cell elongation depends on parallel microtubule organization, and when EB3 (microtubule end-binding protein 3) is depleted, cortical microtubule dynamics are altered and cells fail to elongate (Straube and Merdes, 2007). Similarly, in HeLa cells and cultured drosophila S2R+ cells, cell elongation is dependent on microtubule dynamics and is independent of actomyosin machinery. During cell elongation, microtubules become oriented with the long cell axis, and regulation of microtubule stability at the cell cortex is critical for proper cell shape changes (Picone et al., 2010). These studies indicate that mesenchymal cell shape, unlike that of epithelia, relies on microtubules rather than actomyosin-based forces.

The work described in chapter II has helped to uncover how mesenchymal cell shape is regulated. A major unanswered question in the field was how changes in cortical microtubule dynamics could regulate cell shape. Microtubule dynamics (polymerization) likely do not promote cell growth through force generation that because in isometrically growing cells mechanical strain on microtubules decreases (Hu et al., 2004). This idea is further supported by the fact that microtubules often buckle when they extend to the cell cortex, indicating that microtubule filaments are not stiff enough to withstand the mechanical strain that would be required for substantial physical pushing (Dogterom et al., 2005). Therefore, microtubules likely function fundamentally differently than actin in cell shape regulation, but the mechanisms by which cortical microtubules affect cell shape changes were previously unknown.

The work outlined in Chapter II provides the first in vivo testable model of how microtubule organization influences cell shape. I found that Erc1 localizes to the cell cortex, where it regulates cortical microtubule organization and polarity during chondrocyte cell elongation. In the absence of Erc1, microtubule plus ends are enriched at polarized growing ends of the cell and diminished at the lateral margins. As a result, cargo trafficking along microtubule tracks becomes biased towards polarized cell ends and the cells elongate but fail to maintain cell width. Thus, my data indicate that in growing chondrocytes microtubules influence cell shape changes by acting as a conduit for directed cargo delivery (i.e. lipids or specialized proteins) to the cell surface.

Molecular components that function in mesenchymal cell shape regulation

Another open question concerned the auxiliary proteins that function in microtubule-dependent cell shape regulation. Before my work, EB3 was the only such protein identified (Straube and Merdes, 2007). In addition to microtubule-associated proteins (MAPs) such as EB3, cortical proteins are also likely to function in cell shape regulation. This idea is supported by experiments using elongating HeLa cells, where it was shown that microtubules are initially radially arrayed but then become oriented toward the growing ends of the cell. Microtubules that approach the lateral (non-growing) sides of the cell remain dynamic and extend toward polarized cell ends, where they are "captured" (Picone et al., 2010). Although cortical microtubule capture has not been examined in the context of cell growth, it has been studied in non-motile cells that have long, radial microtubules terminating at the cell cortex. The presence of long, stable

microtubules contrasts with the dynamic instability model of microtubule behavior, which involves periods of rapid growth and destabilization (Gardner et al., 2013). This difference in behavior during cortical capture is regulated by the concerted action of specific MAPs and cortical proteins, which together function to locally suppress dynamic instability at the cell cortex. This is supported by studies showing that inhibiting cortical capture components such as LL5β or KIF21A results in decreased microtubule stability or microtubule overgrowth, respectively (Lansbergen et al., 2006; van der Vaart et al., 2013).

The fact that mesenchymal cell shape changes depend on cortical microtubule dynamics and seem to involve cortical capture (Straube and Merdes, 2007; Picone et al., 2010) suggests that, in addition to EB3, other MAPs and cortical proteins may also function in this process. My dissertation research is the first to identify a cortical protein, Erc1, that functions in microtubules-dependent cell shape regulation.

To further delineate how mesenchymal cell shape changes are regulated, it will be important to determine precisely how Erc1 influences microtubule polarity and organization in chondrocytes. Erc1 does not directly interact with microtubules and it has not been shown to bind to any MAPs that were tested (Lansbergen et al., 2006). Nonetheless, Erc1 does regulate cortical microtubule organization, but it does so indirectly by acting as a scaffolding component at cortical platforms, which function as capture sites for microtubule plus-ends. A logical prediction would be that Erc1 regulates microtubule organization in chondrocytes in a similar fashion as it does in cultured cells. However, my data argue against this possibility. Namely, I found that inhibiting Rab8 or Kinesin-1 phenocopies the Erc1 loss-of-function cell shape. Rab8 and Kinesin-1 have

been shown to function in Erc1-dependent exocytic traffic, but they are not known to regulate cortical microtubule capture and they do not localize to cortical platforms (Grigoriev et al., 2007, 2011). Given that loss of Erc1, Kinesin-1, and Rab8 each results in cell shape dysregulation, and given that combined loss of Erc1 and either Rab8 or Kinesin-1 does not alter severity of the cell shape phenotype, my studies indicate that each of these 3 components functions in the same pathway to regulate cell elongation. Thus, in chondrocytes Erc1 likely influences microtubule organization through regulation of exocytic traffic rather than through cortical microtubule capture as in HeLa cells.

Cell polarity and cell shape regulation

It remains unclear how loss of exocytic trafficking components leads to changes in microtubule polarity and organization. One possibility is that Erc1-dependent trafficking is required to establish or maintain chondrocyte cell polarity and that microtubule organization is a secondary effect of changes in cell polarity. This idea is supported by studies showing that regulation of cell polarity is required for chondrocyte cell shape changes. Several genes have been identified in this process, including members of the heparin sulfate proteoglycan synthesis pathway, such as gpc4 (glypican 4) (Topczewski et al., 2001; LeClair et al., 2009) and ext2 (exostosin glycosyltransferase 2) (Clément et al., 2008), as well as components of the wnt/planar cell polarity pathway, including wnt5 (Yang et al., 2003) and fzd7 (frizzled 7) (Li and Dudley, 2009). Inhibition of these components results in clusters of non-stacked rounded chondrocytes, rather than stacks of elongated cells, due to a failure of initiating proper polarity (Topczewski et al.,

2011). Additionally, the orientation of the microtubule organizing center (MTOC) is altered in chondrocytes when cell polarity components are inhibited (Le Pabic et al., 2014), suggesting that microtubule polarity may be a downstream effector of cell polarity signaling in chondrocytes. Future studies examining cell polarity markers before the onset of cell shape changes in Erc1-, Rab8-, and Kinesin-1-deficient chondrocytes will help to address these questions.

Rab11-dependent cargo traffic and cell shape regulation

An interesting finding I made is that inhibiting the function of Rab11, which has an evolutionarily conserved role in regulating cell polarity and membrane recycling (Welz et al., 2014), suppresses cell shape changes in Erc1-deficient chondrocytes. I interpret these data to indicate that chondrocyte cell shape changes depend membrane recycling through Rab11-positive compartments, which then deliver new membrane or specialized cargo to the cell surface via exocytic traffic along microtubules. In Erc1-deficient chondrocytes, Rab11-dependent traffic is enriched towards polarized cell ends due to changes in microtubule polarity, leading to cells that are elongated but collapsed in width. It will be important to further test how Rab11 regulates chondrocyte cell shape changes. Interestingly, expression of dominant-negative dynamin-1 (K44A) failed to suppress cell shape changes in Erc1-deficient cells similarly to Rab11 (data not shown). However, dynamin-1 regulates clathrin-mediated endocytosis, which represents only a subset of endocytic events, so it is possible that non-clathrin mediated endocytosis could contribute to cell shape changes.

We also found that, in WT chondrocytes, eGFP-Rab11 predominately localizes near the cell cortex, similar to that of Erc1. The similar localization, along with our genetic interaction data, raise the question of whether Erc1 and Rab11 might physically interact. In fact, Erc1 contains a predicted Rab11-interacting domain (RBD-FIP) at the C-terminus, which has not been investigated to date. The RBD-FIP domain of Erc1 is located in a region of the protein that is alternatively spliced (Wang et al., 2002), such that the domain is present in the longer Erc1a isoform but not in Erc1b. In our study, however, the shorter Erc1b was used for the rescue experiments, indicating that the RBD-FIP domain is not required for Erc1-dependent cell shape regulation. Notably, Erc1a and Erc1b share the same interacting partners and functions except that Erc1b contains a conserved IWA domain that is required for interaction of a protein complex unique to pre-synaptic neurons (Wang et al., 2002; Monier et al., 2002; Lansbergen et al., 2006; Grigoriev et al., 2007). Future investigations of Erc1a's RBD-FIP and other domains could reveal functional differences between the two isoforms.

Regulation of cell behaviors during differentiation

A longstanding goal of developmental biology is to understand how different cellular regulatory pathways are integrated during differentiation to create phenotypically specialized cell types. Much work in this area has focused on gene regulatory networks and transcription factors that govern lineage and cell-type specification, for example myoD function in myogenic differentiation (Cao et al., 2010) or sox9 in chondrogenesis (Ohba et al., 2015). However, less is known about the downstream factors that execute

changes in cell behavior during differentiation. For example, mesenchymal stem cells undergo a battery of changes during their differentiation to chondrocytes in order to become specialized secretory cells. Not only must chondrocytes express high levels of type II collagen and other matrix proteins, but the biosynthetic-secretory pathway must be coordinately regulated to meet the demands of ECM synthesis and secretion. For example, failure to export proteins from the ER causes backlog of type II collagen and compromises organ growth (Lang et al., 2006; Sarmah et al., 2010; Melville et al., 2011). Differentiation would also require regulation of the cytoskeleton, cell polarity, the cell cycle, and many other processes. Ultimately the complement of specialized cell behaviors determines the function of a mature differentiated cell, so it is of great interest to understand how these processes are coordinately regulated.

Our study provides a unique example of a cell behavior having a dual function during differentiation and organ growth. Before differentiation, mesenchymal cartilage templates are composed of clusters of small round progenitor cells. Subsequent chondrocyte differentiation is characterized by synthesis, trafficking, and secretion of cartilage ECM proteoglycans, as well as polarized cell growth. These two processes seem to be primarily responsible for the rapid growth that occurs after cartilage formation since we found that proliferation is nearly absent at this stage. Interestingly, both ECM formation and cell growth seem to be influenced by the secretory pathway. Whereas inhibiting ER export via COPII loss-of-function blocks cell growth after chondrocyte differentiation (Sarmah et al., 2010), inhibiting post-Golgi trafficking leads to altered cell growth due to changes in microtubule polarity. These data indicate that secretory

pathway is tightly regulated to facilitate multiple phenotypic changes during differentiation.

We propose that high levels of secretory activity with membrane being continuously delivered to the cell surface give young chondrocytes an intrinsic propensity toward cell growth, and that regulation of endo- and exocytic trafficking along microtubule tracks helps to determine where at the plasma membrane lipid and protein cargos are delivered to drive cell shape changes. The biosynthetic pathway originating in the ER may be required to promote cell growth via cargo synthesis, while sorting through the Golgi and possibly endosomes acts as a gatekeeper for plasma membrane expansion by spatially restricting cargo delivery at the cell surface. Future studies examining whether the gene regulatory networks underlying chondrocyte cell specification modulate the expression of specific trafficking components during cell growth may help to uncover how cell behavior changes are executed during cell differentiation.

Regulation of pre-Golgi traffic in lipid absorption

Dietary lipids, because they are not water soluble, are unable to be directly absorbed in the intestine and secreted to circulation. Rather, they must first be extensively processed in several regulated steps. Ingested lipids undergo initial processing in both the oral cavity and gut lumen, where the combined functions of lipases, bile salts, and peristaltic activity result in the emulsification and incorporation of lipids into suspension within micelles, solubilizing the lipids. Micelles are then acted upon by additional lipases and other gastric enzymes to process more complex lipids into core components that can

be absorbed by the apical surface of enterocytes. These include free fatty acids, monoacylglycerol, and free cholesterol. Transporters that are located on the enterocyte apical membrane facilitate the uptake of different classes of lipids into the enterocyte cytoplasm, and after uptake lipids are transported to the endoplasmic reticulum (ER), where they are modified and incorporated into specialized vesicular transport carriers known as chylomicrons. These vesicles are then trafficked from the ER to the Golgi to be further modified and are ultimately secreted from enterocytes to be transported to different tissues in the body for utilization.

Chylomicron transport is a specialized form of COPII (coat protein complex II)-mediated ER-to-Golgi traffic. Although chylomicrons require similar cellular machinery as COPII vesicles, including Sar1, Sec23, and Sec24 (Levy et al., 2011), lipid carriers are substantially larger than standard COPII carriers. Additionally, some in vitro studies indicate that COPII machinery may function differently in chylomicron transport than in protein cargo transport, namely that COPII components are required for chylomicron fusion at the Golgi rather than for ER export (Siddiqi et al., 2003). These unique features of chylomicron transport are poorly understood and have largely been studied using in vitro and cell culture systems (e.g. Caco-2 cell line derived from colorectal carcinoma). Thus, much of our understanding of COPII function in chylomicron transport has not been examined in an in vivo system with normal physiology and absorptive properties. The zebrafish sar1b model that I developed, along with feeding, lipid clearance, and cholesterol uptake assays, provides not only proof-of-concept for modeling lipid malabsorption diseases but also a set of protocols to analyze lipid absorption in future

studies. For example, our system can be used to screen chemical libraries to identify molecules that relieve lipid retention in sar1b-deficient animals.

Sar1 paralog-specific function in chylomicron transport

A fascinating aspect of COPII function in lipid metabolism is that although vertebrates have two Sar1 parlogs (Sar1a and Sar1b) that share 90% amino acid sequence identity, Sar1b function is uniquely required for chylomicron transport. This conclusion is supported by the fact that mutations in human *SAR1B* result in chylomicron retention disease (CMRD, OMIM 246700), which is also known as Anderson disease (ANDD), but mutations in *SAR1A* have not been reported for CMRD or any other disease. Additionally, CMRD patients were reported to have modest but significant increases in *SAR1A* expression in the intestine. These findings suggest that Sar1a cannot compensate for loss of Sar1b in lipid transport despite high sequence conservation; however, this hypothesis had not been directly tested in vivo due to a lack of a disease model. In my studies, I performed replacement experiments by overexpressing either *sar1a* or *sar1b* in sar1b-MO embryos and found that *sar1a* partially compensates for loss of *sar1b* in overall growth and morphogenesis but does not significantly restore lipid clearance in the gut. These results suggest that the two paralogs have redundant function in most cargo transport (e.g. ECM cargo), while Sar1b is uniquely required in the gut. Thus, my research provides direct evidence that Sar1a does not compensate for Sar1b function in lipid transport.

The functional differences between Sar1 paralogs are not well understood and under investigation by many research groups. It has been postulated that Sar1b function in chylomicron transport may be related to its rate of GTP hydrolysis (Unlu et al., 2014). Sar1 initiates vesicle budding and helps to recruit COPII coat components to the ER membrane. Lower GTP hydrolysis rates are thought to slow the kinetics of COPII formation and allow larger vesicles to form (Fromme et al., 2007). This may explain why Sar1b is specifically required for chylomicrons while both Sar1 paralogs seem to have redundant function for most other cargo.

Structure-function studies using genetic replacement assays I developed may provide a unique model to uncover the mechanistic basis for the functional differences between Sar1a and Sar1b. For example, using a Sar1b-depleted background, one can express Sar1b variants with mutations in divergent residues that differ in the two paralogs and then test their efficiency at clearing lipids from the gut. For this type of analysis, it may be preferable to use a *sar1b* genetic mutant rather than morpholino knockdown in order to obtain uniform and consistent Sar1b loss-of-function at later stages of development. For this, I recently used the CRISPR/Cas9 system (Jao et al., 2013) to generate a *sar1b* knockout line. Given that human Sar1a and Sar1b differ only by 20 amino acids, and because my studies show Sar1b function in chylomicron transport is conserved from zebrafish to humans, one would expect that amino acids that confer Sar1b-specific function in chylomicron secretion should be conserved in fish and humans. I am using this rationale to design and generate Sar1b variants for the genetic replacement and lipid clearance assays.

Sar1b-dependent dietary cholesterol uptake

Cholesterol is a vital component of phospholipid membranes in cells, particularly within the plasma membrane where it regulates permeability and structural organization (Wüstner and Solanko, 2015). Additionally, cholesterol has important functions in lipid metabolism and physiology, since it is a biosynthetic precursor of vitamin D and steroid hormones (Cortes et al., 2014). In humans, cholesterol is derived primarily by de novo synthesis and secretion from the liver, but a significant portion is provided from dietary sources. The majority of dietary cholesterol is present as a free sterol form that can be directly absorbed into enterocytes, while about 10-15% is an esterified form that must be hydrolyzed by secreted digestive enzymes in the intestinal lumen in order to be absorbed (Iqbal and Hussain, 2009). After absorption, cholesterol is transported to the ER, where it is then packaged along with other lipids into chylomicrons for eventual secretion from enterocytes (Mansbach and Siddiqi, 2010). Hypocholesteremia is a condition where individuals have low circulating cholesterol levels, which can be caused either by defects in cholesterol biosynthesis or by impaired absorption of dietary cholesterol. Low serum cholesterol results in many pathological conditions and is considered a general indicator of poor health. Hypocholesteremia is also characteristic of CMRD caused by mutations in *SAR1B* (Roy et al., 1987; Charcosset et al., 2008).

Because CMRD is caused by defects in intracellular lipoprotein trafficking, a logical prediction is that hypocholesteremia associated with *SAR1B* mutations is due to cholesterol malabsorption in these patients. If this is true, then one would expect cholesterol to be backlogged in chylomicrons in Sar1b-deficient enterocytes. However,

this possibility had not been tested prior to our study, so the mechanistic basis of hypocholesteremia in CMRD is unknown. Using our zebrafish model, we fed a traceable cholesterol analog that can be absorbed and metabolized (Walters et al., 2012), and found that more that 75% of Sar1b-deficient larvae fail to uptake dietary cholesterol into enterocytes. Furthermore, among the small percentage of remaining Sar1b-deficient larvae that do uptake cholesterol, we observed that enterocytes have enlarged cholesterol inclusions compared to wild types. These data indicate that Sar1b is required both for cholesterol uptake into and secretion from enterocytes, which suggest unexpected and complex roles for Sar1b in cholesterol homeostasis.

Future mechanistic studies are needed to determine how Sar1b regulates cholesterol uptake, which is a complex process. For example, dietary cholesterol absorption into enterocytes depends on the concerted action of several proteins and lipids. A portion of dietary cholesterol cannot be directly absorbed and must first be modified by the enzyme cholesterol esterase, which is secreted by the pancreas into the intestinal lumen. Free cholesterol then must be incorporated into micelles, whose formation depends on the secretion of bile salts from the liver (Abumrad and Davidson, 2012). Micelles facilitate the movement of cholesterol to the enterocyte brush border, where interaction with NPCL1, a cholesterol transporter, occurs. NPCL1 translocation from the enterocyte cytoplasm to the brush border requires the presence of free fatty acids in the intestinal lumen (Walters et al., 2012), and high concentrations of free fatty acids from dietary intake in the intestinal lumen depend on enzymatic digestion of triaglycerides, which is facilitated by pancreatic lipase. After absorption through the brush border,

cholesterol is transported to the ER for packaging into chylomicrons. Therefore, dietary cholesterol uptake must be tightly regulated by several diverse cell-types and organs.

Notably, each of the steps required for cholesterol absorption require secretory activity, whether from enterocytes (NPCL1, a transmembrane glycosylated protein), the pancreas (cholesterol esterase and lipase secretion), or the liver (exporter-mediated bile secretion). Thus, impaired cholesterol uptake in Sar1b-deficient animals could be caused by impaired COPII-dependent protein transport in enterocytes and other digestive organs. Given Sar1b's high expression levels in each of these tissues and its involvement in secretory pathway activity, future studies can be used to clarify the precise mechanisms of cholesterol malabsorption caused by Sar1b-deficiency.

Concluding statement

Cargo trafficking is a fundamentally important cellular process that is critical for development and homeostasis. Due to paralogous expansion and differential regulation, many trafficking components have acquired specialized functions that are poorly understood in vivo. In this dissertation, I have described unique tissue-specific functions of trafficking components in the pre- and post-Golgi pathways that have vastly different requirements in organ morphogenesis and function. Future mechanistic studies that I have outlined here are likely to have important implications in human health and disease.

REFERENCES

Abumrad, N.A., and N.O. Davidson. 2012. Role of the Gut in Lipid Homeostasis. *Physiol. Rev.* 92:1061–1085. doi:10.1152/physrev.00019.2011.

Anderson, J.L., J.D. Carten, and S.A. Farber. 2011. Chapter 5 - Zebrafish Lipid Metabolism: From Mediating Early Patterning to the Metabolism of Dietary Fat and Cholesterol. *In* Methods in Cell Biology. M.W. and L.I.Z. H. William Detrich, editor. Academic Press. 111–141.

Aridor, M., K.N. Fish, S. Bannykh, J. Weissman, T.H. Roberts, J. Lippincott-Schwartz, and W.E. Balch. 2001. The Sar1 Gtpase Coordinates Biosynthetic Cargo Selection with Endoplasmic Reticulum Export Site Assembly. *J. Cell Biol.* 152:213–230. doi:10.1083/jcb.152.1.213.

Arnold, W.V., and A. Fertala. 2013. Skeletal diseases caused by mutations that affect collagen structure and function. *Int. J. Biochem. Cell Biol.* 45:1556–1567. doi:10.1016/j.biocel.2013.05.017.

Ashburner, M., C.A. Ball, J.A. Blake, D. Botstein, H. Butler, J.M. Cherry, A.P. Davis, K. Dolinski, S.S. Dwight, J.T. Eppig, M.A. Harris, D.P. Hill, L. Issel-Tarver, A. Kasarskis, S. Lewis, J.C. Matese, J.E. Richardson, M. Ringwald, G.M. Rubin, and G. Sherlock. 2000. Gene Ontology: tool for the unification of biology. *Nat. Genet.* 25:25–29. doi:10.1038/75556.

Baines, A.C., E.J. Adams, B. Zhang, and D. Ginsburg. 2013. Disruption of the Sec24d Gene Results in Early Embryonic Lethality in the Mouse. *PLoS ONE*. 8:e61114. doi:10.1371/journal.pone.0061114.

Barlowe, C., C. d'Enfert, and R. Schekman. 1993. Purification and characterization of SAR1p, a small GTP-binding protein required for transport vesicle formation from the endoplasmic reticulum. *J. Biol. Chem.* 268:873–879.

Barlowe, C., L. Orci, T. Yeung, M. Hosobuchi, S. Hamamoto, N. Salama, M.F. Rexach, M. Ravazzola, M. Amherdt, and R. Schekman. 1994. COPII: a membrane coat formed by Sec proteins that drive vesicle budding from the endoplasmic reticulum. *Cell*. 77:895–907.

Barrallo-Gimeno, A., J. Holzschuh, W. Driever, and E.W. Knapik. 2004. Neural crest survival and differentiation in zebrafish depends on mont blanc/tfap2a gene function. *Development*. 131:1463–1477. doi:10.1242/dev.01033.

Bernard, G., M. Panisset, A.F. Sadikot, and S. Chouinard. 2010. Chylomicron retention disease: Dystonia as a new clinical feature. *Mov. Disord.* 25:1755–1756. doi:10.1002/mds.23165.

Bhattacharya, N., J. O Donnell, and S.M. Stagg. 2012. The structure of the Sec13/31 COPII cage bound to Sec23. *J. Mol. Biol.* 420:324–334. doi:10.1016/j.jmb.2012.04.024.

Bianchi, P., E. Fermo, C. Vercellati, C. Boschetti, W. Barcellini, A. Iurlo, A.P. Marcello, P.G. Righetti, and A. Zanella. 2009. Congenital dyserythropoietic anemia type II (CDAII) is caused by mutations in the SEC23B gene. *Hum. Mutat.* 30:1292–1298. doi:10.1002/humu.21077.

Bielli, A., C.J. Haney, G. Gabreski, S.C. Watkins, S.I. Bannykh, and M. Aridor. 2005. Regulation of Sar1 NH2 terminus by GTP binding and hydrolysis promotes membrane deformation to control COPII vesicle fission. *J. Cell Biol.* 171:919–924. doi:10.1083/jcb.200509095.

Bi, X., R.A. Corpina, and J. Goldberg. 2002. Structure of the Sec23/24-Sar1 pre-budding complex of the COPII vesicle coat. *Nature*. 419:271–277. doi:10.1038/nature01040.

Bi, X., J.D. Mancias, and J. Goldberg. 2007. Insights into COPII coat nucleation from the structure of Sec23.Sar1 complexed with the active fragment of Sec31. *Dev. Cell*. 13:635–645. doi:10.1016/j.devcel.2007.10.006.

Bonfanti, L., A.A. Mironov, J.A. Martínez-Menárguez, O. Martella, A. Fusella, M. Baldassarre, R. Buccione, H.J. Geuze, A.A. Mironov, and A. Luini. 1998. Procollagen Traverses the Golgi Stack without Leaving the Lumen of Cisternae. *Cell*. 95:993–1003. doi:10.1016/S0092-8674(00)81723-7.

Boyadjiev, S.A., J.C. Fromme, J. Ben, S.S. Chong, C. Nauta, D.J. Hur, G. Zhang, S. Hamamoto, R. Schekman, M. Ravazzola, L. Orci, and W. Eyaid. 2006. Cranio-lenticulo-sutural dysplasia is caused by a SEC23A mutation leading to abnormal endoplasmic-reticulum-to-Golgi trafficking. *Nat. Genet.* 38:1192–1197. doi:10.1038/ng1876.

Boyadjiev, S.A., S.-D. Kim, A. Hata, C. Haldeman-Englert, E.H. Zackai, C. Naydenov, S. Hamamoto, R.W. Schekman, and J. Kim. 2011. Cranio-lenticulo-sutural dysplasia associated with defects in collagen secretion. *Clin. Genet.* 80:169–176. doi:10.1111/j.1399-0004.2010.01550.x.

Bradford, Y., T. Conlin, N. Dunn, D. Fashena, K. Frazer, D.G. Howe, J. Knight, P. Mani, R. Martin, S.A.T. Moxon, H. Paddock, C. Pich, S. Ramachandran, B.J. Ruef, L. Ruzicka, H.B. Schaper, K. Schaper, X. Shao, A. Singer, J. Sprague, B. Sprunger, C.V. Slyke, and M. Westerfield. 2010. ZFIN: enhancements and updates to the zebrafish model organism database. *Nucleic Acids Res.* gkq1077. doi:10.1093/nar/gkq1077.

Campbell, P.D., and F.L. Marlow. 2013. Temporal and tissue specific gene expression patterns of the zebrafish kinesin-1 heavy chain family, kif5s, during development. *Gene Expr. Patterns*. 13:271–279. doi:10.1016/j.gep.2013.05.002.

Campinho, P., M. Behrndt, J. Ranft, T. Risler, N. Minc, and C.-P. Heisenberg. 2013. Tension-oriented cell divisions limit anisotropic tissue tension in epithelial spreading during zebrafish epiboly. *Nat. Cell Biol.* 15:1405–1414. doi:10.1038/ncb2869.

Canty, E.G., and K.E. Kadler. 2005. Procollagen trafficking, processing and fibrillogenesis. *J. Cell Sci.* 118:1341–1353. doi:10.1242/jcs.01731.

Cao, Y., Z. Yao, D. Sarkar, M. Lawrence, G.J. Sanchez, M.H. Parker, K.L. MacQuarrie, J. Davison, M.T. Morgan, W.L. Ruzzo, R.C. Gentleman, and S.J. Tapscott. 2010. Genome-wide MyoD Binding in Skeletal Muscle Cells: A Potential for Broad Cellular Reprogramming. *Dev. Cell*. 18:662–674. doi:10.1016/j.devcel.2010.02.014.

Carten, J.D., M.K. Bradford, and S.A. Farber. 2011. Visualizing digestive organ morphology and function using differential fatty acid metabolism in live zebrafish. *Dev. Biol.* 360:276–285. doi:10.1016/j.ydbio.2011.09.010.

Charcosset, M., A. Sassolas, N. Peretti, C.C. Roy, C. Deslandres, D. Sinnett, E. Levy, and A. Lachaux. 2008. Anderson or chylomicron retention disease: Molecular impact of five mutations in the SAR1B gene on the structure and the functionality of Sar1b protein. *Mol. Genet. Metab.* 93:74–84. doi:10.1016/j.ymgme.2007.08.120.

Clark, B.S., M. Winter, A.R. Cohen, and B.A. Link. 2011. Generation of Rab-based transgenic lines for in vivo studies of endosome biology in zebrafish. *Dev. Dyn.* 240:2452–2465. doi:10.1002/dvdy.22758.

Clément, A., M. Wiweger, S. von der Hardt, M.A. Rusch, S.B. Selleck, C.-B. Chien, and H.H. Roehl. 2008. Regulation of Zebrafish Skeletogenesis by ext2/dackel and papst1/pinscher. *PLoS Genet*. 4:e1000136. doi:10.1371/journal.pgen.1000136.

Copic, A., C.F. Latham, M.A. Horlbeck, J.G. D'Arcangelo, and E.A. Miller. 2012. ER cargo properties specify a requirement for COPII coat rigidity mediated by Sec13p. *Science*. 335:1359–1362. doi:10.1126/science.1215909.

Corbeel, L., and K. Freson. 2008. Rab proteins and Rab-associated proteins: major actors in the mechanism of protein-trafficking disorders. *Eur. J. Pediatr.* 167:723–729. doi:10.1007/s00431-008-0740-z.

Cortes, V.A., D. Busso, A. Maiz, A. Arteaga, F. Nervi, and A. Rigotti. 2014. Physiological and pathological implications of cholesterol. *Front. Biosci. Landmark Ed.* 19:416–428.

Coutinho, P., M.J. Parsons, K.A. Thomas, E.M.A. Hirst, L. Saúde, I. Campos, P.H. Williams, and D.L. Stemple. 2004. Differential Requirements for COPI Transport during Vertebrate Early Development. *Dev. Cell*. 7:547–558. doi:10.1016/j.devcel.2004.07.020.

Cutrona, M.B., G.V. Beznoussenko, A. Fusella, O. Martella, P. Moral, and A.A. Mironov. 2013. Silencing of Mammalian Sar1 Isoforms Reveals COPII-Independent Protein Sorting and Transport. *Traffic*. 14:691–708. doi:10.1111/tra.12060.

Dacks, J.B., and M.C. Field. 2007. Evolution of the eukaryotic membrane-trafficking system: origin, tempo and mode. *J. Cell Sci.* 120:2977–2985. doi:10.1242/jcs.013250.

Dannoura, A.H., N. Berriot-Varoqueaux, P. Amati, V. Abadie, N. Verthier, J. Schmitz, J.R. Wetterau, M.-E. Samson-Bouma, and L.P. Aggerbeck. 1999. Anderson's Disease Exclusion of Apolipoprotein and Intracellular Lipid Transport Genes. *Arterioscler. Thromb. Vasc. Biol.* 19:2494–2508. doi:10.1161/01.ATV.19.10.2494.

Davis, E.E., S. Frangakis, and N. Katsanis. 2014. Interpreting human genetic variation with in vivo zebrafish assays. *Biochim. Biophys. Acta BBA - Mol. Basis Dis.* 1842:1960–1970. doi:10.1016/j.bbadis.2014.05.024.

Delporte, F.M., V. Pasque, N. Devos, I. Manfroid, M.L. Voz, P. Motte, F. Biemar, J.A. Martial, and B. Peers. 2008. Expression of zebrafish pax6b in pancreas is regulated by two enhancers containing highly conserved cis-elements bound by PDX1, PBX and PREP factors. *BMC Dev. Biol.* 8:53. doi:10.1186/1471-213X-8-53.

Dent, E.W., S.L. Gupton, and F.B. Gertler. 2011. The Growth Cone Cytoskeleton in Axon Outgrowth and Guidance. *Cold Spring Harb. Perspect. Biol.* 3:a001800. doi:10.1101/cshperspect.a001800.

Dogterom, M., J.W. Kerssemakers, G. Romet-Lemonne, and M.E. Janson. 2005. Force generation by dynamic microtubules. *Curr. Opin. Cell Biol.* 17:67–74. doi:10.1016/j.ceb.2004.12.011.

Dohn, M.R., N.A. Mundell, L.M. Sawyer, J.A. Dunlap, and J.R. Jessen. 2013. Planar cell polarity proteins differentially regulate extracellular matrix organization and assembly during zebrafish gastrulation. *Dev. Biol.* 383:39–51. doi:10.1016/j.ydbio.2013.08.027.

Driever, W., L. Solnica-Krezel, A.F. Schier, S.C. Neuhauss, J. Malicki, D.L. Stemple, D.Y. Stainier, F. Zwartkruis, S. Abdelilah, Z. Rangini, J. Belak, and C. Boggs. 1996. A genetic screen for mutations affecting embryogenesis in zebrafish. *Development*. 123:37–46.

Ellis, K., J. Bagwell, and M. Bagnat. 2013. Notochord vacuoles are lysosome-related organelles that function in axis and spine morphogenesis. *J. Cell Biol.* 200:667–679. doi:10.1083/jcb.201212095.

Fromme, J.C., L. Orci, and R. Schekman. 2008. Coordination of COPII vesicle trafficking by Sec23. *Trends Cell Biol.* 18:330–336. doi:10.1016/j.tcb.2008.04.006.

Fromme, J.C., M. Ravazzola, S. Hamamoto, M. Al-Balwi, W. Eyaid, S.A. Boyadjiev, P. Cosson, R. Schekman, and L. Orci. 2007. The Genetic Basis of a Craniofacial Disease Provides Insight into COPII Coat Assembly. *Dev. Cell*. 13:623–634. doi:10.1016/j.devcel.2007.10.005.

Garbes, L., K. Kim, A. Rieß, H. Hoyer-Kuhn, F. Beleggia, A. Bevot, M.J. Kim, Y.H. Huh, H.-S. Kweon, R. Savarirayan, D. Amor, P.M. Kakadia, T. Lindig, K.O. Kagan, J. Becker, S.A. Boyadjiev, B. Wollnik, O. Semler, S.K. Bohlander, J. Kim, and C. Netzer. 2015. Mutations in SEC24D, Encoding a Component of the COPII Machinery, Cause a Syndromic Form of Osteogenesis Imperfecta. *Am. J. Hum. Genet.* 96:432–439. doi:10.1016/j.ajhg.2015.01.002.

Gardner, M.K., M. Zanic, and J. Howard. 2013. Microtubule catastrophe and rescue. *Curr. Opin. Cell Biol.* 25:14–22. doi:10.1016/j.ceb.2012.09.006.

Gauthier, N.C., O.M. Rossier, A. Mathur, J.C. Hone, and M.P. Sheetz. 2009. Plasma Membrane Area Increases with Spread Area by Exocytosis of a GPI-anchored Protein Compartment. *Mol. Biol. Cell*. 20:3261–3272. doi:10.1091/mbc.E09-01-0071.

Georges, A., J. Bonneau, D. Bonnefont-Rousselot, J. Champigneulle, J.P. Rabès, M. Abifadel, T. Aparicio, J.C. Guenedet, E. Bruckert, C. Boileau, A. Morali, M. Varret, L.P. Aggerbeck, and M.E. Samson-Bouma. 2011. Molecular analysis and intestinal expression of SAR1 genes and proteins in Anderson's disease (Chylomicron retention disease). *Orphanet J. Rare Dis.* 6:1. doi:10.1186/1750-1172-6-1.

Granero-Moltó, F., S. Sarmah, L. O'Rear, A. Spagnoli, D. Abrahamson, J. Saus, B.G. Hudson, and E.W. Knapik. 2008. Goodpasture Antigen-binding Protein and Its Spliced Variant, Ceramide Transfer Protein, Have Different Functions in the Modulation of Apoptosis during Zebrafish Development. *J. Biol. Chem.* 283:20495–20504. doi:10.1074/jbc.M801806200.

Grigoriev, I., D. Splinter, N. Keijzer, P.S. Wulf, J. Demmers, T. Ohtsuka, M. Modesti, I.V. Maly, F. Grosveld, C.C. Hoogenraad, and A. Akhmanova. 2007. Rab6 Regulates Transport and Targeting of Exocytotic Carriers. *Dev. Cell*. 13:305–314. doi:10.1016/j.devcel.2007.06.010.

Grigoriev, I., K.L. Yu, E. Martinez-Sanchez, A. Serra-Marques, I. Smal, E. Meijering, J. Demmers, J. Peränen, R.J. Pasterkamp, P. van der Sluijs, C.C. Hoogenraad, and A. Akhmanova. 2011. Rab6, Rab8, and MICAL3 Cooperate in Controlling Docking and Fusion of Exocytotic Carriers. *Curr. Biol.* 21:967–974. doi:10.1016/j.cub.2011.04.030.

He, B., F. Xi, J. Zhang, D. TerBush, X. Zhang, and W. Guo. 2007. Exo70p mediates the secretion of specific exocytic vesicles at early stages of the cell cycle for polarized cell growth. *J. Cell Biol.* 176:771–777. doi:10.1083/jcb.200606134.

He, H., F. Dai, L. Yu, X. She, Y. Zhao, J. Jiang, X. Chen, and S. Zhao. 2002. Identification and characterization of nine novel human small GTPases showing variable expressions in liver cancer tissues. *Gene Expr.* 10:231–242.

Howell, G.J., Z.G. Holloway, C. Cobbold, A.P. Monaco, and S. Ponnambalam. 2006. Cell Biology of Membrane Trafficking in Human Disease. *In* International Review of Cytology. K.W. Jeon, editor. Academic Press. 1–69.

Hu, S., J. Chen, and N. Wang. 2004. Cell spreading controls balance of prestress by microtubules and extracellular matrix. *Front. Biosci. J. Virtual Libr.* 9:2177–2182.

Iolascon, A., M.R. Esposito, and R. Russo. 2012. Clinical aspects and pathogenesis of congenital dyserythropoietic anemias: from morphology to molecular approach. *Haematologica*. 97:1786–1794. doi:10.3324/haematol.2012.072207.

Iolascon, A., R. Russo, M.R. Esposito, R. Asci, C. Piscopo, S. Perrotta, M. Fénéant-Thibault, L. Garçon, and J. Delaunay. 2010. Molecular analysis of 42 patients with congenital dyserythropoietic anemia type II: new mutations in the SEC23B gene and a search for a genotype-phenotype relationship. *Haematologica*. 95:708–715. doi:10.3324/haematol.2009.014985.

Iqbal, J., and M.M. Hussain. 2009. Intestinal lipid absorption. *Am. J. Physiol. - Endocrinol. Metab.* 296:E1183–E1194. doi:10.1152/ajpendo.90899.2008.

Ishikawa, Y., and H.P. Bächinger. 2013. A molecular ensemble in the rER for procollagen maturation. *Biochim. Biophys. Acta BBA - Mol. Cell Res.* 1833:2479–2491. doi:10.1016/j.bbamcr.2013.04.008.

Jao, L.-E., S.R. Wente, and W. Chen. 2013. Efficient multiplex biallelic zebrafish genome editing using a CRISPR nuclease system. *Proc. Natl. Acad. Sci. U. S. A.* 110:13904–13909. doi:10.1073/pnas.1308335110.

Jiang, S., Y. Li, X. Zhang, G. Bu, H. Xu, and Y. Zhang. 2014. Trafficking regulation of proteins in Alzheimer's disease. *Mol. Neurodegener.* 9:6. doi:10.1186/1750-1326-9-6.

Jones, B., E.L. Jones, S.A. Bonney, H.N. Patel, A.R. Mensenkamp, S. Eichenbaum-Voline, M. Rudling, U. Myrdal, G. Annesi, S. Naik, N. Meadows, A. Quattrone, S.A. Islam, R.P. Naoumova, B. Angelin, R. Infante, E. Levy, C.C. Roy, P.S. Freemont, J. Scott, and C.C. Shoulders. 2003. Mutations in a Sar1 GTPase of COPII vesicles are associated with lipid absorption disorders. *Nat. Genet.* 34:29–31. doi:10.1038/ng1145.

Kadzik, R.S., E.D. Cohen, M.P. Morley, K.M. Stewart, M.M. Lu, and E.E. Morrisey. 2014. Wnt ligand/Frizzled 2 receptor signaling regulates tube shape and branch-point formation in the lung through control of epithelial cell shape. *Proc. Natl. Acad. Sci.* 111:12444–12449. doi:10.1073/pnas.1406639111.

Kertai, M.D., Y.-J. Li, Y.-W. Li, Y. Ji, J. Alexander, M.F. Newman, P.K. Smith, D. Joseph, J.P. Mathew, and M.V. Podgoreanu. 2015. Genome-wide association study of perioperative myocardial infarction after coronary artery bypass surgery. *BMJ Open*. 5. doi:10.1136/bmjopen-2014-006920.

Khoriaty, R., M.P. Vasievich, and D. Ginsburg. 2012. The COPII pathway and hematologic disease. *Blood*. 120:31–38. doi:10.1182/blood-2012-01-292086.

Kimmel, C.B., W.W. Ballard, S.R. Kimmel, B. Ullmann, and T.F. Schilling. 1995. Stages of embryonic development of the zebrafish. *Dev. Dyn.* 203:253–310. doi:10.1002/aja.1002030302.

Kimmel, C.B., C.T. Miller, G. Kruze, B. Ullmann, R.A. BreMiller, K.D. Larison, and H.C. Snyder. 1998. The Shaping of Pharyngeal Cartilages during Early Development of the Zebrafish. *Dev. Biol.* 203:245–263. doi:10.1006/dbio.1998.9016.

Kim, S.-D., K.B. Pahuja, M. Ravazzola, J. Yoon, S.A. Boyadjiev, S. Hammamoto, R. Schekman, L. Orci, and J. Kim. 2012. The [corrected] SEC23-SEC31 [corrected] interface plays critical role for export of procollagen from the endoplasmic reticulum. *J. Biol. Chem.* 287:10134–10144. doi:10.1074/jbc.M111.283382.

Knapik, E.W., A. Goodman, O.S. Atkinson, C.T. Roberts, M. Shiozawa, C.U. Sim, S. Weksler-Zangen, M.R. Trolliet, C. Futrell, B.A. Innes, G. Koike, M.G. McLaughlin, L. Pierre, J.S. Simon, E. Vilallonga, M. Roy, P.W. Chiang, M.C. Fishman, W. Driever, and H.J. Jacob. 1996. A reference cross DNA panel for zebrafish (Danio rerio) anchored with simple sequence length polymorphisms. *Development*. 123:451–460.

Knapik, E.W., A. Goodman, M. Ekker, M. Chevrette, J. Delgado, S. Neuhauss, N. Shimoda, W. Driever, M.C. Fishman, and H.J. Jacob. 1998. A microsatellite genetic linkage map for zebrafish (Danio rerio). *Nat. Genet.* 18:338–343. doi:10.1038/ng0498-338.

Korzh, S., X. Pan, M. Garcia-Lecea, C. Winata, X. Pan, T. Wohland, V. Korzh, and Z. Gong. 2008. Requirement of vasculogenesis and blood circulation in late stages of liver growth in zebrafish. *BMC Dev. Biol.* 8:84. doi:10.1186/1471-213X-8-84.

Kuge, O., C. Dascher, L. Orci, T. Rowe, M. Amherdt, H. Plutner, M. Ravazzola, G. Tanigawa, J.E. Rothman, and W.E. Balch. 1994. Sar1 promotes vesicle budding from the endoplasmic reticulum but not Golgi compartments. *J. Cell Biol.* 125:51–65. doi:10.1083/jcb.125.1.51.

Kumkhaek, C., J.G. Taylor, J. Zhu, C. Hoppe, G.J. Kato, and G.P. Rodgers. 2008. Fetal haemoglobin response to hydroxycarbamide treatment and sar1a promoter polymorphisms in sickle cell anaemia. *Br. J. Haematol.* 141:254–259. doi:10.1111/j.1365-2141.2008.07045.x.

Kwan, K.M., E. Fujimoto, C. Grabher, B.D. Mangum, M.E. Hardy, D.S. Campbell, J.M. Parant, H.J. Yost, J.P. Kanki, and C.-B. Chien. 2007. The Tol2kit: A multisite gateway-based construction kit for Tol2 transposon transgenesis constructs. *Dev. Dyn.* 236:3088–3099. doi:10.1002/dvdy.21343.

Lang, M.R., L.A. Lapierre, M. Frotscher, J.R. Goldenring, and E.W. Knapik. 2006. Secretory COPII coat component Sec23a is essential for craniofacial chondrocyte maturation. *Nat. Genet.* 38:1198–1203. doi:10.1038/ng1880.

Lansbergen, G., I. Grigoriev, Y. Mimori-Kiyosue, T. Ohtsuka, S. Higa, I. Kitajima, J. Demmers, N. Galjart, A.B. Houtsmuller, F. Grosveld, and A. Akhmanova. 2006. CLASPs Attach Microtubule Plus Ends to the Cell Cortex through a Complex with LL5β. *Dev. Cell*. 11:21–32. doi:10.1016/j.devcel.2006.05.012.

Latimer, A., and J.R. Jessen. 2010. Extracellular matrix assembly and organization during zebrafish gastrulation. *Matrix Biol. J. Int. Soc. Matrix Biol.* 29:89–96. doi:10.1016/j.matbio.2009.10.002.

LeClair, E.E., S.R. Mui, A. Huang, J.M. Topczewska, and J. Topczewski. 2009. Craniofacial skeletal defects of adult zebrafish Glypican 4 (knypek) mutants. *Dev. Dyn.* 238:2550–2563. doi:10.1002/dvdy.22086.

Levic, D.S., J.R. Minkel, W.-D. Wang, W.M. Rybski, D.B. Melville, and E.W. Knapik. 2015. Animal model of Sar1b deficiency presents lipid absorption deficits similar to Anderson disease. *J. Mol. Med.* 93:165–176. doi:10.1007/s00109-014-1247-x.

Levy, E., E. Harmel, M. Laville, R. Sanchez, L. Emonnot, D. Sinnett, E. Ziv, E. Delvin, P. Couture, V. Marcil, and A.T. Sane. 2011. Expression of Sar1b Enhances Chylomicron Assembly and Key Components of the Coat Protein Complex II System Driving Vesicle Budding. *Arterioscler. Thromb. Vasc. Biol.* 31:2692–2699. doi:10.1161/ATVBAHA.111.233908.

Li, Y., and A.T. Dudley. 2009. Noncanonical frizzled signaling regulates cell polarity of growth plate chondrocytes. *Development*. 136:1083–1092. doi:10.1242/dev.023820.

Lui, W.-O., L. Zeng, V. Rehrmann, S. Deshpande, M. Tretiakova, E.L. Kaplan, I. Leibiger, B. Leibiger, U. Enberg, A. Höög, C. Larsson, and T.G. Kroll. 2008. CREB3L2-PPARgamma fusion mutation identifies a thyroid signaling pathway regulated by intramembrane proteolysis. *Cancer Res.* 68:7156–7164. doi:10.1158/0008-5472.CAN-08-1085.

MacArthur, D.G., T.A. Manolio, D.P. Dimmock, H.L. Rehm, J. Shendure, G.R. Abecasis, D.R. Adams, R.B. Altman, S.E. Antonarakis, E.A. Ashley, J.C. Barrett, L.G. Biesecker, D.F. Conrad, G.M. Cooper, N.J. Cox, M.J. Daly, M.B. Gerstein, D.B. Goldstein, J.N. Hirschhorn, S.M. Leal, L.A. Pennacchio, J.A. Stamatoyannopoulos, S.R. Sunyaev, D. Valle, B.F. Voight, W. Winckler, and C. Gunter. 2014. Guidelines for investigating causality of sequence variants in human disease. *Nature*. 508:469–476. doi:10.1038/nature13127.

Maddison, L.A., and W. Chen. 2012. Nutrient Excess Stimulates β-Cell Neogenesis in Zebrafish. *Diabetes*. 61:2517–2524. doi:10.2337/db11-1841.

Mancias, J.D., and J. Goldberg. 2008. Structural basis of cargo membrane protein discrimination by the human COPII coat machinery. *EMBO J.* 27:2918–2928. doi:10.1038/emboj.2008.208.

Mansbach, C.M., and S.A. Siddiqi. 2010. The Biogenesis of Chylomicrons. *Annu. Rev. Physiol.* 72:315–333. doi:10.1146/annurev-physiol-021909-135801.

Mao, Y., and B. Baum. 2015. Tug of war—The influence of opposing physical forces on epithelial cell morphology. *Dev. Biol.* 401:92–102. doi:10.1016/j.ydbio.2014.12.030.

Matsuoka, K., L. Orci, M. Amherdt, S.Y. Bednarek, S. Hamamoto, R. Schekman, and T. Yeung. 1998. COPII-Coated Vesicle Formation Reconstituted with Purified Coat Proteins and Chemically Defined Liposomes. *Cell*. 93:263–275. doi:10.1016/S0092-8674(00)81577-9.

Melville, D.B., and E.W. Knapik. 2011. Traffic jams in fish bones. *Cell Adhes. Migr.* 5:114–118. doi:10.4161/cam.5.2.14377.

Melville, D.B., M. Montero-Balaguer, D.S. Levic, K. Bradley, J.R. Smith, A.K. Hatzopoulos, and E.W. Knapik. 2011. The feelgood mutation in zebrafish dysregulates COPII-dependent secretion of select extracellular matrix proteins in skeletal morphogenesis. *Dis. Model. Mech.* 4:763–776. doi:10.1242/dmm.007625.

Merte, J., D. Jensen, K. Wright, S. Sarsfield, Y. Wang, R. Schekman, and D.D. Ginty. 2010. Sec24b selectively sorts Vangl2 to regulate planar cell polarity during neural tube closure. *Nat. Cell Biol.* 12:41–46; sup pp 1–8. doi:10.1038/ncb2002.

Miller, E.A., and C. Barlowe. 2010. Regulation of coat assembly—sorting things out at the ER. *Curr. Opin. Cell Biol.* 22:447–453. doi:10.1016/j.ceb.2010.04.003.

Miller, E., B. Antonny, S. Hamamoto, and R. Schekman. 2002. Cargo selection into COPII vesicles is driven by the Sec24p subunit. *EMBO J.* 21:6105–6113.

Mimori-Kiyosue, Y., I. Grigoriev, G. Lansbergen, H. Sasaki, C. Matsui, F. Severin, N. Galjart, F. Grosveld, I. Vorobjev, S. Tsukita, and A. Akhmanova. 2005. CLASP1 and CLASP2 bind to EB1 and regulate microtubule plus-end dynamics at the cell cortex. *J. Cell Biol.* 168:141–153. doi:10.1083/jcb.200405094.

Monier, B., M. Gettings, G. Gay, T. Mangeat, S. Schott, A. Guarner, and M. Suzanne. 2015. Apico-basal forces exerted by apoptotic cells drive epithelium folding. *Nature*. 518:245–248. doi:10.1038/nature14152.

Monier, S., F. Jollivet, I. Janoueix-Lerosey, L. Johannes, and B. Goud. 2002. Characterization of Novel Rab6-Interacting Proteins Involved in Endosome-to-TGN Transport. *Traffic*. 3:289–297. doi:10.1034/j.1600-0854.2002.030406.x.

Montero-Balaguer, M., M.R. Lang, S.W. Sachdev, C. Knappmeyer, R.A. Stewart, A. De La Guardia, A.K. Hatzopoulos, and E.W. Knapik. 2006. The mother superior mutation ablates foxd3 activity in neural crest progenitor cells and depletes neural crest derivatives in zebrafish. *Dev. Dyn.* 235:3199–3212. doi:10.1002/dvdy.20959.

Mooney, M.A., J.T. Nigg, S.K. McWeeney, and B. Wilmot. 2014. Functional and genomic context in pathway analysis of GWAS data. *Trends Genet.* 30:390–400. doi:10.1016/j.tig.2014.07.004.

Morris, C.E., and U. Homann. 2001. Cell surface area regulation and membrane tension. *J. Membr. Biol.* 179:79–102.

Müller, I.I., E.W. Knapik, and A.K. Hatzopoulos. 2006. Expression of the protein related to Dan and Cerberus gene—prdc—During eye, pharyngeal arch, somite, and swim bladder development in zebrafish. *Dev. Dyn.* 235:2881–2888. doi:10.1002/dvdy.20925.

Müller, I.I., D.B. Melville, V. Tanwar, W.M. Rybski, A. Mukherjee, M.B. Shoemaker, W.-D. Wang, J.A. Schoenhard, D.M. Roden, D. Darbar, E.W. Knapik, and A.K. Hatzopoulos. 2013. Functional modeling in zebrafish demonstrates that the atrial-fibrillation-associated gene GREM2 regulates cardiac laterality, cardiomyocyte differentiation and atrial rhythm. *Dis. Model. Mech.* 6:332–341. doi:10.1242/dmm.010488.

Nakano, A., and M. Muramatsu. 1989. A novel GTP-binding protein, Sar1p, is involved in transport from the endoplasmic reticulum to the Golgi apparatus. *J. Cell Biol.* 109:2677–2691. doi:10.1083/jcb.109.6.2677.

Neuhauss, S.C., L. Solnica-Krezel, A.F. Schier, F. Zwartkruis, D.L. Stemple, J. Malicki, S. Abdelilah, D.Y. Stainier, and W. Driever. 1996. Mutations affecting craniofacial development in zebrafish. *Development*. 123:357–367.

Nomura, H., T. Ohtsuka, S. Tadokoro, M. Tanaka, and N. Hirashima. 2009. Involvement of ELKS, an active zone protein, in exocytotic release from RBL-2H3 cells. *Cell. Immunol.* 258:204–211. doi:10.1016/j.cellimm.2009.05.005.

Novick, P., C. Field, and R. Schekman. 1980. Identification of 23 complementation groups required for post-translational events in the yeast secretory pathway. *Cell*. 21:205–215.

Ogata, S., J. Morokuma, T. Hayata, G. Kolle, C. Niehrs, N. Ueno, and K.W.Y. Cho. 2007. TGF-β signaling-mediated morphogenesis: modulation of cell adhesion via cadherin endocytosis. *Genes Dev.* 21:1817–1831. doi:10.1101/gad.1541807.

Ohara-Imaizumi, M., T. Ohtsuka, S. Matsushima, Y. Akimoto, C. Nishiwaki, Y. Nakamichi, T. Kikuta, S. Nagai, H. Kawakami, T. Watanabe, and S. Nagamatsu. 2005. ELKS, a Protein Structurally Related to the Active Zone-associated Protein CAST, Is Expressed in Pancreatic β Cells and Functions in Insulin Exocytosis: Interaction of ELKS with Exocytotic Machinery Analyzed by Total Internal Reflection Fluorescence Microscopy. *Mol. Biol. Cell*. 16:3289–3300. doi:10.1091/mbc.E04-09-0816.

Ohba, S., X. He, H. Hojo, and A.P. McMahon. 2015. Distinct Transcriptional Programs Underlie Sox9 Regulation of the Mammalian Chondrocyte. *Cell Rep.* 12:229–243. doi:10.1016/j.celrep.2015.06.013.

Ohisa, S., K. Inohaya, Y. Takano, and A. Kudo. 2010. sec24d encoding a component of COPII is essential for vertebra formation, revealed by the analysis of the medaka mutant, vbi. *Dev. Biol.* 342:85–95. doi:10.1016/j.ydbio.2010.03.016.

Le Pabic, P., C. Ng, and T.F. Schilling. 2014. Fat-Dachsous Signaling Coordinates Cartilage Differentiation and Polarity during Craniofacial Development. *PLoS Genet*. 10:e1004726. doi:10.1371/journal.pgen.1004726.

Paccaud, J.P., W. Reith, J.L. Carpentier, M. Ravazzola, M. Amherdt, R. Schekman, and L. Orci. 1996. Cloning and functional characterization of mammalian homologues of the COPII component Sec23. *Mol. Biol. Cell*. 7:1535–1546.

Paluch, E., and C.-P. Heisenberg. 2009. Biology and Physics of Cell Shape Changes in Development. *Curr. Biol.* 19:R790–R799. doi:10.1016/j.cub.2009.07.029.

Panagopoulos, I., E. Möller, A. Dahlén, M. Isaksson, N. Mandahl, A. Vlamis-Gardikas, and F. Mertens. 2007. Characterization of the native CREB3L2 transcription factor and the FUS/CREB3L2 chimera. *Genes. Chromosomes Cancer*. 46:181–191. doi:10.1002/gcc.20395.

Peränen, J., P. Auvinen, H. Virta, R. Wepf, and K. Simons. 1996. Rab8 promotes polarized membrane transport through reorganization of actin and microtubules in fibroblasts. *J. Cell Biol.* 135:153–167. doi:10.1083/jcb.135.1.153.

Peretti, N., C.C. Roy, A. Sassolas, C. Deslandres, E. Drouin, A. Rasquin, E. Seidman, P. Brochu, M.-C. Vohl, S. Labarge, R. Bouvier, M.-E. Samson-Bouma, M. Charcosset, A. Lachaux, and E. Levy. 2009. Chylomicron retention disease: A long term study of two cohorts. *Mol. Genet. Metab.* 97:136–142. doi:10.1016/j.ymgme.2009.02.003.

Picone, R., X. Ren, K.D. Ivanovitch, J.D.W. Clarke, R.A. McKendry, and B. Baum. 2010. A Polarised Population of Dynamic Microtubules Mediates Homeostatic Length Control in Animal Cells. *PLoS Biol*. 8:e1000542. doi:10.1371/journal.pbio.1000542.

Porazinski, S., H. Wang, Y. Asaoka, M. Behrndt, T. Miyamoto, H. Morita, S. Hata, T. Sasaki, S.F.G. Krens, Y. Osada, S. Asaka, A. Momoi, S. Linton, J.B. Miesfeld, B.A. Link, T. Senga, A. Castillo-Morales, A.O. Urrutia, N. Shimizu, H. Nagase, S. Matsuura, S. Bagby, H. Kondoh, H. Nishina, C.-P. Heisenberg, and M. Furutani-Seiki. 2015. YAP is essential for tissue tension to ensure vertebrate 3D body shape. *Nature*. advance online publication. doi:10.1038/nature14215.

Roach, H.I., T. Aigner, and J.B. Kouri. 2004. Chondroptosis: a variant of apoptotic cell death in chondrocytes? *Apoptosis Int. J. Program. Cell Death*. 9:265–277.

Rodríguez-Fraticelli, A.E., J. Bagwell, M. Bosch-Fortea, G. Boncompain, N. Reglero-Real, M.J. García-León, G. Andrés, M.L. Toribio, M.A. Alonso, J. Millán, F. Perez, M. Bagnat, and F. Martín-Belmonte. 2015. Developmental regulation of apical endocytosis controls epithelial patterning in vertebrate tubular organs. *Nat. Cell Biol.* 17:241–250. doi:10.1038/ncb3106.

Roy, C.C., E. Levy, P.H. Green, A. Sniderman, J. Letarte, J.P. Buts, J. Orquin, P. Brochu, A.M. Weber, C.L. Morin, Y. Marcel, and R.J. Deckelbaum. 1987. Malabsorption, hypocholesterolemia, and fat-filled enterocytes with increased intestinal apoprotein B. Chylomicron retention disease. *Gastroenterology*. 92:390–399.

Sachdev, S.W., U.H. Dietz, Y. Oshima, M.R. Lang, E.W. Knapik, Y. Hiraki, and C. Shukunami. 2001. Sequence analysis of zebrafish chondromodulin-1 and expression profile in the notochord and chondrogenic regions during cartilage morphogenesis. *Mech. Dev.* 105:157–162.

Saito, A., S. Hino, T. Murakami, S. Kanemoto, S. Kondo, M. Saitoh, R. Nishimura, T. Yoneda, T. Furuichi, S. Ikegawa, M. Ikawa, M. Okabe, and K. Imaizumi. 2009a. Regulation of endoplasmic reticulum stress response by a BBF2H7-mediated Sec23a pathway is essential for chondrogenesis. *Nat. Cell Biol.* 11:1197–1204. doi:10.1038/ncb1962.

Saito, K., M. Chen, F. Bard, S. Chen, H. Zhou, D. Woodley, R. Polischuk, R. Schekman, and V. Malhotra. 2009b. TANGO1 Facilitates Cargo Loading at Endoplasmic Reticulum Exit Sites. *Cell*. 136:891–902. doi:10.1016/j.cell.2008.12.025.

Sarmah, S., A. Barrallo-Gimeno, D.B. Melville, J. Topczewski, L. Solnica-Krezel, and E.W. Knapik. 2010. Sec24D-Dependent Transport of Extracellular Matrix Proteins Is Required for Zebrafish Skeletal Morphogenesis. *PLoS ONE*. 5:e10367. doi:10.1371/journal.pone.0010367.

Schekman, R., and P. Novick. 2004. 23 Genes, 23 years later. *Cell*. 116, Supplement 2:S13–S15. doi:10.1016/S0092-8674(03)00972-3.

Schlacht, A., and J.B. Dacks. 2015. Unexpected Ancient Paralogs and an Evolutionary Model for the COPII Coat Complex. *Genome Biol. Evol.* 7:1098–1109. doi:10.1093/gbe/evv045.

Schlegel, A., and D.Y.R. Stainier. 2006. Microsomal Triglyceride Transfer Protein Is Required for Yolk Lipid Utilization and Absorption of Dietary Lipids in Zebrafish Larvae†. *Biochemistry (Mosc.)*. 45:15179–15187. doi:10.1021/bi0619268.

Schlombs, K., T. Wagner, and J. Scheel. 2003. Site-1 protease is required for cartilage development in zebrafish. *Proc. Natl. Acad. Sci.* 100:14024–14029. doi:10.1073/pnas.2331794100.

Schwarz, K., A. Iolascon, F. Verissimo, N.S. Trede, W. Horsley, W. Chen, B.H. Paw, K.-P. Hopfner, K. Holzmann, R. Russo, M.R. Esposito, D. Spano, L. De Falco, K. Heinrich, B. Joggerst, M.T. Rojewski, S. Perrotta, J. Denecke, U. Pannicke, J. Delaunay, R. Pepperkok, and H. Heimpel. 2009. Mutations affecting the secretory COPII coat component SEC23B cause congenital dyserythropoietic anemia type II. *Nat. Genet.* 41:936–940. doi:10.1038/ng.405.

Sehring, I.M., B. Dong, E. Denker, P. Bhattachan, W. Deng, B.T. Mathiesen, and D. Jiang. 2014. An Equatorial Contractile Mechanism Drives Cell Elongation but not Cell Division. *PLoS Biol*. 12:e1001781. doi:10.1371/journal.pbio.1001781.

Shin, D., C.H. Shin, J. Tucker, E.A. Ober, F. Rentzsch, K.D. Poss, M. Hammerschmidt, M.C. Mullins, and D.Y.R. Stainier. 2007. Bmp and Fgf signaling are essential for liver specification in zebrafish. *Development*. 134:2041–2050. doi:10.1242/dev.000281.

Shoulders, C.C., D.J. Stephens, and B. Jones. 2004. The intracellular transport of chylomicrons requires the small GTPase, Sar1b. *Curr. Opin. Lipidol.* 15:191–197.

Siddiqi, S.A., F.S. Gorelick, J.T. Mahan, and C.M. Mansbach. 2003. COPII proteins are required for Golgi fusion but not for endoplasmic reticulum budding of the pre-chylomicron transport vesicle. *J. Cell Sci.* 116:415–427. doi:10.1242/jcs.00215.

Siddiqi, S., S.A. Siddiqi, and C.M. Mansbach. 2010. Sec24C is required for docking the prechylomicron transport vesicle with the Golgi. *J. Lipid Res.* 51:1093–1100. doi:10.1194/jlr.M002758.

Silvain, M., D. Bligny, T. Aparicio, P. Laforêt, A. Grodet, N. Peretti, D. Ménard, F. Djouadi, C. Jardel, J. Bégué, F. Walker, J. Schmitz, A. Lachaux, L. Aggerbeck, and M. Samson-Bouma. 2008. Anderson's disease (chylomicron retention disease): a new mutation in the SARA2 gene associated with muscular and cardiac abnormalities. *Clin. Genet.* 74:546–552. doi:10.1111/j.1399-0004.2008.01069.x.

Smedley, D., S. Kohler, W. Bone, A. Oellrich, J. Jacobsen, K. Wang, C. Mungall, N. Washington, S. Bauer, D. Seelow, P. Krawitz, C. Boerkel, C. Gilissen, M. Haendel, S.E. Lewis, and P.N. Robinson. 2014. Use of animal models for exome prioritization of rare disease genes. *Orphanet J. Rare Dis.* 9:O19. doi:10.1186/1750-1172-9-S1-O19.

Stagg, S.M., C. Gürkan, D.M. Fowler, P. LaPointe, T.R. Foss, C.S. Potter, B. Carragher, and W.E. Balch. 2006. Structure of the Sec13/31 COPII coat cage. *Nature*. 439:234–238. doi:10.1038/nature04339.

Stagg, S.M., P. LaPointe, A. Razvi, C. Gürkan, C.S. Potter, B. Carragher, and W.E. Balch. 2008. Structural basis for cargo regulation of COPII coat assembly. *Cell*. 134:474–484. doi:10.1016/j.cell.2008.06.024.

Stepanova, T., J. Slemmer, C.C. Hoogenraad, G. Lansbergen, B. Dortland, C.I.D. Zeeuw, F. Grosveld, G. van Cappellen, A. Akhmanova, and N. Galjart. 2003. Visualization of Microtubule Growth in Cultured Neurons via the Use of EB3-GFP (End-Binding Protein 3-Green Fluorescent Protein). *J. Neurosci.* 23:2655–2664.

Strachan, L.R., and M.L. Condic. 2004. Cranial neural crest recycle surface integrins in a substratum-dependent manner to promote rapid motility. *J. Cell Biol.* 167:545–554. doi:10.1083/jcb.200405024.

Straube, A., and A. Merdes. 2007. EB3 Regulates Microtubule Dynamics at the Cell Cortex and Is Required for Myoblast Elongation and Fusion. *Curr. Biol.* 17:1318–1325. doi:10.1016/j.cub.2007.06.058.

Sucic, S., A. El-Kasaby, O. Kudlacek, S. Sarker, H.H. Sitte, P. Marin, and M. Freissmuth. 2011. The serotonin transporter is an exclusive client of the coat protein complex II (COPII) component SEC24C. *J. Biol. Chem.* 286:16482–16490. doi:10.1074/jbc.M111.230037.

Swaroop, A., T.L. Yang-Feng, W. Liu, L. Gieser, L.L. Barrow, K.C. Chen, N. Agarwal, M.H. Meisler, and D.I. Smith. 1994. Molecular characterization of a novel human gene, SEC13R, related to the yeast secretory pathway gene SEC13, and mapping to a conserved linkage group on human chromosome 3p24-p25 and mouse chromosome 6. *Hum. Mol. Genet.* 3:1281–1286.

Tang, B.L., J. Kausalya, D.Y. Low, M.L. Lock, and W. Hong. 1999. A family of mammalian proteins homologous to yeast Sec24p. *Biochem. Biophys. Res. Commun.* 258:679–684. doi:10.1006/bbrc.1999.0574.

Tang, B.L., T. Zhang, D.Y. Low, E.T. Wong, H. Horstmann, and W. Hong. 2000. Mammalian homologues of yeast sec31p. An ubiquitously expressed form is localized to endoplasmic reticulum (ER) exit sites and is essential for ER-Golgi transport. *J. Biol. Chem.* 275:13597–13604.

Tao, J., M. Zhu, H. Wang, S. Afelik, M.P. Vasievich, X.-W. Chen, G. Zhu, J. Jensen, D. Ginsburg, and B. Zhang. 2012. SEC23B is required for the maintenance of murine professional secretory tissues. *Proc. Natl. Acad. Sci. U. S. A.* 109:E2001–2009. doi:10.1073/pnas.1209207109.

Topczewski, J., D.S. Sepich, D.C. Myers, C. Walker, A. Amores, Z. Lele, M. Hammerschmidt, J. Postlethwait, and L. Solnica-Krezel. 2001. The Zebrafish Glypican Knypek Controls Cell Polarity during Gastrulation Movements of Convergent Extension. *Dev. Cell*. 1:251–264. doi:10.1016/S1534-5807(01)00005-3.

Uchida, A., N.H. Alami, and A. Brown. 2009. Tight Functional Coupling of Kinesin-1A and Dynein Motors in the Bidirectional Transport of Neurofilaments. *Mol. Biol. Cell*. 20:4997–5006. doi:10.1091/mbc.E09-04-0304.

Ulrich, F., M. Krieg, E.-M. Schötz, V. Link, I. Castanon, V. Schnabel, A. Taubenberger, D. Mueller, P.-H. Puech, and C.-P. Heisenberg. 2005. Wnt11 Functions in Gastrulation by Controlling Cell Cohesion through Rab5c and E-Cadherin. *Dev. Cell*. 9:555–564. doi:10.1016/j.devcel.2005.08.011.

Unlu, G., D.S. Levic, D.B. Melville, and E.W. Knapik. 2014. Trafficking mechanisms of extracellular matrix macromolecules: Insights from vertebrate development and human diseases. *Int. J. Biochem. Cell Biol.* 47:57–67. doi:10.1016/j.biocel.2013.11.005.

van der Vaart, B., W.E. van Riel, H. Doodhi, J.T. Kevenaar, E.A. Katrukha, L. Gumy, B.P. Bouchet, I. Grigoriev, S.A. Spangler, K.L. Yu, P.S. Wulf, J. Wu, G.

Lansbergen, E.Y. van Battum, R.J. Pasterkamp, Y. Mimori-Kiyosue, J. Demmers, N. Olieric, I.V. Maly, C.C. Hoogenraad, and A. Akhmanova. 2013. CFEOM1-Associated Kinesin KIF21A Is a Cortical Microtubule Growth Inhibitor. *Dev. Cell*. 27:145–160. doi:10.1016/j.devcel.2013.09.010.

Vacaru, A.M., G. Unlu, M. Spitzner, M. Mione, E.W. Knapik, and K.C. Sadler. 2014. In vivo cell biology in zebrafish – providing insights into vertebrate development and disease. *J. Cell Sci.* 127:485–495. doi:10.1242/jcs.140194.

Vinson, C.R., P.B. Sigler, and S.L. McKnight. 1989. Scissors-grip model for DNA recognition by a family of leucine zipper proteins. *Science*. 246:911–916. doi:10.1126/science.2683088.

Wakana, Y., J. van Galen, F. Meissner, M. Scarpa, R.S. Polishchuk, M. Mann, and V. Malhotra. 2012. A new class of carriers that transport selective cargo from the trans Golgi network to the cell surface: Golgi to cell surface transport carriers. *EMBO J.* 31:3976–3990. doi:10.1038/emboj.2012.235.

Walters, J.W., J.L. Anderson, R. Bittman, M. Pack, and S.A. Farber. 2012. Visualization of Lipid Metabolism in the Zebrafish Intestine Reveals a Relationship between NPC1L1- Mediated Cholesterol Uptake and Dietary Fatty Acid. *Chem. Biol.* 19:913–925. doi:10.1016/j.chembiol.2012.05.018.

Walther, T.C., and R.V. Farese. 2012. Lipid Droplets and Cellular Lipid Metabolism. *Annu. Rev. Biochem.* 81:687–714. doi:10.1146/annurev-biochem-061009-102430.

Wang, Y., X. Liu, T. Biederer, and T.C. Südhof. 2002. A family of RIM-binding proteins regulated by alternative splicing: Implications for the genesis of synaptic active zones. *Proc. Natl. Acad. Sci.* 99:14464–14469. doi:10.1073/pnas.182532999.

Wansleeben, C., H. Feitsma, M. Montcouquiol, C. Kroon, E. Cuppen, and F. Meijlink. 2010. Planar cell polarity defects and defective Vangl2 trafficking in mutants for the COPII gene Sec24b. *Dev. Camb. Engl.* 137:1067–1073. doi:10.1242/dev.041434.

Welz, T., J. Wellbourne-Wood, and E. Kerkhoff. 2014. Orchestration of cell surface proteins by Rab11. *Trends Cell Biol.* 24:407–415. doi:10.1016/j.tcb.2014.02.004.

Wendeler, M.W., J.-P. Paccaud, and H.-P. Hauri. 2007. Role of Sec24 isoforms in selective export of membrane proteins from the endoplasmic reticulum. *EMBO Rep.* 8:258–264. doi:10.1038/sj.embor.7400893.

Williams, B.B., V.A. Cantrell, N.A. Mundell, A.C. Bennett, R.E. Quick, and J.R. Jessen. 2012a. VANGL2 regulates membrane trafficking of MMP14 to control cell polarity and migration. *J. Cell Sci.* 125:2141–2147. doi:10.1242/jcs.097964.

Williams, B.B., N. Mundell, J. Dunlap, and J. Jessen. 2012b. The planar cell polarity protein VANGL2 coordinates remodeling of the extracellular matrix. *Commun. Integr. Biol.* 5:325–328. doi:10.4161/cib.20291.

Wüstner, D., and K. Solanko. 2015. How cholesterol interacts with proteins and lipids during its intracellular transport. *Biochim. Biophys. Acta BBA - Biomembr.* 1848:1908–1926. doi:10.1016/j.bbamem.2015.05.010.

Yang, X.-Y., X.-Y. Zhou, Q.Q. Wang, H. Li, Y. Chen, Y.-P. Lei, X.-H. Ma, P. Kong, Y. Shi, L. Jin, T. Zhang, and H.-Y. Wang. 2013. Mutations in the COPII Vesicle Component Gene SEC24B are Associated with Human Neural Tube Defects. *Hum. Mutat.* 34:1094–1101. doi:10.1002/humu.22338.

Yang, Y., L. Topol, H. Lee, and J. Wu. 2003. Wnt5a and Wnt5b exhibit distinct activities in coordinating chondrocyte proliferation and differentiation. *Development*. 130:1003–1015. doi:10.1242/dev.00324.

Yoshihisa, T., C. Barlowe, and R. Schekman. 1993. Requirement for a GTPase-activating protein in vesicle budding from the endoplasmic reticulum. *Science*. 259:1466–1468.

Zhu, J., B. Lee, K.K. Buhman, and J.-X. Cheng. 2009. A dynamic, cytoplasmic triacylglycerol pool in enterocytes revealed by ex vivo and in vivo coherent anti-Stokes Raman scattering imaging. *J. Lipid Res.* 50:1080–1089. doi:10.1194/jlr.M800555-JLR200.

PUBLICATIONS

Eames BF, Yan YL, Swartz ME, **Levic DS**, Knapik EW, Postlethwait JH, Kimmel CB. 2011. Mutations in fam20b and xylt1 reveal that cartilage matrix controls timing of endochondral ossification by inhibiting chondrocyte maturation. *PLoS Genet*. 7(8):e1002246. PMC3161922

Melville DB, Montero-Balaguer M, **Levic DS**, Bradley K, Smith JR, Hatzopoulos AK, Knapik EW. 2011. The feelgood mutation in zebrafish dysregulates COPII-dependent secretion of select extracellular matrix proteins in skeletal morphogenesis. *Dis Model Mech*. 4(6):763-76. PMC3209646

Venkateswaran A, Sekhar KR, **Levic DS**, Melville DB, Clark TA, Rybski WM, Walsh AJ, Skala MC, Crooks PA, Knapik EW, Freeman ML. 2013. The NADH oxidase ENOX1, a critical mediator of endothelial cell radiosensitization, is crucial for vascular development. *Cancer Res*. 74(1):38-43. PMC3947320

Unlu G, **Levic DS**, Melville DB, Knapik EW. 2014. Trafficking mechanisms of extracellular matrix macromolecules: insights from vertebrate development and human diseases. *Int J Biochem Cell Biol*. 47:57-67. PMC3915713

Levic DS, Minkel JR, Wang WD, Rybski WM, Melville DB, Knapik EW. 2015. Animal model of Sar1b deficiency presents lipid absorption deficits similar to Anderson Disease. *J Mol Med*. 93(2):165-176. PMC4319984

Zou P, Wu S-Y, Koteiche HA, Mishra S, **Levic DS**, Knapik EW, Chen W, Mchaourab HS. 2015. A conserved role of αA-crystallin in the development of the zebrafish embryonic lens. *Exp Eye Res.* doi: 10.1016/j.exer.2015.07.001.

Pfaltzgraff ER, Samade R, Adams R, **Levic DS**, Bader DM, Fleming AE. 2015. Inter-professional projects promote and strengthen interdisciplinary collaborative behaviors. *Med Educ. In press.*

Levic DS, Melville DB, Unlu G, Knapik EW. Post-Golgi traffic acts as a gatekeeper of cell growth by spatially restricting cargo delivery. *In preparation.*